Infrared and Radio Studies of Massive Star Formation

by

James Cox

A thesis submitted to

Cardiff University

for the degree of

Doctor of Philosophy

28th September 2007

ProQuest LLC
789 East Eisenhower Parkway
P.O. Box 1346
Ann Arbor, MI 48106-1346

DECLARATION

This work has not previously been accepted in substance for any degree and is not being concurrently submitted in candidature for any degree.

Signed ..... Date 30th May 2008

STATEMENT 1

This thesis is being submitted in partial fulfilment of the requirements for the degree of PhD.

Signed ..... Date 30th May 2008

STATEMENT 2

The work presented in this thesis is all my own and carried out under the supervision of Dr. D. Ward-Thompson with the following exceptions: when I joined the THUMPER team the instrument had already been designed and built. However, the lab testing had only just begun and I continued this testing and characterised the instrument. I then took THUMPER to the telescope and was a key member of the team that commissioned the instrument and saw its first light. Similarly the Methanol Maser Multibeam Survey had been devised and the instrument built before I joined the team. I was present at the commissioning of the instrument however, and also saw first light on the Methanol Maser Multibeam Survey. I played a key role in commissioning the software for the instrument on the telescope at Parkes. The data analysis and comparison between the radio and infrared data presented in chapters 5 and 6 is all my own work.

A bibliography is appended.

Signed ..... Date 30th May 2008

STATEMENT 3

I hereby give consent for my thesis, if accepted, to be available for photocopying and for inter-library loan, and for the title and summary to be made available to outside organisations.

Signed ..... Date 30th May 2008

ACKNOWLEDGMENTS

I'd like to thank my supervisor, Professor Derek Ward-Thompson, for his guidance and advice as I carried out the work presented in this thesis and for his support and input during its writing. His patience when I disappeared of the face of the Earth, and his gee up during the last month or so of the write up was, and still is, massively appreciated. Thanks Derek.

The success of THUMPER would not have been possible without the goodwill and hard work of many people. Neal Potter and Rhodri Evans both worked hard to affect a smooth hand over of THUMPER, while Rashmi Sudiwala worked hard to pick up any pieces that were dropped during that process. The patience he displayed while explaining THUMPER's readout electronics to the n'th person was remarkable. Iris showed me how to transfer Helium in a way that would not cost the department £800 every time. Rob Tucker was always on hand in his workshop to offer components and advice, while Fred and Glynn were always willing to cut stuff up and drill holes in things. Professor Phil Mauskopf and Paul Hargreaves designed the lenses that were used on the JCMT, Brian Kiernan made them in a very short space of time, Ian Walker ensured the process ran smoothly - thanks to all of them. Professor Peter Ade gave a lot of his time for many useful discussions - thank you.

We are massively indebted to Professor Gary Davis, then director of the JCMT, for allowing us to use director discretionary time to commission THUMPER. Professor David Naylor deserves higher praise than my limited vocabulary allows. Without his presence and guidance at the JCMT, THUMPER would not have been commissioned. Darren Hayton's ability to listen to me talk utter nonsense and then gently suggest a saner course of action is unparallelled. Iain Coulson, our JCMT support scientist, went above and beyond, particularly when Neal and I were left alone; his three am phone calls kept us cheerful during poor weather. The JCMT support staff were all fantastic. Ken, Jon and the rest of the day crew were supportive and helped us so much.

My work on the Methanol Maser Multibeam project was aided by several people. Michele Pestalozzi during his spell at Cardiff was great in helping us get to grips with the maser data and suggesting things we could do with them. Professor Jim Caswell, Jimi Green, Danny Wong-Mcsweeney, Adam Avison and Maxim Voronkov all made observing a lot of fun. Finally, I'd like to thank Jim Cohen for allowing me to become involved with the MMB project - the Aussie day BBQ was super, thanks.

I'd also like to thank the friends who helped and supported me through the last few years. Thanks to Si and Al for taking me in and feeding me. Rob&Jane, Rhianne, Bruce and Emma for being good friends and buying me beer when I couldn't afford too. Sibley, Cloud, Nige and Noggin - thanks for being such great mates and overlooking just how bad I am at keeping in touch. Sid, thanks for listening to me moan a lot last summer.

Finally I'd like to thank my family for their support and love. Mum and Dad, Christopher and Lauren, Nan Cox and Nan Joy - thanks for everything.

ABSTRACT

The 6.67 GHz methanol maser is uniquely associated with the phenomena of the earliest stages of high mass star formation, high mass protostellar objects (HMPOs), hot molecular starless cores (HMSCs), and compact HII regions. An unbiased survey for these masers in the plane of the Galaxy, the Methanol Maser Multibeam (MMB) Survey, is outlined. It is noted that for the subsequent exploration of these regions highly spatially resolved mid and far infrared observations are required, since this is where the emission from HMSCs and HMPOs peak. I discuss a new far infrared camera, THUMPER, which was designed and built in Cardiff. THUMPER was capable of making such observations of HMSCs and HMPOs. The observations that were carried out with THUMPER on the JCMT are presented. These are the characterisation of the atmospheric transmission at 200 μm on Mauna Kea and the first 200 μm ground based astronomical images. I present the results of the MMB survey and compare the maser detections with various infrared parameters. The spectral indices (α) of the infrared sources are calculated and a correlation between α and the flux of the associated maser is found. This is explained in terms of the mass of dust present and age of the source. The more dust associated with the source, the brighter the maser.

Contents

List of Figures

List of Tables

Chapter 1

The Formation of Massive Stars

1.1 Introduction

1.2 Overview

Understanding how massive stars form is crucial because of the role that they play in the evolution of Galaxies; they heat the molecular clouds that they are formed in, enrich the interstellar medium with heavy elements, influence their local environment with stellar winds and radiation fields, ionise their surroundings, and sometimes trigger nearby star formation. Though vital and widespread, much is unknown about the formation of massive stars, particularly the earliest stages of their evolution and the conditions inside the molecular cloud in which they are formed.

An evolutionary scenario for the formation of high mass stars ($M > 8M_{\odot}$) was recently outlined by Beuther et al. (2007). An overview of the processes and

scales involved in massive star formation is given here. Firstly, following Williams et al. (2000), the term *clumps* is used to describe condensations associated with cluster formation, and the term *cores* is used to describe molecular condensations that form single or gravitationally bound multiple massive protostars.

The sequence for high mass star forming cores is:

- High mass starless cores (HMSCs)
- High mass cores containing accreting low/intermediate mass protostar(s) destined to become (a) high mass star(s)
- High mass protostellar objects (HMPOs)
- Main sequence stars.

High mass protostellar objects (HMPOs) are accreting high mass protostars which have not necessarily formed a detectable Hot Molecular Core (HMC) and/or hypercompact HII region (HCHIIs, size r $<$ 0.01 pc). HMCs and HCHIIs might exist simultaneously. Ultracompact HII regions (UCHIIs, size 0.01 $>$ r $<$ 0.1pc) are a transition group (Wood and Churchwell, 1989a). Some of them may still contain accreting protostars, i.e. are at the end of the HMPO stage, but many have probably finished accreting and can be considered as final stars in the above sequence. High mass stars can be deeply embedded and still accreting while on the main sequence, as well as after they stop accreting and become final stars. It should be noted that HCHII regions are considered distinct from UCHII regions, that is, they are not just more extreme versions of UCHII regions. This is mostly because of the extremely broad recombination line profiles, typically 40 - 50 kms^{-1}, with some greater than 100 kms^{-1} (Gaune et al. 1995, Johnson et al. 1998, Sewilo

et al. 2004). The line widths of UCHIIs are typically 30 - 40 kms^{-1} (Keto et al. 1995; Afferbach et al. 1996)

The intermediate stage between HMSC and HMPO, i.e. high mass cores containing an accreting protostar which is destined to become a high mass star, has not been well studied. However, there is in all likeliness a stage between HMSCs and HMPOs which contains high mass cores with embedded low/intermediate mass objects.

On the cluster/clump scale the proposed evolutionary sequence is that massive starless clumps lead to protoclusters, which in turn evolve into stellar clusters (Beuther et al. 2007). Massive starless clumps can only contain high mass starless cores (and low mass starless cores), but protoclusters can in principle contain all sorts of smaller scale objects (low and intermediate mass protostars, HMPOs, HMCs, HCHIIs, UCHIIs and even HMSCs).

1.3 Giant Molecular Clouds

Giant molecular clouds (GMCs) are the largest objects in our Galaxy, with sizes between ~20 and ~100 pc and masses between $\sim 10^4$ and $\sim 10^6$ $M_\odot$ (McKee 1999). They are dynamical objects with varying temperatures and densities which contain stars at all stages of their evolution.

Sanders et al. (1993), using large velocity gradient (LVG) analysis on a variety of molecular transitions, calculated average local densities in the range $n_H \approx 4 \times 10^3$ to 1.2×10^4 cm^{-3} for GMCs in our own Galaxy, with temperatures ranging from 10 to 15 K. Volume averaged densities of $n_H \approx 50$ to 100 cm^{-3}, much lower than

the average local densities, imply that these clouds are highly clumped.

The molecular gas in these clouds moves at velocities between 2 and 3 kms^{-1} which, with typical sound speeds of 0.2 kms^{-1}, are therefore supersonic. These motions are mainly due to turbulence (MacLow and Klessen 2004, Elmergreen and Scalo 2004). The magnetic field strength in these regions has been measured to be around a few 10 μG (e.g. Crutcher 1999), which gives magnetic critical masses between 5×10^5 $M_\odot$ for GMCs, to just a few $M_\odot$ for low mass star forming regions. Although the Jeans masses for GMCs is low, support from turbulence and magnetic fields is believed to keep them from complete collapse on large scales.

1.4 HMPOs and UCHIIs

Most observational work on high mass star forming regions has focused on HMPOs and UCHIIs. These objects already contain an embedded massive protostellar source and have mid infrared emission from the hot dust. HMPOs are between a few hundred and a few thousand solar masses and have sizes between 0.25 pc and 0.5 pc, their average densities can exceed 10^6 cm^{-3}. From studies of various NH_3 transitions, the mean temperature of these objects is 22 K, and the line widths of $NH_3(1,1)$ are approximately 2.1 kms^{-1} (Beuther et al. 2007). HMPOs are associated with H_2O and class II CH_3OH masers (see below).

UCHII regions were distinguished from compact HII regions and then defined observationally by Wood and Churchwell (1989a) as regions with sizes $\leq$ 0.1 pc, densities $\geq 10^4$ cm^{-3}. Their study, as well as that of HCHII regions, is important because the ionised gas reveals properties of the stars, and illuminates the immediate surroundings, allowing the density distribution to be inferred, as well as other

details of the environment in which the star is forming.

1.5 Problems with current HMSF theories

The main conceptual problem with high mass star formation (HMSF), is that the radiation pressure that the massive star exerts on the surrounding dust and gas core could theoretically halt further accretion (Kahn 1974, Wolfire and Casinelli 1987, Jijina and Adams 1996, Yorke and Sonnhalter 2002, Krumholz et al. 2005b). This is particularly a problem because stars with masses greater than about 8 solar masses have short Kelvin-Helmholtz (KH) times, meaning that a massive star can be on the main sequence while still accreting. Once nuclear burning is switched on, a huge luminosity, and hence large radiation pressure is exerted on the infalling dust and gas. This is in stark contrast with low mass star formation, where the formation time is short compared with the KH time; accretion has generally finished by the time they reach the main sequence, on which they evolve extensively.

This radiation pressure effect currently limits the upper mass of stars that can form by accretion in our current theories; in fact, stars of masses greater than 50 $M_{\odot}$ are currently theoretically impossible. Therefore it is not just a case of scaling up the theories of low mass star formation, but altering them completely.

There are two current approaches to this. The first one is to change the numbers involved in the accretion of matter onto the (proto)star, such as by: varying dust properties (e.g. Wolfire and Casinelli 1987); increasing the accretion rates in turbulent cloud cores from about 10^{-6} $M_{\odot}yr^{-1}$ (typical for LMSF) to the order 10^{-4} to 10^{-3} $M_{\odot}yr^{-1}$ (e.g Norberg and Maeder 2000, Mckee and Tan 2003);

using accretion via disks (e.g. Jijinja and Adams 1996); invoking accretion through the evolving (hyper) compact HII region (Keto, 2003; Keto and Wood, 2006); or permitting the radiation pressure to escape via wind blown cavities (Krumholz et al. 2005a). All of these studies present theoretical evidence that high mass stars can form in an accretion based manner, that is, in a modified version of low mass star formation.

The alternative approach is to fundamentally change the way in which massive stars form compared to low mass stars. The observation that high mass stars always form at dense centres of stellar clusters led to the idea of coalescence. In this, the protostellar and stellar densities are around 10^8 pc^{-3} which is high enough that protostars could collide and merge. This overcomes the effects of radiation pressure.

Another scenario put forward is competitive accretion, which occurs in a clustered environment. Protostars don't need to physically merge, but the accretion rates of massive cluster members is linked to the number of stellar companions (Bonnell et al., 2004).

What all of these potential explanations for high mass star formation need is observations of the earliest stages of this process. These are currently lacking because the initial stages happen very quickly in some of the most dense and dusty regions of GMCs. What are needed are tracers of massive star formation to pinpoint the exact areas to explore. The 6.7 GHz methanol maser is such a tracer, as it is exclusively associated with the earliest stages of high mass star formation, with HMPOs, HMCs and UCHII regions. For the subsequent exploration, the mid and far infrared regions are required, since this is where the emission from HMSCs and HMPOs peaks.

1.6 Astronomical Masers

1.6.1 Masers

A maser is a source of stimulated spectral line emission in the microwave region of the electromagnetic spectrum. Astronomical masers are naturally occurring, usually associated with energetic astrophysical phenomena. The radiation from a maser, which is from a very compact region, is intense and collimated. A variety of molecules, giving the right conditions, can give rise to maser emission, these include: Hydroxyl (OH), Water (H_2O), SiO, Methanol (CH_3OH) and Ammonia (NH_3). The right conditions for masing are that the gaseous cloud is in a state of population inversion. The exact mechanism responsible for population inversion, or "pumping" of the maser, is not precisely known, though it is thought that the various maser species are maybe pumped by different processes such as radiative or collisional excitation.

The clumps of molecular gas which become masers are very dense (between 10^6 and 10^9 cm^{-3}) and are just a few tens of AU in size. From very long baseline interferometry (VLBI) observations, it has been shown that maser sources comprise groups of intense spots of radiation. These spots are usually less than 10^{15} cm in size, and are distributed in areas of around 10^{16} cm. Masers have brightness temperatures $\sim 10^{12}$ K and aspect ratios of $\sim$10 (Elitzur 1992).

This intense maser radiation, which is not attenuated by dust, makes them ideal for probing objects which are accreting dusty dense material. Doppler shifting of the spectral line allows kinematic information of the maser source to be derived which together with proper motion measurements, allows accurate distances to be

calculated for the sources.

1.6.2 Methanol Masers

Methanol (CH_3OH) has a complicated line structure with well over 200 lines in the frequency range between 834 MHz and 350 GHz. Over 20 of those have been seen to display maser emission in more than a hundred star forming regions, making methanol the species with the largest number of astronomical masing lines. The first methanol maser to be detected was towards Orion and arose from the $J_k = 2 \rightarrow J_k = 1$ series of the E species. Five transitions with frequencies around 25 GHz were detected (Barret, Schwartz and Waters 1971). The 6.7 GHz line, the basis of the Methanol Maser Multibeam Survey which will be discussed in Chapter 4, was not discovered until 1991 (Menten 1991b). This line corresponds to the $5_1 \rightarrow 6_0$ A^+ transition and flux densities can reach 5000 Jy, making it, after the 22 GHz H_2O maser, the second strongest astronomical maser detected (Elitzur 1992). Figure 1.1 shows the spectra of 6.7 GHz Menten detected towards various star forming regions (1991).

Methanol masers are associated with OH masers, H_2O masers and compact HII regions. Because of this, and the fact that there are many transitions for methanol masers which are found in different regions (for example, no 12 GHz methanol maser has been found near a 25 GHz maser), a scheme was required to divide these into separate classes. Batrla et al. (1987) proposed that there were two classes of methanol maser which became known as Class I and Class II. Class II sources often show absorption in the class I lines and vice versa (Menten, 1991b, Elitzur 1992). Since this classification was devised more class II CH_3OH masers than class I have been discovered.

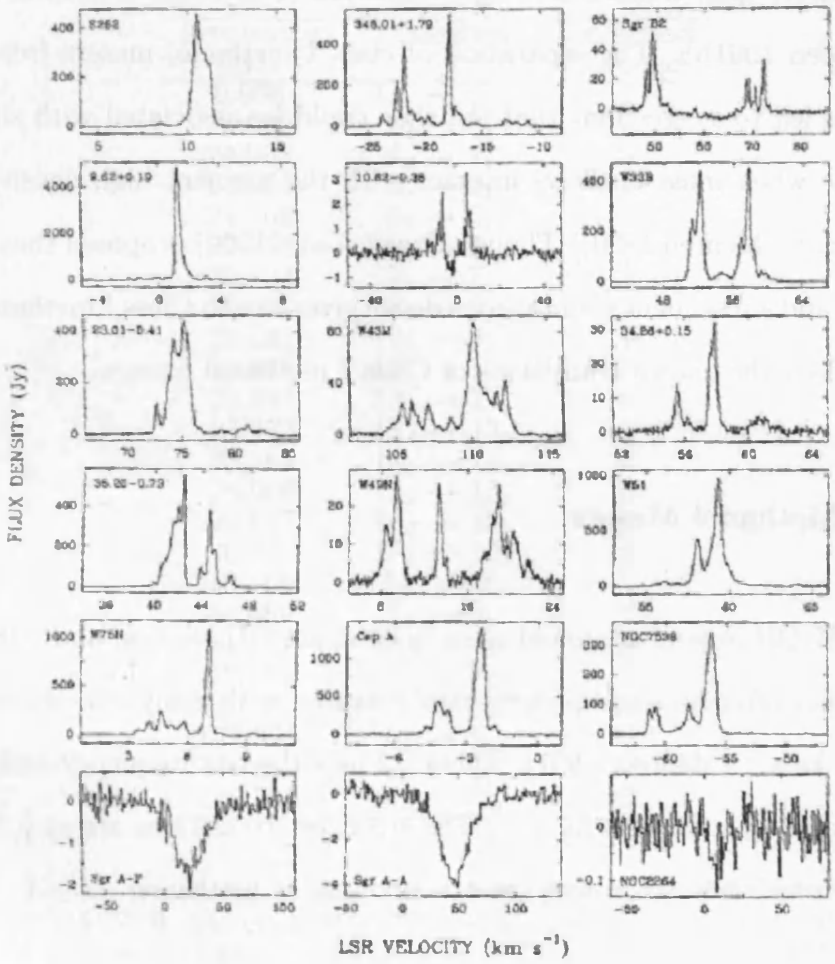

Figure 1.1: Spectra of 6.7 GHz methanol masers detected towards various star forming regions (Menten 1991b)

Class I Methanol Masers

Class I CH_3OH masers are found in the general area of massive star formation, but offset from compact HII regions, strong infrared sources and OH and H_2O masers. Some class I methanol masers are accompanied by absorption in the class II 12.2 and 6.7 GHz transitions (e.g. Whiteoak et al 1988; Whiteoak and Peng, 1989; Menten 1991b). The separation of class I methanol masers from compact HII regions led to suggestions that the they could be associated with shock fronts which arise when mass outflows interact with the ambient high density material (Plambeck and Menten 1990). Though Cragg et al. (1992) proposed that collisional excitation and subsequent spontaneous decay gives rise to Class I methanol masers. Table 1.1 lists the known transitions of Class I methanol masers.

Class II Methanol Masers

Class II CH_3OH masers are found close to compact HII regions, and, OH and H_2O masers. They often have complex spectral features, with many velocity components over a few kms^{-1} (Menten, 1991). Table 1.2 lists the rest frequency and transition of known class II methanol masers. The strongest transitions are at 6.7 GHz and 12.2 GHz, which both require a great abundance of methanol.

1.6.3 Previous Methanol Maser Surveys

Searches for 6.7 and 12.2 GHz methanol masers were initially focused towards IRAS colour selected sources, infrared sources, UCHII regions as well as OH and H_2O masers. Szymczak et al. (2002) performed an unbiased search for 6.7 GHz

Frequency GHz	Transition	Detection Reference
9.936	$9_{-1} \rightarrow 8_{-2}$	1
24.929	$3_2 \rightarrow 3_1$	2
24.933	$4_2 \rightarrow 4_1$	3
24.934	$2_2 \rightarrow 2_1$	2
24.959	$5_2 \rightarrow 5_1$	3
25.018	$6_2 \rightarrow 6_1$	3
25.124	$7_2 \rightarrow 7_1$	3
25.294	$8_2 \rightarrow 8_1$	3
25.541	$9_2 \rightarrow 9_1$	4
25.878	$10_2 \rightarrow 10_1$	5
26.847	$12_2 \rightarrow 12_1$	6
27.473	$13_2 \rightarrow 13_1$	6
28.169	$14_2 \rightarrow 14_1$	6
28.906	$15_2 \rightarrow 15_1$	6
29.637	$16_2 \rightarrow 16_1$	6
30.308	$17_2 \rightarrow 17_1$	6
36.169	$4_{-1} \rightarrow 3_0$	7
44.069	$7_0 \rightarrow 6_1$	7
84.521	$5_{-1} \rightarrow 4_0$	8
95.169	$8_0 \rightarrow 7_1$	9
104.3	$11_{-1} \rightarrow 10_{-2}$	10
132.891	$6_1 \rightarrow 5_0$	11
146.619	$9_0 \rightarrow 8_1$	12
229.759	$8_{-1} \rightarrow 7_0$	13

Table 1.1: Known transitions of class I methanol masers. 1: Slysh at al. (1993); 2: Barrett et al. (1975); 3: Barrett et al. (1971); 4: Menten et al. (1986); 5: Matsakis et al. (1980); 6: Wilson et al. (1996); 7: Morimoto et al. (1985); 8: Batrla and Menten (1988); 9: Nakano (1986); 10: Voronkov et al. (2005); 11: Slysh et al. (1997); 12: Menten (1991b); 13: Slysh et al. (2002).

Frequency GHz	Transition	Detection Reference
6.669	$5_1 \rightarrow 6_0$	1
12.179	$2_0 \rightarrow 3_{-1}$	2
19.967	$2_1 \rightarrow 3_0$	3
23.121	$9_2 \rightarrow 10_1$	4
28.97	$8_2 \rightarrow 9_1$	5
37.704	$7_0 \rightarrow 8_1$	6
38.293	$6_2 \rightarrow 5_3$	6
38.453	$6_2 \rightarrow 5_3$	6
86.616	$7_2 \rightarrow 6_3$	7
86.903	$7_2 \rightarrow 6_3$	7
107.014	$3_1 \rightarrow 4_0$	8
108.894	$0_0 \rightarrow 1_{-1}$	9
156.489	$8_0 \rightarrow 8_{-1}$	10
156.602	$2_1 \rightarrow 3_0$	10
156.829	$7_0 \rightarrow 7_{-1}$	10
157.049	$6_0 \rightarrow 6_{-1}$	10
157.179	$5_0 \rightarrow 5_{-1}$	10
157.246	$4_0 \rightarrow 4_{-1}$	10
157.271	$1_0 \rightarrow 1_{-1}$	10
157.272	$3_0 \rightarrow 3_{-1}$	10
157.276	$2_0 \rightarrow 2_{-1}$	10

Table 1.2: Known transitions of class II methanol masers. 1: Menten (1991b); 2: Batrla et al. (1987); 3: Wilson et al. (1985); 4: Wilson et al. (1984); 5: Wilson et al. (1993); 6: Haschick et al. (1989); 7: Sutton et al. (2001); 8: Val'tts et al. (1995); 9: Val'tts et al. (1999); 10: Slysh et al. (1995).

methanol masers covering 21 square degrees. They detected 100 sources, 26 of which were new. About 80 of the sources had an infrared counterpart within 1 arcsec, but not all the IRAS counterparts had colours typical of UCHII regions.

Several surveys have in the past been conducted towards colour selected IRAS sources. Two which selected IRAS sources based on the Wood and Churchwell (1989) were Schutte et al. (1993) and van der Walt et al. (1995).

The Wood and Churchwell criteria for colour selecting an IRAS source and labelling it as a UCHII candidate is to satisfy both: $\log(S_{25}/S_{12}) \geq 0.57$, and, $\log(S_{60}/S_{12}) \geq 1.3$, where S is the flux at the relevant wavelength. If a source satisfies both equations it is considered a UCHII candidate.

Both Schutte and van der Walt looked for 6.7 GHz methanol masers towards IRAS sources which satisfied this criteria. Schutte looked at 235 and found 35 methanol masers. Three of these were later found to have an associated H_2O maser, and two an OH maser. Van der Walt searched 520 sources to reveal 31 methanol masers. Between them 755 IRAS sources were targeted to search for 6.7 GHz methanol masers, revealing only 66 (a detection rate of ~9%).

More recently, Szymczak et al. (2000), and Szymczak and Kus (2000) used the IRAS point source catalogue to colour select sources and targeted 1399 IRAS sources to search for 6.7 GHz methanol masers. They achieved a detection rate of 13%. Several of the methanol masers were found to have sources with colours outside the range normally accepted for UCHII regions. This led Szymczak et al. (2002) to conclude that using IRAS colour selected sources underestimates the number of methanol masers by a factor of 2.

Contrary to this, Walsh et al. (1997) searched for 6.7 GHz methanol masers

towards 535 colour selected IRAS sources, and once again the Wood and Churchwell criteria was used. They found evidence of 201 methanol masers, a detection rate of 38%. In 1998 they carried out follow up observations of their 1997 sample and found a detection rate of 25%. They found that the size of the UCHII regions associated with methanol masers are generally smaller than those without, suggesting that such regions are possibly younger.

These surveys, together with Ellingsen et al. (1996), found that not all the IRAS sources associated with 6.7 GHz methanol masers had IRAS colours indicative of UCHII regions. This, and the low detection rates of methanol masers towards IRAS identified UCHII regions, led to the conclusion that targeting colour selected IRAS sources alone is not an efficient way of finding methanol masers.

Ellingsen (2007) performed a GLIMPSE[1] based search for 6.7 GHz methanol masers, targeting 200 sources that were either bright at 8μm, or had extreme [3.6]-[4.5] colours. It was thought that these sources would likely be young high mass star forming regions. The prediction that these 200 sources would yield $\sim$20 new masers within 3.5 arcsec was based on earlier work (Ellingsen 2006), where known methanol masers were associated with the GLIMPSE point source catalogue. It was found that approximately two thirds of the 6.7 GHz methanol masers which had been detected as part of untargeted searches of the Galactic Plane were associated with a GLIMPSE point source. Such sources were typically bright in the 8 μm band and had very bright mid infrared colours. More accurately, it was noted that $\sim$10% of GLIMPSE sources that satisfied both: [8] $<$ 10, and, [3.6] - [4.5] $>$ 1.3, were associated with methanol masers. It was also found that targeting these

[1]The GLIMPSE (Galactic Legacy Infrared Mid-Plane Survey Extraordinaire) survey was made with the Spitzer Space Telescope. The survey covered 4 wavelengths from 3.6 to 8.0 μm with a spatial resolution of 1.4 - 1.9 arcsec and covered $|b| \leq 1^\circ$ and $10^\circ \geq |l| \leq 65^\circ$ (Benjamin et al. 2003).

sources would have led to the detection of more than 80% of all methanol masers in the region.

From a list of 200 GLIMPSE sources, only 9 new 6.7 GHz methanol masers, from a total of 38 were found. Only 6 of these 9 were within 3.5 arcmin of a methanol maser and only 1 was within 1 arcmin. One suggestion for the poor detection rate (only 30% of the predicted rate was achieved) was that the GLIMPSE sources targeted are at an evolutionary stage before the phase associated with methanol masers. Another was that they are not regions of high mass star formation at all.

1.6.4 Methanol Masers and High Mass Star Formation

The evidence of various surveys led to the conclusion that 6.7 GHz methanol masers, together with H_2O masers, were associated with high mass protostellar objects (HMPOs), hot molecular cores and UCHII regions. Water masers are also associated with molecular outflows from low mass protostellar objects, so only 6.7 GHz methanol masers are *uniquely* associated with these stages of early high mass star formation. Although the evidence for methanol and water maser association with high mass star formation (HMSF) is compelling, it is still unclear which phenomena they trace: molecular outflows, accretion disks or the infalling material. This is further complicated by the overlapping of these stages. For example a HMPO can contain a hot molecular core or an HCHII region. Various VLBI studies of water masers over various epochs have allowed proper motions of them to be determined, and have suggested that they trace the outflows of molecular material from the massive star, as they do with the lower mass stars.

After making VLBI observations of a single young massive protostellar object which is associated with both water and 6.7 GHz methanol masers, Goddi et al. (2007) drew the conclusion that the H_2O masers were tracing the base of the protostellar jet, while the methanol masers were tracing infalling material onto the protostar.

Previous studies have tried to predict regions that contain methanol masers, be it by IRAS, GLIMPSE or MSX colours. These have largely been unsuccessful. That is the justification for the Methanol Maser Multibeam (MMB) Project, the focus of which makes up the second half of this thesis. In the MMB project we reverse this strategy and use an unbiased search method for methanol masers, and then follow this up with mid and far infrared studies.

1.7 Thesis Overview

In this thesis I present a study of high mass star formation using far infrared and radio techniques. Chapters 2-4 discuss a new far infrared camera, THUMPER, which was designed and built in Cardiff. THUMPER worked in the far infrared at 200 μm. Chapters 5 and 6 describe a radio survey for methanol masers.

Chapter 6 further discusses comparisons between the radio and infrared data. However, due to technical and political problems with THUMPER, it was not possible to carry out follow up observations with this instrument. Therefore the ISO data archive was used to obtain the infrared follow up data. Chapter 7 summarises the main conclusions of the thesis.

Chapter 2

A Description of THUMPER

2.1 Why are ground based 200 μm observations needed?

2.1.1 Science Motivators

Observers of star formation objects, such as pre-stellar cores and protostars, are currently lacking high resolution continuum observations of dust thermal emission at far-infrared wavelengths. This is needed because the submillimetre flux from an optically thin source is a function of both density and temperature. Current techniques to solve this hold the temperature of this object constant over it's full extent, so that variations in the submillimetre flux can be attributed to spatial density fluctuations. In most cases however this is not a good assumption, as spatial variations of temperature exist, necessitating an independent measure of temperature. To accurately estimate the temperature of an object, measurements

either side of where the Planck function turns over are required. For early stage star formation objects with temperatures ranging from 10 K to 50 K, this turn over is between 100 μm and 200 μm. Therefore highly spatially resolved measurements at these wavelengths are needed, to match data from instruments such as SCUBA which measures the Planck function at longer wavelengths.

As well as the birth of stars, observations at 200 μm will provide improvements to the study of stars further into their life. The processes involved in the mass loss histories of late-type stars are, at present, poorly understood. Once again, information on the spatial distribution of dust around these objects are hindered by the degeneracy between temperature and density measurements.

2.1.2 Atmospheric Considerations

Observations in the sub-mm are hindered by the atmosphere to such an extent that it constrains which wavelengths can be used to observe. For example, the 850 μm and 450 μm bands of SCUBA take advantage of the existence of so called "windows" of relative transparency in the atmosphere at these wavelengths. Figure 2.1 contains a plot of modelled atmospheric transmission at Mauna Kea which has been calculated with a precipitate water vapour (PWV) content of 0.5mm (Hayton (2005)).

It had previously been predicted, by several atmospheric models, that a similar window of transmission would open up around 200 μm under the driest conditions at sites such as Mauna Kea, Atacama and the South Pole. Measurements at 200 μm have never been made of the atmosphere at Mauna Kea under observing conditions that THUMPER would use, and there is also a level of disagreement between

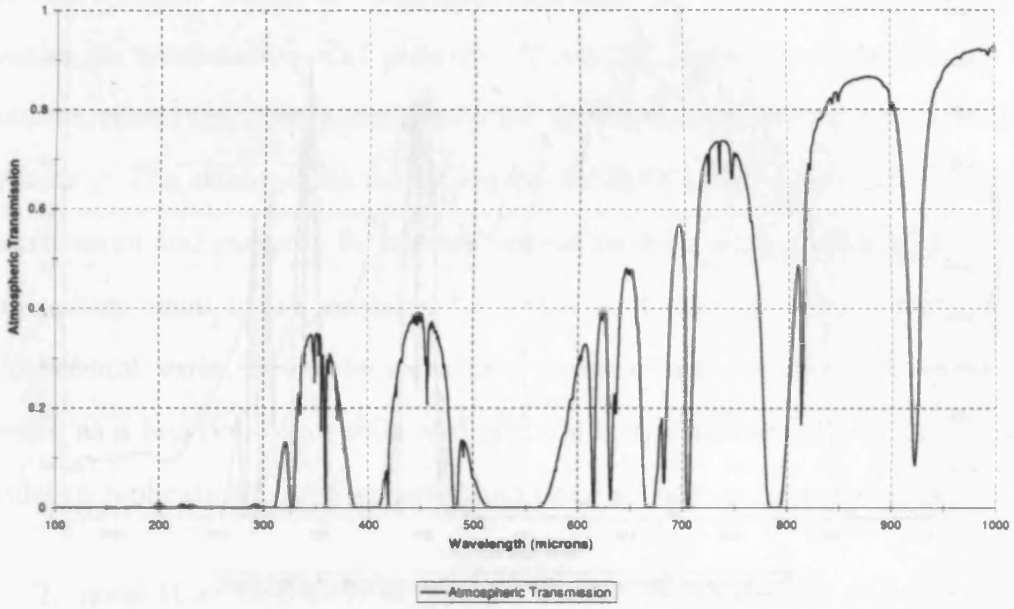

Figure 2.1: Modelled plot of atmospheric transmission at Mauna Kea with observing conditions of PWV = 0.5 mm

existing atmospheric models, about the exact amount of atmospheric transmission, which stems from differences of several model parameters such as concentration profiles and continua (Pardo, Cernicharo, & Serabyn (2001)).

This motivated the development of an accurate atmospheric model by the THUMPER team. An accurate atmospheric model is essential for successful observations for two reasons. Firstly, it allows the estimation of how often there are suitable observing conditions from specific telescope sites. Secondly, it enables calculation of the exact width of any window of transmission. The 200 μm window is defined by very strong H_2O lines which makes it important to minimise any background radiation incident upon the detectors from the opaque sky. This means that THUMPER needs closely matched optical filtering, to ensure that the radiation reaching the detectors is from the region of the spectrum that is transmitting. Figure 2.2 demonstrates this matching. Note that the atmospheric transmission plot is a detail of Figure 2.1. Having a model that can accurately calculate the exact

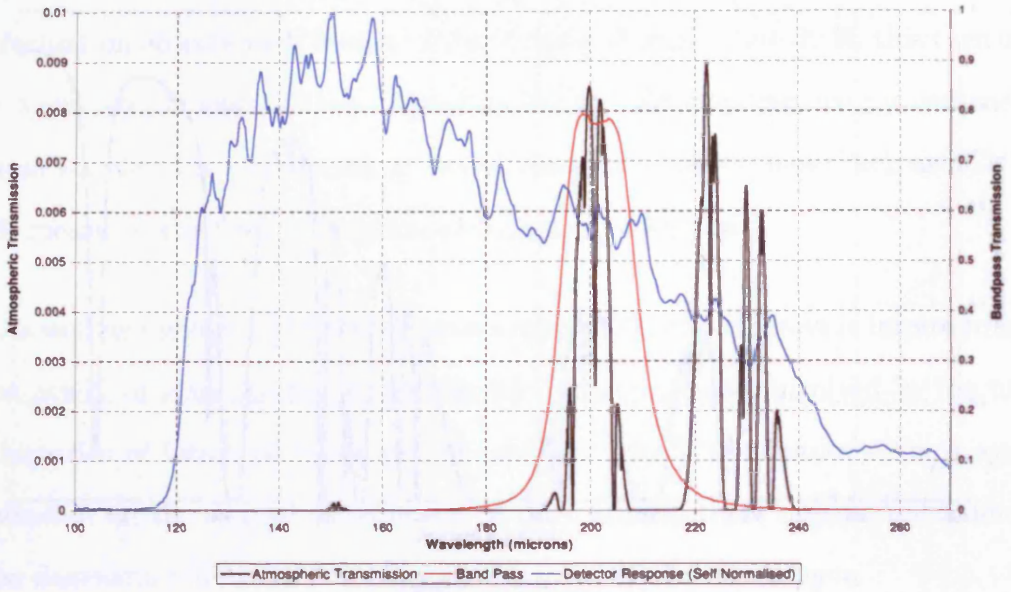

Figure 2.2: Transmission of THUMPER's band pass filter overlayed upon modelled plot of atmospheric transmission at Mauna Kea

frequency and spectral bandwidth of transmission enables this close matching.

Rotational transitions of H_2O are the dominant process of absorption in the atmosphere at 200 μm. Although O_3 and O_2 also play a role, they can be considered as being fairly constant under varying atmospheric conditions.

Observations at 200 μm are so limited, as demonstrated in Figure 2.1, that they are only possible from a few sites worldwide in the driest possible conditions when the windows of transmission open up.

2.2 Atmospheric Model

Construction of the atmospheric model is conceptually simple though computationally intensive. All the known lines for the major species in the Earth's atmosphere

are contained in databases, together with their strength, frequency and dependencies on temperature and pressure. Coupling this with a selected line shape function allows the absorption loss to be calculated using the line data for a given frequency. The atmospheric model applies Kirchoff's law to calculate the expected transmission and emission for a given optical path by setting the absorption of the atmosphere equal to it's emission for a specific frequency. The model also takes into account variations of temperature, pressure and concentration of molecular species as a function of altitude and latitude in the atmosphere. This enables the model to replicate the atmospheric conditions at various telescope sites.

To make this calculation simpler the atmosphere is divided into many parallel planes and the extinction and emission is calculated for each layer. For any given plane the planes between it and the observer need to be considered because, for example, the emission from that layer will be attenuated by the planes below it. The intensity of radiation received at the surface of the Earth is the sum of the intensities from each layer with these attenuation and emission effects accounted for.

The atmospheric modeling code is dealt with in more detail by Araujo et al. (2001) and Walker (2003). An outline of the main points shall be provided here.

2.2.1 Molecular Database

Accurate data on the relevant molecular transitions are required for accurate calculations of the transmission of the atmosphere. The High Resolution TRANsmission molecular absorption database (HITRAN) provides data for over a million spectral lines and is utilised in the calculation of emission and transmission of the

atmosphere. Only the molecules with the strongest absorption at the relevant frequencies need to be used, and the HITRAN Atmospheric WorK Station (HAWKS) extracts these from the HITRAN database. Seven "major absorbing molecules" (Anderson et al. (1986)) were chosen: H_2O, O_2, O_3, CO_2, N_2O, CO, and CH_4 as well as their significant isotopes.

2.2.2 Line Profiles

Transition data from the HITRAN database is idealised to that of a single frequency, when in reality the lines are broadened by several processes. Many different line shapes have been used by atmospheric models to reflect this, with differing approaches being applied to different spectral regions. The two dominant forms of line broadening are pressure broadening and Doppler broadening.

Pressure broadening, also known as Lorentz broadening, is due to the reduction of the lifetime of the excited state for molecules through collisions (Salby (1996)). Doppler broadening results from the natural velocity distributions of the atmospheric molecules. This line shape is derived from the Boltzmann probability distribution and is a Gaussian distribution (Salby (1996)).

At a height of less than 30 km above sea level, where the atmospheric pressure is greater, pressure broadening dominates. But in the higher atmosphere pressure decreases exponentially, so that at a height of 70 km, Doppler broadening is the dominant term.

The atmospheric model that was developed by the THUMPER team uses the Voigt line profile, a convolution of the pressure and Doppler profiles (Pardo et al. (2001)), in the regime where the two effects are comparable. It is applied to all

the lines. Water is additionally treated with a continuum correction.

2.2.3 Continuum Correction

It has long been known that line by line calculation of the atmospheric absorption fails to account for all of the observed atmospheric losses. This is most noticeable in the window regions as an excess absorption (e.g. Rice & Ade (1979) and does not appear to be associated with missing lines or species from the molecular database, but could be an effect of using an incorrect line profile. It is common to correct for this by adding an empirically verified continuum term to the absorption coefficient.

Initial correction terms were dependent on the temperature and pressure of the atmosphere together with the water concentration (Zammit & Ade (1981)). This was improved upon when it was realised that there are actually two correction terms involved (Pardo, Serabyn, & Cernicharo (2001)). The first is known as the wet correction term and comes from interactions involving H_2O. The second is known as the dry correction and comes from interactions of N_2 with O_2 and O_2 with O_2. The dry correction term has been determined at Mauna Kea by measuring atmospheric emission during very dry periods, then comparing this with measurements taken with near identical atmospheric pressure and temperature, but greater PWV.

The dry correction is an order of magnitude lower than that for wet when there is a PWV content of 1 mm. This correction method is quite complicated and loses validity above 1 THz as the frequency under consideration approaches the strong absorption band at 2.4 THz (80 cm^{-1}).

The model developed by the THUMPER team applied a Clough correction

(Clough, Kneizys, & Davies (1989)) which only takes account of absorption of far-wing line features due to water. This is achieved by letting 25 cm^{-1} about the centre of the water line equal to the value it is at that frequency, but truncating it out side of that 50 cm^{-1} region.

The continuum correction is then calculated from summing all the far-wing contributions from all the water lines in the frequency range under consideration.

2.2.4 Scaling Profiles

For the model to be applied to different observing sites it is important to know how temperature, pressure and molecular concentrations vary with altitude and season at the latitude of the site. The Air Force Geophysical Laboratory (AFGL) has a molecular database which contains sets of model atmospheric profiles of major, minor and very minor constituent particles as well as temperature and pressure profiles (Anderson et al. (1986)).

The AFGL database contains data from 0 to 120 km for latitudes at the tropics (15°), mid-latitude(45°), sub arctic (60°) and a standard US atmosphere (45.5°). Both summer and winter data is in the database for the sub-arctic and mid-latitudes.

This model database fared well when comparing pressure and temperature profiles with radiosonde data. Radiosonde are launched regularly from Hilo airport which is at sea level and lies approximately 40 Km to the southeast of Mauna Kea. There was some discrepancy between the radiosonde data and the calculated water concentration values above the troposphere, but this was attributed to an error with the radiosonde measurements. This has been observed before in

Antarctic experiments (Chamberlin & Bally (1995)) and is believed to arise from a hysteresis effect in the carbon hygrometer used to take relative humidity readings. Considering that the PWV is expected to be fairly constant above the tropopause this is not considered important. It is the highly variable tropospheric PWV that it is essential to account for. The net result is that the atmospheric model developed by the THUMPER team assumes that above the tropopause the PWV is constant and applies a scaling function to the PWV in the stratosphere. The AFGL database also contains data on O_2 and O_3 scaling.

2.3 THUMPER Design Constraints and Overview

2.3.1 Design Constraints

THUMPER was designed to become a common user instrument at the JCMT and to be run in tandem with SCUBA. These requirements placed a large number of constraints on the design.

The first and most important constraint was the atmosphere, which posed a number of operational and design problems. The atmosphere has only 20% transmission, at 200 μm, during good conditions, so the optical efficiency of the detector system had to be maximised. The atmosphere also provides a very bright background, so the out-of-band rejection and stray-light blocking had to be extremely efficient.

The second constraint was the speed of operation. Because the atmospheric conditions that allow THUMPER to be used are unpredictable and vary rapidly, THUMPER had to be ready to observe at all times and as quickly as possible. This

meant it had to be kept at operational temperature, and any procedures required to power it up needed be quick and efficient.

The third constraint was the volume of space available to THUMPER on the Nasmyth platform. This was extremely tight, so THUMPER had to be a very compact instrument that would not block access to any other instrument or to the receiver cabin.

The final major constraint was that THUMPER had to be operated simultaneously with SCUBA, to in effect be considered an extra SCUBA channel. This meant that THUMPER had to be designed to match SCUBA's observational mode.

All of these constraints must be considered when studying the design of THUMPER.

2.3.2 Instrument Overview

THUMPER is a 200 μm photometer that has been designed to take advantage of an atmospheric window that develops around this wavelength under the driest conditions at high altitudes. It is a cryogenically cooled array of seven stressed Gallium-doped Germanium photoconductors and was designed for use on the James Clark Maxwell Telescope (JCMT).

The cold plate (Figure 2.3) holds the components for the experiment. The detector array, illuminator for internal calibration, cold optics, thermometer and junction field effect transistors (JFETs) are thermally coupled to the cold plate.

THUMPER's cryostat is a modified version of the QMC Instruments Ltd TK-1865 cryostat. This consists of an aluminium outer vacuum case (OVC) and liquid

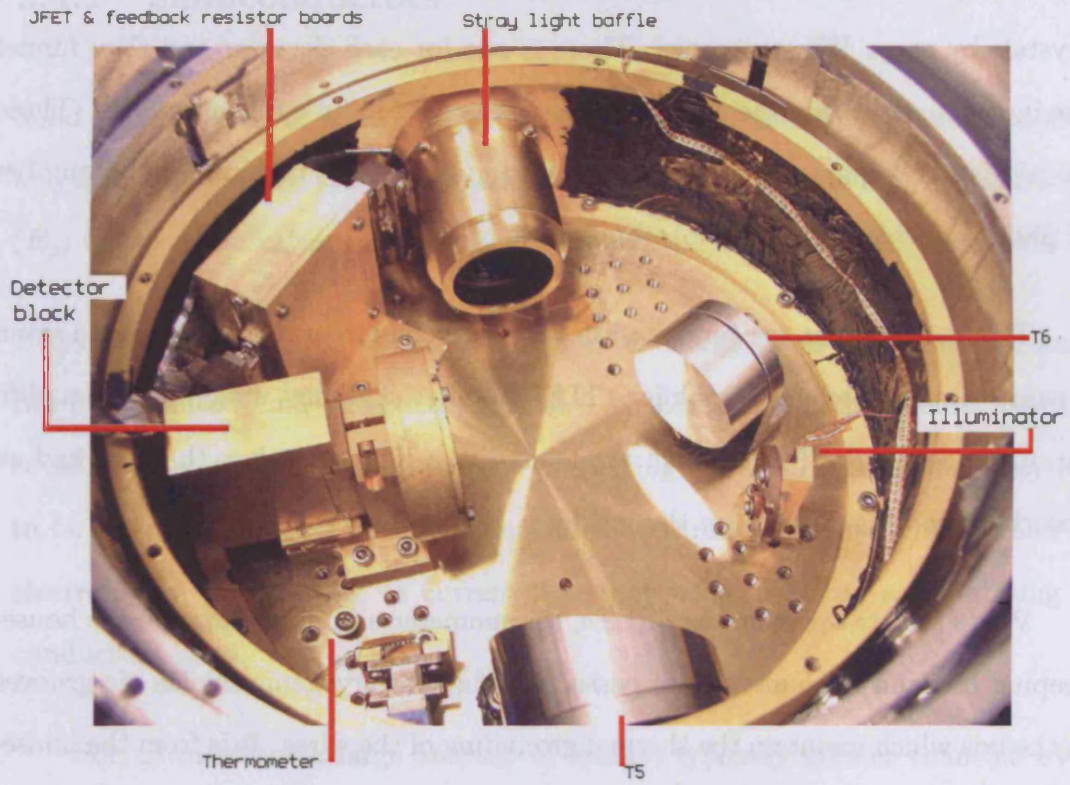

Figure 2.3: The Cold Plate of THUMPER.

nitrogen cooled shield with a stainless steel liquid helium reservoir and copper cold plate. An extra aluminium radiation shield is fitted which is cooled from gas boiled off from the liquid helium reservoir.

The modifications were necessary to accommodate the components for THUMPER's optics. Of the optical components on the cold plate, mirror T5 is used to re-image the incoming beam onto the face of the detector block via the flat mirror, T6.

In this block there are two filters: a 58 cm^{-1} Low Pass Edge (LPE) and a Band Pass (BP) filter. In combination they pass only photons of the wavelength under consideration, around 50 cm^{-1}. There are two other LPE filters within the optical path of the cryostat; these are 90 cm^{-1} filters and are on two of the cryostat stages to reject unwanted photons that increase the thermal load.

The beam that is reflected from the mirror T6 is condensed onto the detector crystals by seven Winston cones. There is one for each detector and they funnel the incoming light onto the crystals which are housed in integrating cavities. These cavities and Winston cones are smooth and gold-plated to maximise the number of photons incident on the photoconductors.

The currents that are generated in the photoconductors are read out via seven separate transimpedance amplifier (TIA) circuits. The first stage of the amplification process uses JFETs which are housed in a light-tight box that has had an absorbent coating painted on the inside.

Wires that travel from the JFETs, thermometer and illuminator to the housekeeping box and readout box are passed through the cryogenic shields via grooves in the lids which maintain the thermal grounding of the wires. It is from the housekeeping and readout boxes and ports that the experiment is controlled, monitored and measured.

2.4 Photoconductor Detectors

THUMPER uses seven stressed Gallium doped Germanium photoconductors in an hexagonal array. Photoconductors are semiconductors that have been modified so that a current flows within them when suitable photons are incident upon them. In this section the physics of semiconductors is outlined, so that the operation of THUMPER's photoconductors is understood, as are the attempts to increase their performance.

2.4.1 Semiconductors

Solid materials can be separated into three categories: conductors, semiconductors and insulators. These can be defined by their band gap, which is the energetic gap (E_g) between the valence and conduction bands of electrons in the substance.

The valence band is the highest occupied energy band for a material and is full for insulators and semiconductors at 0 K. Electrons in the valance band are covalently bound to the atom thereby preventing electrical conduction; they need to be liberated to contribute to a current flow through the material. When free electrons are contributing to current flow they are considered as inhabiting the conduction band.

For an insulator a large amount of energy, typically greater than 3.5 eV, is required to excite an electron to the conduction band and it is practically impossible for an insulator to conduct electricity. For a conductor however, the bands overlap and it naturally has the majority of valence electrons available for a current flow. A semiconductor typically requires energies less than 3.5 eV for the valence electrons to be liberated and available for conduction.

The large number of electrons that are available for current flow in conductors makes them unsuitable for photon detection, unlike semiconductors whose conductance is low at room temperature and can be significantly altered. For example, if an ultraviolet or infrared photon is incident on a semiconductor, charge carriers can be liberated. But if the same photon were absorbed by a conductor, there would be no noticeable difference in the electrical properties of the metal. To use a semiconductor as a photoconductor it is necessary to cool it so that the majority of conducting electrons are liberated through the interaction of photons.

2.4.2 Intrinsic Semiconductors as Photodetectors

Intrinsic semiconductors consist of only one substance, and conventionally the desired wavelength of observation is matched to the energy gap of the material, E_g, the gap between the conduction and valence bands. Incident photons have an energy $E_{ph} = h\nu$, and for an incident photon to excite a charge carrier it needs to have an energy greater than E_g. This gives an upper limit on the wavelength of an ionising photon, known as the cutoff wavelength:

$$\lambda_c = \frac{hc}{E_g}$$

A 200 μm photon has an energy of about 6.2 meV, so to detect this a semiconductor with an energy gap equal to or less than this is needed. Intrinsic semiconductors typically have a large E_g and respond to shorter wavelengths, so to make a photoconductor suitable for FIR observation it is necessary to find a semiconductor with a smaller band gap.

Germanium (Ge) is an intrinsic semiconductor and can be found in group IV of the periodic table, its valence shell contains four electrons and it forms a crystal structure. This structure comes from each atom sharing with four neighbouring atoms one valence electron, to form a bond with each so that it effectively has a filled valence shell.

Germanium has $E_g = 0.67$ eV, too high for far IR detection though it has long been used as a photoconductor at a wavelength of 1.9 μm and is commonly used as the host element for extrinsic photoconductors including THUMPER's crystals.

2.4.3 Extrinsic Semiconductors as Photodetectors

One technique to reduce the energy gap of a semiconductor is to add an impurity to it. Extrinsic semiconductors are comprised of an element that has had a moderate amount of another material, known as a dopant, added to it. Impurity energy levels are then introduced in to the forbidden band by the dopant, to in effect increase the cut-off wavelength by providing a potential charge carrier with lower excitation energy. There are two types of extrinsic semiconductors, acceptor or donor. The difference comes from whether the impurity atoms contribute or take an electron from the host atoms.

Donor Type

Donor types are commonly known as n-type, negative charge carriers. Elements from group V of the periodic table are used as donor type dopants for the element Germanium. These donors have five free electrons and can be considered as being host like, in the sense that the atoms of the host (Ge) have four free electrons; so they are host like with an extra electron. This extra electron does not get used up in the tetrahedral covalent bonds that the dopant atom forms with the neighbouring host atoms, and is attracted by a weak Coulombic attraction that is less energetic than the covalent bonds. The fifth electron is more readily available for conduction, with less energy required for its excitation, thus introducing a donor level in the band diagram close to the conduction band.

Acceptor Type

These are commonly known as p-type, positive charge carriers. Elements from group III of the periodic table are used as acceptor type dopants for Germanium. They have three free electrons and are unable to complete the covalent bonding: such that the acceptor atom accepts a valance electron from a neighbouring host atom. This leaves a mobile "hole" in the lattice where an electron should be. The hole in the lattice is bound to the neighbouring atom by weak Coulomb attraction and introduces an acceptor level in the band diagram near the valence band edge.

2.4.4 Stressed P-type Photodetectors in THUMPER

The photoconductors that are used by THUMPER are extrinsic p-type Gallium doped Germanium and were grown in February 1970 at the Lawrence Berkley National Laboratory. They have a Ga dopant level of 1.7×10^{14} cm^{-3}, with compensating donors of 2.0×10^{12} which are thought to be phosphorous.

Compensation donors are needed because other impurities are present that have very low excitation energies. For example, the group III element Boron, is difficult to eliminate from the doping process and has a band gap that equates to 119 μm, comparable with the 115 μm of Ge:Ga. The compensating donors reduce thermal excitation of these unwanted impurities by being of the opposite type, so to compensate Boron, p-type, an n-type impurity needs to be introduced to capture unwanted charge carriers.

Doping and compensation levels need to be carefully considered and monitored. Too high a concentration of dopant can lead to tunnelling between the

impurity atoms known as hopping conduction. Too much donor compensation can lead to scattering, as well as the rapid capture of photo-excited charge carriers. It is widely considered that achieving a photodetector which balances those two affects is a process of initial trial and error, until the optimum method and quantities are established.

Ge:Ga has an unstressed long wavelength cutoff of 115 μm, and the desired wavelength of operation for THUMPER is 200 μm. To extend the cut off wavelength beyond 115 μm a uniaxial stress is applied to the crystal in the <100> direction, along the crystallographic axis. This can be considered as putting a strain on the inter atomic bonds, such that the energy to ionise a donor atom is lower.

Stressing the crystals makes it possible to ionise an acceptor atom with lower energy than without the stress. This energy could equally come from thermal mechanisms which increases the dark component of the noise. The carrier wavefunction is also extended with the application of stress. This increases the overlap between the neighbouring impurity atoms, increasing the possibility of tunnelling and the dark component of the noise.

2.5 Photoconductor Parameters and Figures of Merit

For a photoconductor to detect light three independent processes occur. Firstly, an incident photon ionises a majority dopant which leads to a free charge carrier. This carrier becomes mobile in the presence of an externally applied electric field,

E, and remains so until its recombination with an ionised majority impurity.

The average distance (l) that a free charge carrier drifts is:

$$l = \mu E \tau \tag{2.1}$$

where μ is the carrier's mobility and τ is the average charge carrier lifetime. The mobility of the charge carrier relates the drift velocity (v_d) with the applied electric field (E) by the relation $v_d = \mu E$. When a photon stream falls upon a photoconductor a signal current, I_s, is formed:

$$I_s = e\dot{N}\eta_{rq}\frac{l}{L} \tag{2.2}$$

where e is the charge of an electron, $\dot{N}$ is the number of photons incident upon the detector per second, η_{rq} is the RQE, responsive quantum efficiency, and L is the inter electrode distance (the width of the detector). The ratio $\frac{l}{L}$ is commonly known as the photoconductive gain, G, and is the ratio of the carrier lifetime to the carrier transit time:

$$G = \frac{l}{L} = \frac{\tau}{\tau_t}$$

The probability that an incident photon will create a charge carrier that migrates to an electrode can be written as $\eta_{rq}G$. From this it can be seen that there is an advantage to minimising the distance between the electrodes and hence the dimensions of the detector.

2.5.1 Responsive Quantum Efficiency

The RQE is the fraction of incident photons that enter the detector and are absorbed by photo-ionisation. It can be thought of as the product of the optical efficiency, which defines the chances of a photon entering the crystal, with the efficiency of photo-ionisation, the probability that a photon which has penetrated the crystal liberating an electron. It is also known as the detective absorption (Bratt (1977)) and is defined as:

$$\eta_{rq} = 1 - \exp(-a(\lambda)z) \tag{2.3}$$

where z is the typical photon path length and a(λ) is the absorption coefficient:

$$a(\lambda) = \sigma_i(\lambda)N_a \tag{2.4}$$

in which $\sigma_i(\lambda)$ is the cross section of photoionisation and N_a (m^2) is the number of acceptor impurities per cubic metre.

Equations 2.3 and 2.4 show that to increase the RQE of a photoconductor it is necessary to increase the size of the detector and number of acceptor impurities. There are physical limits to the increases that can be made to these quantities before there is a degradation of performance. Ways of *effectively* increasing these values exist however, and these shall be explained in section 2.6.2.

The number of impurity atoms that can be placed in the host lattice is limited by two effects. The first is the maximum solid solubility of the impurity in the host

which, when reached, introduces crystalline imperfections such as dislocations. According to Bratt (1977) however, the detector performance is so strongly degraded by these imperfections that a practical limit of half the maximum solubility is used. Secondly, too many impurity atoms leads to the electron "orbits" of neighbouring impurity atoms overlapping, but again before this limit is reached a drop in detector performance is observed. This is manifest as a reduction of detector resistance, and a large increase in detector dark current, which arise from hopping conduction. This is when a loosely bound charge carrier tunnels to an adjacent empty impurity site. This form of conduction is dependent on temperature in addition to impurity concentrations.

The desire to maximise the photoconductive gain (G) means that there is an equal desire to limit the physical dimensions of a detector. This coupled with the need for the detector to be uniformly illuminated results in the typical dimensions of crystals that are seen, $\sim$1 mm^3.

2.5.2 Responsivity

As well as the figures of merit η_{rq} and G, there is also the responsivity that can be used to define the performance of the detector. The responsivity, S, is simply the output signal, which can be measured as either current or Voltage, that is generated per unit Watt of incident power. That is

$$S_I = \frac{I_s}{P} = \frac{\eta \lambda q G}{hc} \qquad (A/W) \qquad (2.5)$$

where P is the photon power and $h\nu$ is the energy of individual photons.

A doubling of the responsivity of stressed Ge:Ga relative to unstressed Ge:Ga would be expected, simply from the incident photons at 200 μm being less energetic than those at 115 μm. However, increases up to factors of ten have been reported in the literature (e.g. Haller (1993)). These further increases in responsivity are attributed to an increase of carrier mobility and lifetime from the increase in stress. It is assumed that the lifetime increases are a result of the changes in the ground state and the bound excited state spectrum of the Ga acceptors in the stressed Ge. Equations 2.1 and 2.2 together with 2.5 illustrate that it is likely that the extra responsivity can be attributed to an increase of the mobility and average lifetime of the free charge carriers.

2.5.3 Noise Equivalent Power

There are a number of processes that introduce noise into the photocurrent, and it is the intention of the following figures of merit to give a feel for how limited the detector is by these.

The noise equivalent power (NEP) can be defined as the photon power which produces a signal current I_s, in an integration time of half a second, that is equal to the quadratic sum of all the noise currents in an electrical band width of 1 Hz. It is commonly written as:

$$NEP = \frac{P_s(2\Delta t_{int})^{(1/2)}}{(S/N)} \qquad (W/\sqrt{Hz}) \qquad (2.6)$$

where P_s is the signal power incident on the detector, t_{int} is the time interval of measurement and S/N is the signal to noise ratio.

For an ideal detector, which has $\eta_{rq} = 1$, the only noise in the photocurrent is that which comes from fluctuations in the photon stream ($\dot{N}$). This leads to a definition of the background limited power NEP_{BLIP}:

$$NEP_{BLIP} = \sqrt{2(2\dot{N}_{total})(h\nu)^2} \tag{2.7}$$

The noise in the photon stream is simply $\sqrt{\dot{N}}$, and the factors of two come from shot noise and the distribution in the mean free paths of the individual photogenerated free carriers.

2.5.4 Detective Quantum Efficiency

These definitions of NEP are non-rigorous but are just introduced here to give a feel for how we compare systems in the following figure of merit, the detective quantum efficiency (DQE). The DQE (η_{dq}) shows how the measured performance of a photoconductor NEP_{meas} deviates from that of a background limited photoconductor and can be defined as:

$$DQE = \left(\frac{NEP_{BLIP}}{NEP_{meas}}\right)^2 \tag{2.8}$$

2.6 Detector Block

THUMPER's p-type photoconducters, and the mechanism for stressing them, are housed in the detector block (see Figure 2.4) which is thermally coupled to the

cold plate. Winston cones and integrating cavities are also within this block and are used to maximise the number of photons incident on the detectors by coupling the detector to the telescope. At the entrance of the detector block is a band pass filter to ensure that only photons of the correct wavelength fall upon the detectors.

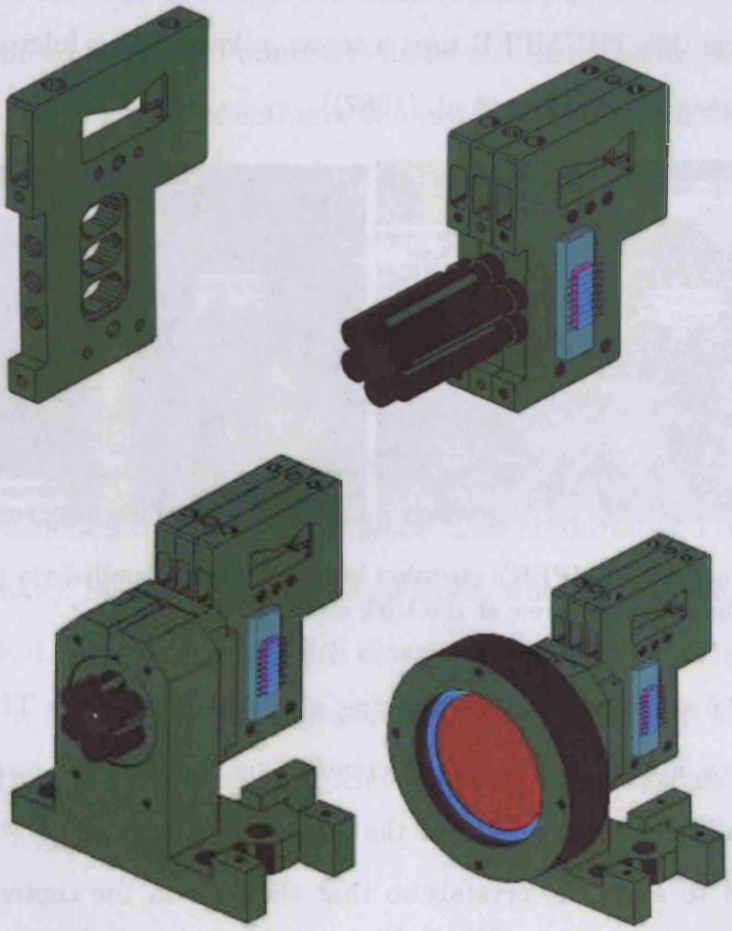

Figure 2.4: The THUMPER focal plane array: (top left) a stressing block in which the crystals are mounted; (top right) the three stressing blocks fixed together to form the focal plane array, with feed-horns on the front of the detectors; (lower left) the focal plane array mounted on its stand; (lower right) the complete array and mount with the filter stack mounted on the front.

2.6.1 Stressing Block

For a Ge:Ga crystal to be responsive to 200 μm radiation, large forces need to be applied, which, to maximise the volume of crystal available for detection, must be applied uniformly across the crystal. Various techniques have been employed in the past to achieve this THUMPER uses a screw, a lever and a fulcrum, a technique that was pioneered by (Wang et al. (1987)).

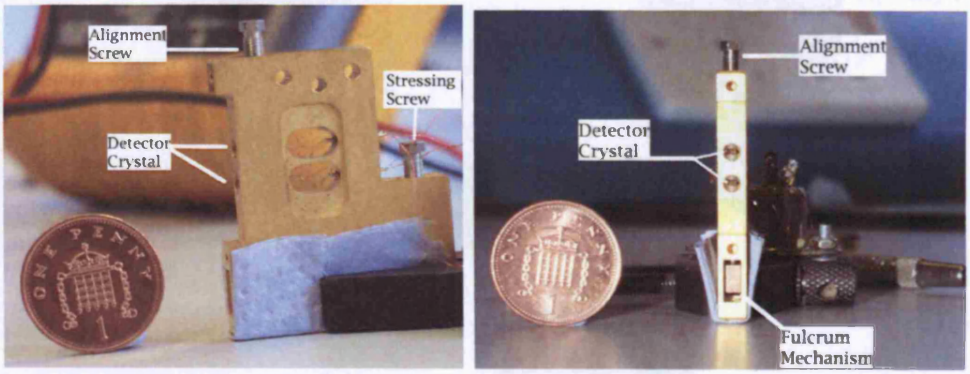

Figure 2.5: One of THUMPER's stressing blocks. Stress is applied via a fulcrum mechanism using the stressing screw at the back of the block.

Figure 2.5 shows one of the stressing mechanisms used by THUMPER. The stressing screw applies stress to the crystals via the fulcrum mechanism. This mechanism allows the torque from the screw to be decoupled. The alignment screw is used to align the crystals so that they are in the centre of the cavity. The Winston cones, which will be discussed below, are positioned in front of the crystals. There is one for each crystal.

2.6.2 Integrating Cavities and Winston Cones

Winston Cones

Winston cones are used to couple the small (1 mm^3) detectors to the larger telescope point spread function. Parameters under consideration in the design of Winston cones are the diameter of entrance and exit apertures, separation of cones and the maximum angle which the cones will receive light from. The opening aperture defines the amount of sky that each detector will see, and the separation of cones affect the beam separation on the sky.

THUMPER was intended to be operated in tandem with SCUBA. That is, it was designed to take data simultaneous with SCUBA and use the data acquisition (DAQ) and reduction chain already in place. This necessitated THUMPER to be designed to match SCUBA's observational mode, which places the requirement of a closely packed hexagonal array with detector to detector spacing of $2F\lambda$. Conventionally λ is the wavelength of operation, but for THUMPER's Winston cones the wavelength of 450 μm is used, which enables the beam spacing of THUMPER to match the 450 μm channel.

Additionally, the entrance aperture of the Winston cones are over sized compared to the diffraction limited 200 μm beam to compensate for the large scattering of the point spread function by surface inaccuracies of the JCMT primary mirror. Ruze theory indicates that the likely percentage of power in the primary beam is

$$\eta_R(\epsilon, \lambda) = \exp(-\left[\frac{4\pi\epsilon}{\lambda}\right]^2) \tag{2.9}$$

where ϵ is the surface accuracy of the primary mirror and λ is the wavelength of radiation. The JCMT primary mirror is good for the wavelengths that SCUBA observes at, with Ruze efficiencies of around 88% and 64% for the 850 μm and 450 μm beams respectively. But with surface accuracies of about 24 μm being measured (Wouterloot 2005), the predicted THUMPER primary beam is predicted to contain only 11% of the available light. The remainder of the light makes up an extended error pattern that the oversized Winston cones attempt to capture. In this situation the Winston cones can be thought of as "light buckets" with the THUMPER detectors not being diffraction limited, but having an effective angular resolution of 14".

Limits are placed on the diameter of the exit aperture to minimise losses, while at the same time not diffracting the 200 μm radiation. The exit apertures are extended and shaped so as to direct the radiation, which would otherwise be diffuse, onto the detector crystals. Figure 2.6 shows a schematic of the Winston cone, detector crystal and integrating cavity. This diagram is looking down on the detector, so the stress that is applied (via the screw/fulcrum mechanism), is perpendicular to the page; so, in THUMPER's array of crystals, there is another crystal stacked on top of it (see figure 2.5).

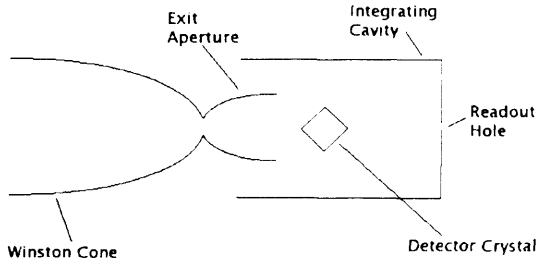

Figure 2.6: Schematic of one of THUMPER's Winston cones. Stress is applied perpendicular to the page.

Integrating Cavities

Not all of the photons that are incident upon the detector will be absorbed, a fraction (r) of the photons are reflected back from the crystal face

$$r = \left(\frac{n-1}{n+1}\right)^2$$

where n is the refractive index of the material. For Ge:Ga, n is 4, so 36% of incident photons are reflected from the crystals (Wang1986).

Additionally, not all of the photons that penetrate the detector will ionise an acceptor atom, the probability of this happening is dependent on the absorption coefficient a(λ), which has been defined in equation 2.4.

The absorption length is the reciprocal of a(λ), so the effect of increasing the doping levels of the detectors is to decrease the length of material required for (an average) photon absorption. As stated in section 2.5.1 there are practical limits for amount of dopant that can be added to a host, so to increase the chances of photo-ionisation, a physically longer detector is needed.

For the THUMPER detectors the approximate values we have to determine the absorption length are as follows. The cross section of ionisation of Gallium (Ga) is 1.0 x 10^{-14} cm^2, and it is estimated that the level of Ga doping in the THUMPER crystals are approximately 1.7 x 10^{+14} cm^{-3}. This gives an approximate absorption length of 5.8 mm for the THUMPER crystals which is considerably greater than the cubes of 1 mm that are used.

The reason for this is that it is preferred to use crystals of a cube shape, while

there are gains in minimising the the inter-electrode distance (perpendicular to the photon stream). It is preferable to have a cube shape, to ensure uniform illumination; and decreasing the inter-electrode distance increases the photoconductor gain.

It is possible to effectively increase the size of the crystal by housing the photoconductor crystal in an integrating cavity. This comprises specifically angled highly reflective material which increases the number of passes each photon makes through a crystal. To further increase photon absorption, the face of the crystal perpendicular to the incoming photon stream is angled, as shown in figure 2.6.

This shape of crystal is known as roof type, end-fire, flat-roofed or bevel-ended crystal and increases the chances of photon absorption through total inner reflection. Wang et al. (1986) found that the average internal path length increased by a factor of 4.1 for a bevel angle of 20 degrees. The light that is transmitted through the cones is diffuse (2π steradians) increasing the need for the integrating cavity.

Both the Winston cones and the integrating cavities are smoothed after construction and then gold plated to a high quality finish to minimise the number of photons that are absorbed or scattered before they have a chance of forming a signal current across the detector.

2.7 Readout Electronics

The charge carriers that are photo-excited in the detector start flowing as an electric current when an electric field is applied to it. This current needs to be amplified

so that it can be measured, and the incident photon flux estimated.

2.7.1 Transimpedance Amplifier

In this circuit the detector is connected to the inverting input (-ve) of an operational amplifier (op-amp), and the output of the op-amp loops back via a feedback resistor (R_f) to the same input. The current through R_f opposes the detector current (negative feedback), see Figure 2.7.

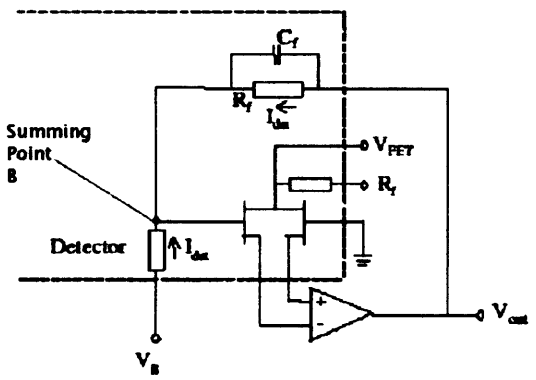

Figure 2.7: The Trans Impedance Amplifier Circuit.

The photoconductor has an electric field applied to it, and is connected to a JFET that is positioned as close as possible to the detector block so that microphonic noise is minimised (Potter (2003)). Microphonic noise, a particular problem of high impedance detectors, is a fluctuating voltage at the op-amp input that is generated by the changing capacitance of the TIA input wire. This changing capacitance is a result of the movement of the signal wire that runs to the input of the op-amp relative to the cryostat ground. The JFETs provide a relatively low impedance input to the op-amp thereby reducing microphonic noise.

The TIA circuit allows the bias that is applied to the detector to be varied, but to be independent of power loading. This is an effect of the non inverting input

(+ve) being tied to ground, and the feedback of the amplifier maintaining the voltage at the inverting input. This gives a high degree of linearity to the circuit, so that if the detector current is linear with photon flux, the output of the amplifier reflects this. The non inverting input of the op-amp is connected to ground via a JFET that is closely matched to the JFET that the detector is connected to. JFET pairs are commercially available and the pair used for THUMPER were purchased from IR Labs.

It is possible to determine the output of the TIA and justify the previous paragraph in the following way.

The +ve input of the op-amp is tied to 0 V and so the voltage at the -ve input (V_-) can be approximated as 0 V because an op-amp adjusts it's output to minimise the difference between the two inputs.

So $V_+ \approx V_- \approx 0$ V and the voltage at B is also 0 V.

At the summing point in the circuit (B) Kirchoff's law gives $I_d + I_f = I_-$; i.e. $I_d + I_f \approx 0V$. So

$$\frac{V_{out} - V_d}{R_f} = -\frac{V_b - V_d}{R_d}$$

and because $V_d \approx 0$ V,

$$V_{out} = -V_b \frac{R_f}{R_d}$$

(where $-\frac{R_f}{R_d}$ is the gain of the op-amp), so that

$$V_{out} = -I_d R_f.$$

where V_{out} is the output voltage, V_d is the voltage across the detector and V_b is the bias voltage.

As well as being able to measure the current from the detector using the output of the TIA, it is possible to measure the current across the feedback resistor. As shown above, this is equivalent to the current generated in the detector from the incident photon flux. Both these measurements are made in the following experiments.

Chapter 3

Status of THUMPER as of October 2003 and Further Experiments

3.1 Status of THUMPER and Purpose of Experiments

3.1.1 Status

When I joined the THUMPER team in October 2003 THUMPER had been designed and constructed. During the construction several assembly problems had been solved, and there was a completed detector ready for performance testing. The biggest problem that faced the THUMPER team during construction was that of microphonic noise.

One of the critical design goals was that THUMPER would have a long liquid Helium (LHe) hold time (30 days), during which it would remain in a state of "stand-by", due to the short timescales over which the weather changes at the JCMT. The JFETs that are used by THUMPER operate at a temperature of around 100 K, and it was calculated that placing the JFETs on the 3.6 K cold plate and heating them to 100 K would place a greater heat load on the LHe bath, increase boil off and ultimately reduce the hold time to an unacceptable level. To avoid this it was decided that placing the JFETs on the 77 K liquid Nitrogen (LN_2) cooled shield would reduce the amount of heating required, as well as only increasing the boil off of LN_2.

During the course of the team's investigations (Potter (2003)), it became apparent that microphonic noise was the dominant noise source, and it was decided to put the JFETs on the cold plate, thus limiting the length of high impedance wire that could move relative to the grounding shield of the cryostat and reducing any fluctuation in the voltage at the TIA input.

3.1.2 Purpose

The purpose of the experiments carried out between late 2003 and early 2004 was to monitor the performance of THUMPER's detectors, as alterations were made to improve performance. The focus of these alterations was the change in stress that was applied to the crystals. To cover the period of alterations data were taken during three separate months: September 2003, October 2003 and February 2004.

The performance was measured in September 2003 and was below the required level of 10%. It was believed that this was a combination of a poor finish of the

Winston cones and integrating cavities reducing the number of photons incident on the detectors, and variations in stress being applied to the detectors. The throughput of the horns was measured, before they were smoothed, cleaned, re-plated; to exhibit an estimated throughput increase of twofold (Ade (2003)). In October 2003 the performance was measured to again be below the minimum acceptable DQE, 10%.. It was noted that levels of (1/f) noise were high, and that the responses of the detectors were still quite low. The JFETs were replaced with low noise space qualified units and the stress of the detectors was altered. This final setup was tested from February 2004 to June 2004.

3.2 Laboratory Testing

A variety of experiments have been devised to determine the parameters that indicate the performance of a detector (e.g. Rieke & Visnovsky (1996)). The common theme of these tests is their exposing of the detectors to a known power load while measuring the current that is generated; these are then completed by an estimation of the noise level in the system.

The parameters that were measured for THUMPER's detectors are output current (mA), noise ($V\sqrt{Hz}^{-1}$) and spectral response. These enabled determination of responsivity, DQE, NEP and NEFD, which can be used to define whether the instrument is within minimum performance specification. For THUMPER this was a minimum DQE of 10%.

3.2.1 Signal and Noise Measurements

An aluminium chopper wheel is used to generate a signal on the detectors in the following manner. The wheel is placed close (about one cm) to the optical port and set in rotary motion. When the chopper is "open" the detector is exposed to ambient temperature radiation (300 K in the lab). When the blades of the chopper cover the optical port the detector sees the reflected 77 K radiation from the LN_2 stage.

This means that when the chopper wheel is in motion, the chopped output signal is the difference between the 300 K and 77 K source, which can be represented as a square wave of amplitude P_s and by the series

$$P(t) = \frac{P_s}{2} + \frac{2P_s}{\pi}[cos(\omega t) - \frac{cos(3\omega t)}{3} + ...] \tag{3.1}$$

where $\omega = 2\pi f$. The fundamental frequency (f) is the frequency of modulation, the rate of rotation of the chopper. For a cosine wave, the RMS value is the amplitude divided by $\sqrt{2}$. But from equation 3.1 the RMS power received by the detector is $\sqrt{2}P_s/\pi = 0.450P_s$.

P_s is the power that is incident on the detector from the signal that is generated by the chopper. As such it is the difference in the power on the detector from the 300 K and 77 K load (taking into account filtering). i.e.

$$P_s = P_{300} - P_{77} \tag{3.2}$$

where

$$P_T = A_{det}\Omega_{T5}\int t_{fil}(\nu)[\epsilon_{back}B(\nu,T_{BB})t_{win}(\nu) + \epsilon_{win}(\nu)(\nu,T_{win})]d\nu$$

Which demonstrates how the incident power on a detector is calculated from a blackbody of temperature T, in this instance being 77 K or 300 K. In this equation: A_{det} is the area of the detector (defined by the feedhorn entrance aperture), ϵ_{T5} is the solid angle defined by mirror T5, t_{fil} and t_{win} are the transmission function of the filters and cryostat window respectively, similarly ϵ_{back} and ϵ_{win} are the emissivities of the background and cryostat window. $B(\nu,T_{BB})$ is the Planck function.

So the responsivity of the detector is

$$S(f) = \frac{V_{rms}(f)}{\sqrt{2}/\pi P_s}. \tag{3.3}$$

Equation 3.3 allows conversion from a square wave signal to an rms value at the fundamental frequency, the constant $\sqrt{2}/\pi$ is called the waveform factor (or chopping efficiency).

These experiments allow determination of the system's S/N, responsivity, NEP, DQE and NEFD. Use of the chopper wheel removes all signal fluctuations except those higher than the modulation frequency. This is particularly useful when astronomical observations are being made since the long scale drifts that are removed include sky drifts.

The experiments that were carried out on THUMPER were variations on the

above to find the optimum operating setup.

3.2.2 AC Measurement Procedure

These measurements used the setup as described above with a signal being made up of a chop between 300 K and 77 K. Measurement of the output voltages was made using the PC based LABVIEW software.

The output from THUMPER was fed into input of the LABVIEW DAQ card via a D-type to SCSI II converter. The LABVIEW software reads from this DAQ card and performs a Fourier transform on the recorded signal to display the variation of signal/noise with frequency.

The experiments that were carried out were aimed at finding the optimum bias for each channel individually, and optimum JFET operating temperature for all channels collectively.

Bias is applied to all the of the detectors by a single signal generator, which makes it easy to quickly alter the bias so that an exploration of the effect of bias can be made. It is possible to alter the bias to individual channels using potentiometers that are part of the TIA circuitry, so each detector can be set to it's optimum bias once it has been established. For these experiments though, each channel was identically biased.

The JFET pairs are on the cold plate and need to be at a temperature of around 100 K to operate within specification. A heater is placed on the JFETs circuit board and this is controlled by another potentiometer in the housekeeping box.

With these two parameters being explored, experiments were carried out in the following manner. Once THUMPER's cold plate was at the correct operating temperature, power was applied and the JFET heaters were set to the required value and were left to warm up. Because it is easier to warm up the JFETs than cool them down, the procedure was to start at a lower temperature, take measurements, increase the temperature, take measurements and repeat this until the maximum desired temperature had been reached.

When the JFETs were stable in temperature; signal and noise measurements were made. For signal measurements the chopper was set to a modulation frequency of 8 Hz, this will be the chopping frequency used for observations. Noise measurements were made by estimating noise levels under background loading of 300 K and 77 K, at two positions of the noise spectra, 8 Hz and 80 Hz, so an approximation could be made of the levels of 1/f noise.

Signal and noise measurements were made between 0 mV and 120 mV in increments of 20 mV. At each bias increment the level of signal at 8 Hz and level of noise at 8 Hz and 80 Hz were noted from the display of the LABVIEW software and the spectral data were saved. Saving the spectral data is particularly important for the noise measurements, as the estimation of noise is rather subjective.

The LABVIEW procedure allows data sampling parameters to be altered. For signal measurements rms averaging was used and 10 averages were used to record the data. Units of signal are Volts. For noise measurements power spectra density (PSD) units are used with between 20 and 50 rms averages being taken, dependent on the level of background noise. The units of noise are then $V\sqrt{Hz}^{-1}$.

The non-differential gain of the TIA is kept at 20 and this needs to be corrected

for when comparing values of responsivities calculated by different methods. It is possible to increase the gain to 2000 and 20000.

3.2.3 DC Measurements

DC measurements are made at each JFET operating temperature. Both positive and negative biases are applied from 0 mV to the breakdown voltage in increments of 10 mV. Measurement is made directly of the voltage across the feedback resistor for each channel via the hermetic connector in the house keeping box. This measurement is made with the chopper wheel stationary, so that the response of the detector to 300 K and 77 K power loads is determined.

3.2.4 Spectral Response Measurement

A polarising Fourier Transform Spectrometer (FTS) was used to measure the spectral response of the detector. Radiation from a mercury arc lamp source passes through a fixed polariser. This reflects half of the source power back to the source. The transmitted polarised beam continues on to a polarising beam splitter, which has its polariser direction orientated at 45° with respect to the input polariser. The incident beam is therefore split into two orthogonally polarised beams one being reflected and the other transmitted. The transmitted component travels to a fixed roof top mirror orientated such that it rotates the polarised beam by 90° on reflection. The reflected component travels to a moving rooftop mirror, which also rotates the polarised beam by 90° on reflection. The different optical path traversed in this arm introduces a phase delay when the two beams recombined at the beam divider. As the moving mirror traverses, each source frequency is modulated

resulting in a characteristic cosine pattern being observed at the output. When white light is incident the output is the sum of all the monochromatic components, referred to as an interferogram. Performing a Fourier Transform on the measured interferogram reduces it to the input spectrum hence the name FT spectrometer.

The interferogram is measured directly by the detector. The output signal from the TIA readout is passed to a computer running LABVIEW software, and Fourier transformed to give the detector's relative spectral response. THUMPER's cryostat was placed so that the cryostat window was sitting next to the exit port of the spectrometer. The inside of the spectrometer was evacuated, necessary to remove the absorption by atmospheric gases such as H_2O vapour and O_2 in the optical path. The vacuum seal is effected directly onto the window of THUMPER's cryostat ensuring there is no air in the optical path.

The spectrum recorded is the intensity measured by the photoconductor from a near blackbody source (mercury arc lamp with an effective temperature of 2000 K) through the optics and filters of the spectrometer-cryostat system. To obtain the spectral response of the crystal alone a bolometric detector with a known spectrally flat absorber is used in the same cryostat on the same spectrometer. The spectrum taken with the PC is then ratioed against the bolometer spectrum to determine the spectral response of the detector.

3.2.5 Changes to THUMPER's Operational Setup

As stated in Section 3.1.2, the operating setup was altered between September 2003, October 2003 and February 2004 measurements. After the September 2003 measurements, the Winston cones were cleaned thoroughly and replated in an

attempt to increase the photon throughput. The feedback resistors in the TIA circuit were replaced with resistors of a higher value. This setup was measured in October 2003.

After the October 2003 measurements, the JFETs were replaced and the stress that was applied to the crystals was altered, for five of the crystals this was an increase. This setup was measured in February 2004 through to June 2004. As the results are presented, so shall the justifications for the above alterations.

3.3 Results and Discussion

3.3.1 Overview

The results that are presented can be summarised as follows: after the Winston cones were improved there was an increase in performance marked by an increase in DQE. The responsivity of the crystals however was not affected. There is also evidence for inhomogeneous stress being applied across the detector arrays and possibly the crystals.

3.3.2 Performance Change Between September and October 2003

DQE Results

Figures 3.1 through 3.4 hold the plots of DQE (from AC measurements) as a function of bias for each channel, each plot shows the data for one channel for all

three periods of testing. The error in the calculation of the DQE is dominated by the error in the measurement of the noise. This statement shall be examined in more detail in section 3.3.4. The errors in the DQE were calculated to be no greater than plus 1.9% and minus 1% of the DQE value.

Looking at September's DQEs it is clear that the DQEs are far too low, and visual inspection of the Winston cones led to the conclusion that the poor finish of the integrating cavities was responsible for unacceptable levels of photon loss. When the DQEs from September are compared with those taken after the cleaning in October, it is clear that a marked improvement had been made in the performance of the detectors.

Although there was an overall improvement in DQE in the October 2003 measurements, there was a variation in DQE between channels present in September 2003 that remained.

During the process of cleaning the Winston cones they were all mixed up, that is, no record was made of which horn belonged with which channel, so that it's highly unlikely that the horns would go back with their original detector. The Winston cones could therefore be ruled out as the cause of the disparity that remained between the channels in October and they could be considered as performing well.

In October, the DQEs were still below the required level of 10%. It was anticipated that whatever was causing the disparity between the DQEs of the channels was also responsible for their general low performance. All of the crystals that were used as photoconductors were cut from the same block of crystal and must therefore all have the same levels of potential charge carriers. All channels

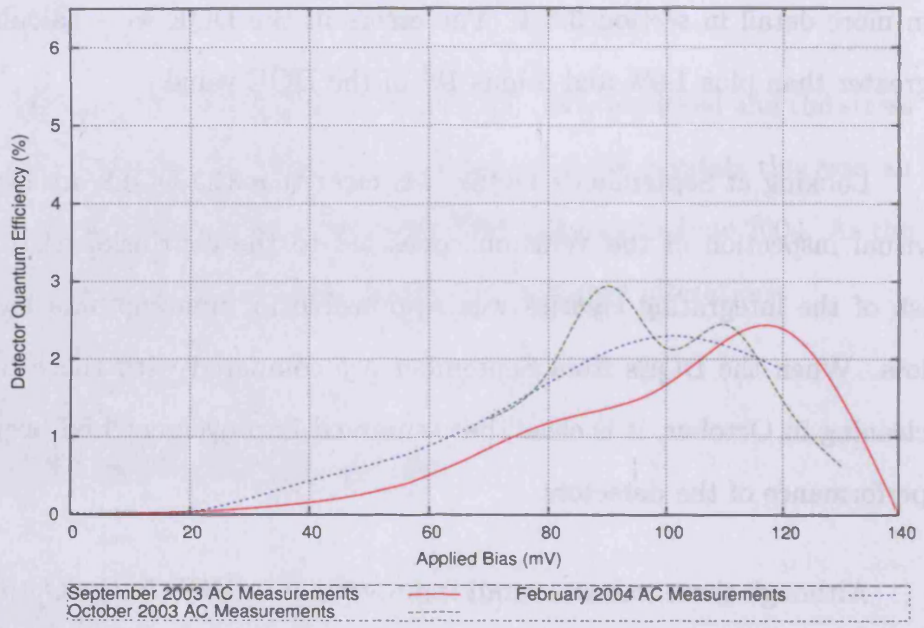

[Channel 1.]

September 2003 AC Measurements
October 2003 AC Measurements
February 2004 AC Measurements

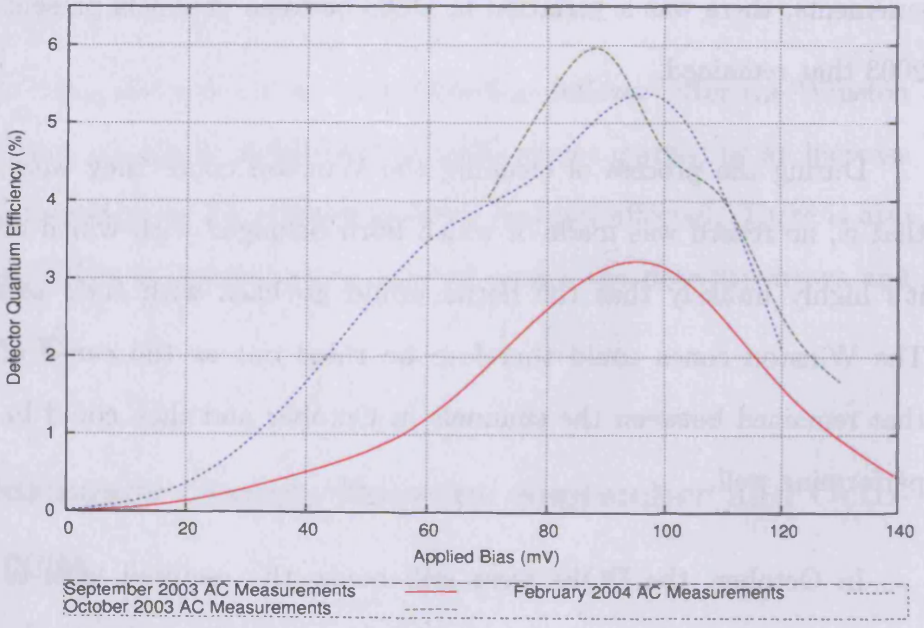

[Channel 2.]

September 2003 AC Measurements
October 2003 AC Measurements
February 2004 AC Measurements

Figure 3.1: Comparison of detector quantum efficiency (%) varying with applied bias (mV) for channels one and two. Data were taken during three seperate periods with a cold plate of 3.7 K for all.

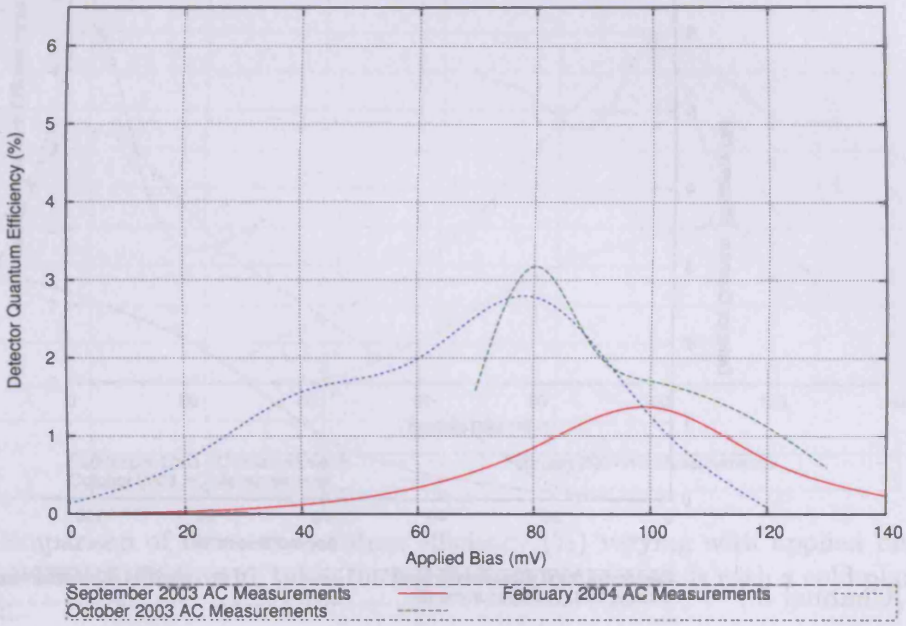

[Channel 3.]

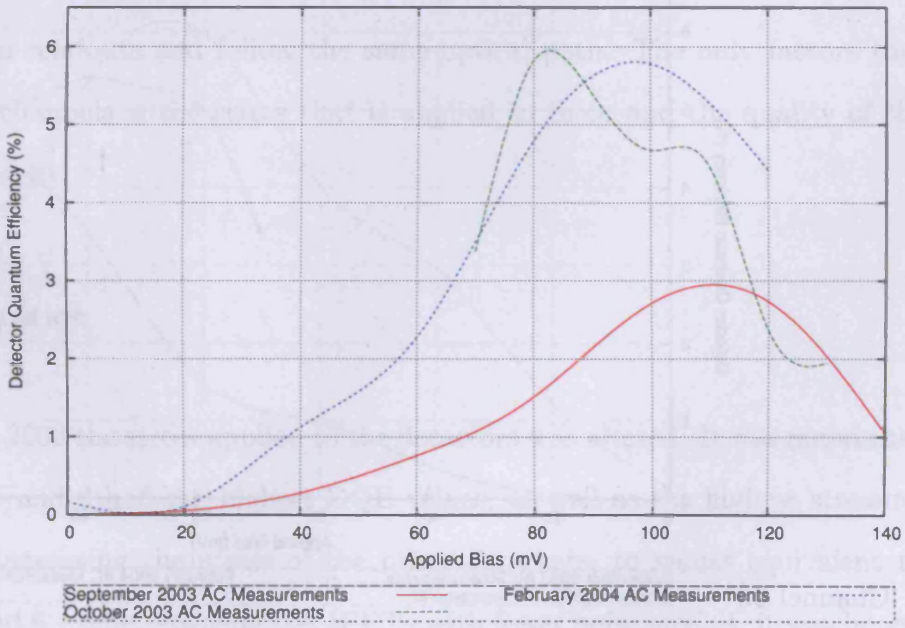

[Channel 4.]

Figure 3.2: Comparison of detector quantum efficiency (%) varying with applied bias (mV) for channels three and four. Data were taken during three seperate periods with a cold plate of 3.7 K for all.

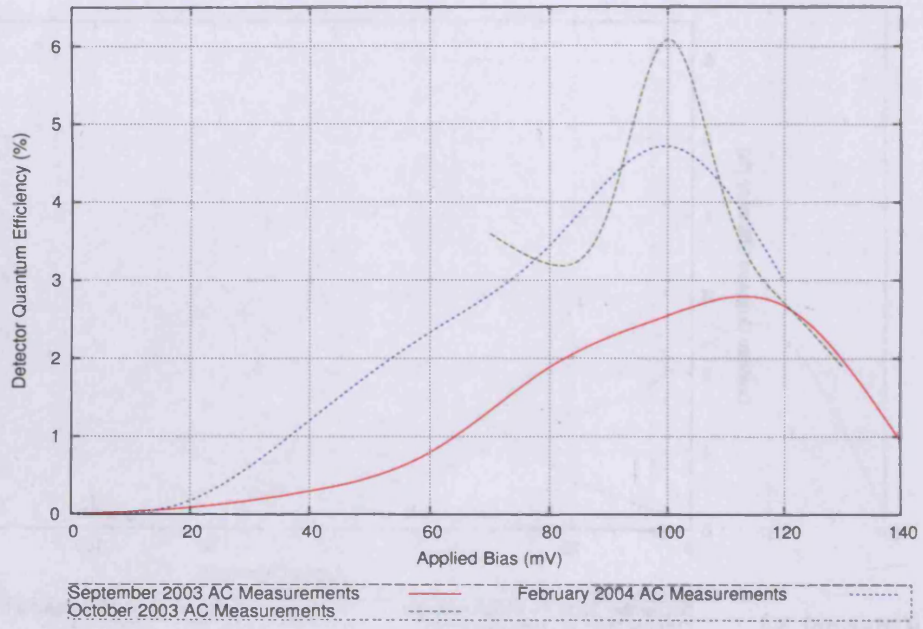

[Channel 5.]

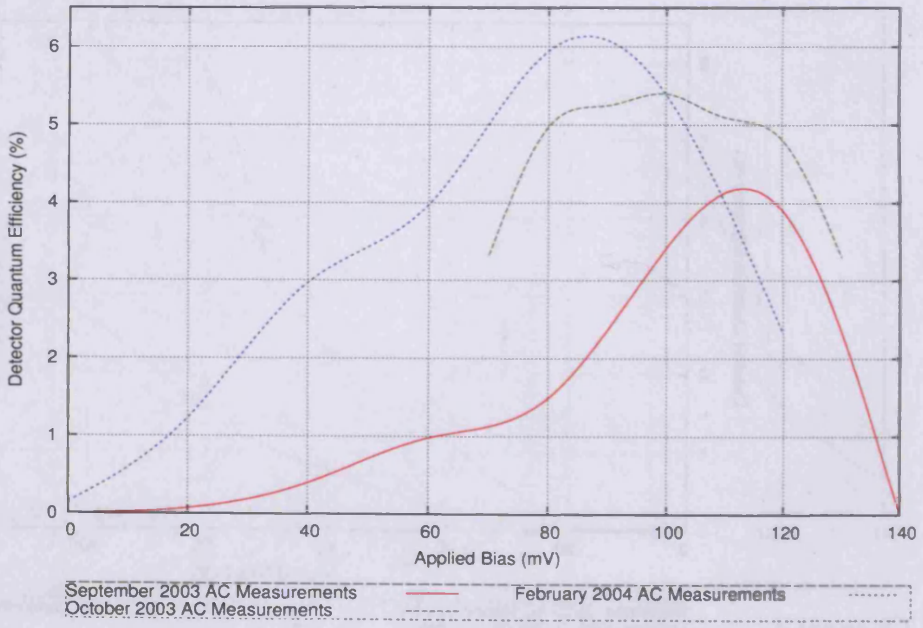

[Channel 6.]

Figure 3.3: Comparison of detector quantum efficiency (%) varying with applied bias (mV) for channels five and six. Data were taken during three seperate periods with a cold plate of 3.7 K for all.

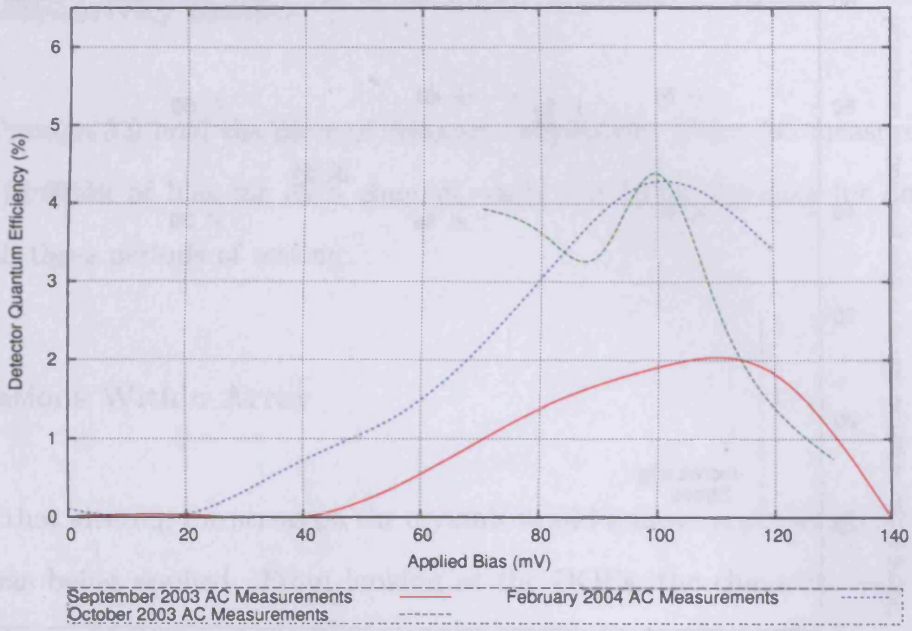

Figure 3.4: Comparison of detector quantum efficiency (%) varying with applied bias (mV) for channel seven. Data were taken during three seperate periods with a cold plate of 3.7 K for all.

have identical readouts and follow the same optical path. The only factors that vary for the channels is the stress that is applied to them and the quality of the integrating cavity.

Stress Alteration

In December 2003 the stress applied to the detectors was altered. It was noted that channels 4, 5 and 6 had the highest DQE values, as well as the highest stressing values. By increasing the stress of the other detectors, to values equivalent to channels 4 and 6, while replacing the JFETs with lower noise models, it was hoped that DQE could be increased beyond the minimum required value of 10%. The change in stress is represented in Figure 3.5.

Values of stress are indicated on the y-axis using the change in room temper-

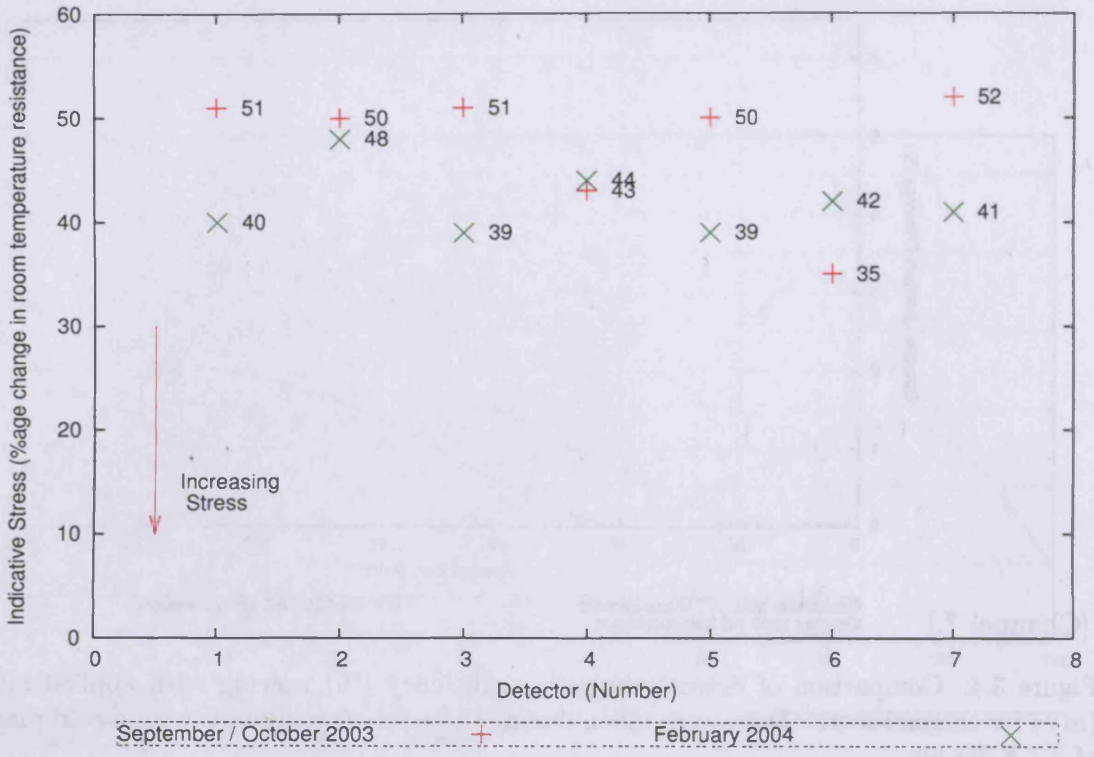

Figure 3.5: Indicative stress for each channel. Before and after stress modification.

ature resistance as a guide. Absolute values of resistance are not used, as other factors, such as the cleanliness of the ohmic connections, affect the resistance that is measured. For channels 1,3,5 and 7, stresses were increased the most. Channel 2 had its stress increased a comparatively small amount, while 4 had its stress reduced and channel 6 had its stress reduced slightly more.

Increasing the stress applied to a photoconductor can be expected to produce an increase in responsivity. This assumes that increasing the physical stress on a photoconductor weakens the bonds that hold the charge carrier to the acceptor atom. The more stress that is applied to a crystal, the more weakened charge carriers are created.

Detector Responsivity Results

Figures 3.6 through 3.9 hold the plots of detector responsivity (from AC measurements) as a function of bias for each channel, each plot holds the data for one channel for all three periods of testing.

Stress Variations Within Array

It was hoped that altering the stress on the crystals would remove any non-uniform stress that was being applied. From looking at the DQEs, the channels can be loosely bound together. Channels 2,4 and 6 all have roughly the same DQE (5.5%), whilst 1 and 3 can grouped together (2.7%) as can 5 and 7 (4.2%).

Channels 2,4 and 6 are all in the same array and have a gradient in stress applied to their array (as indicated by change in room temperature resistance). Channels 1 and 5 are in one outer array and 3 and 7 are in the other. The indications of stress show that 1 and 5 and 7 and 3 have similar stress applied to them. There is no difference in the outer array's stresses. But there is more of a difference in the central block stresses.

However, the central block has the higher uniformity of DQE values, while the outer two arrays have larger variations in DQEs. This suggests that either: not all of the stress that is being applied is acting on the whole crystal, which effectively reduces the size of the photoconductor, or something other than the stressing level is responsible for the variation in DQE.

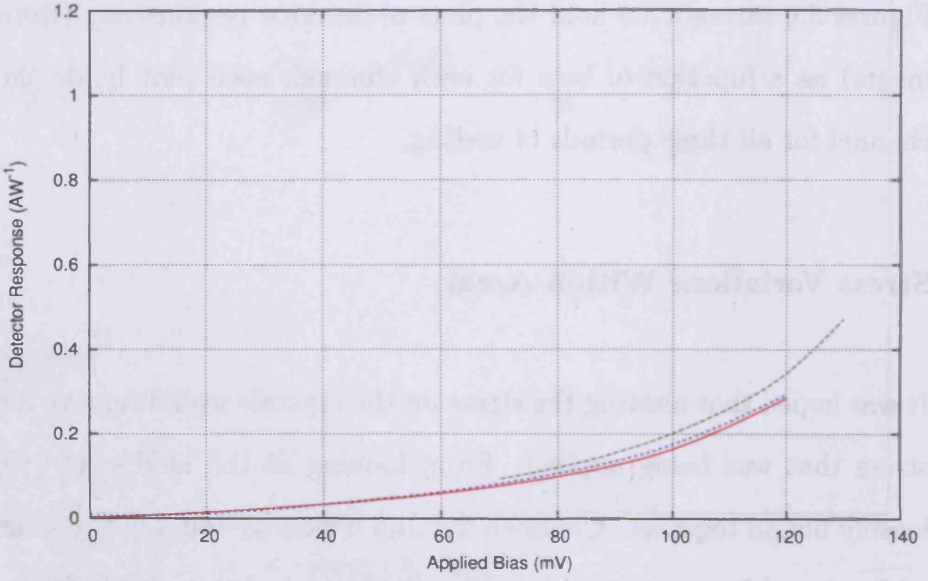

[Channel 1.]

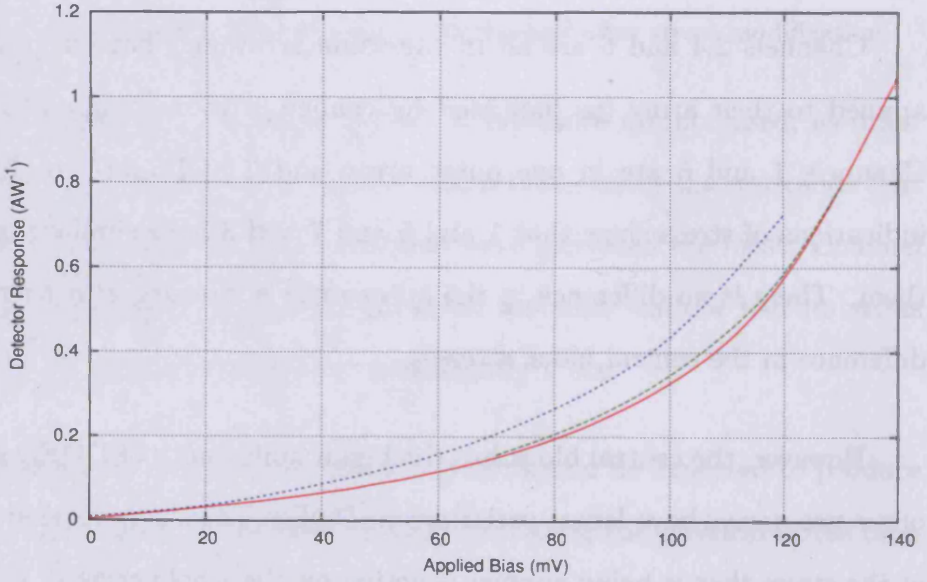

[Channel 2.]

Figure 3.6: Comparison of detector responsivity (AW^{-1}) varying with applied bias (mV) for channels one and two. Data were taken during three separate periods with a cold plate of 3.7 K for all.

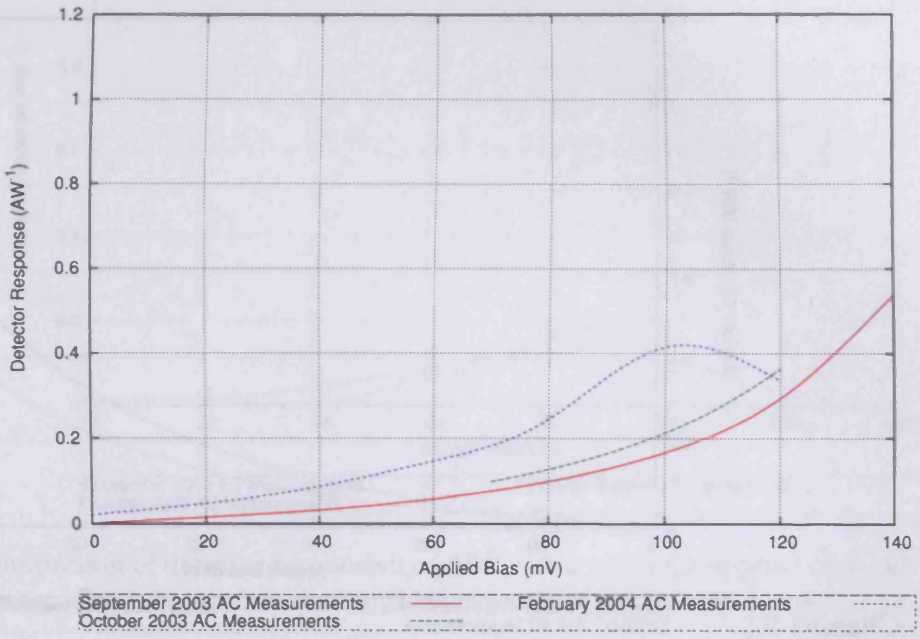

[Channel 3.]

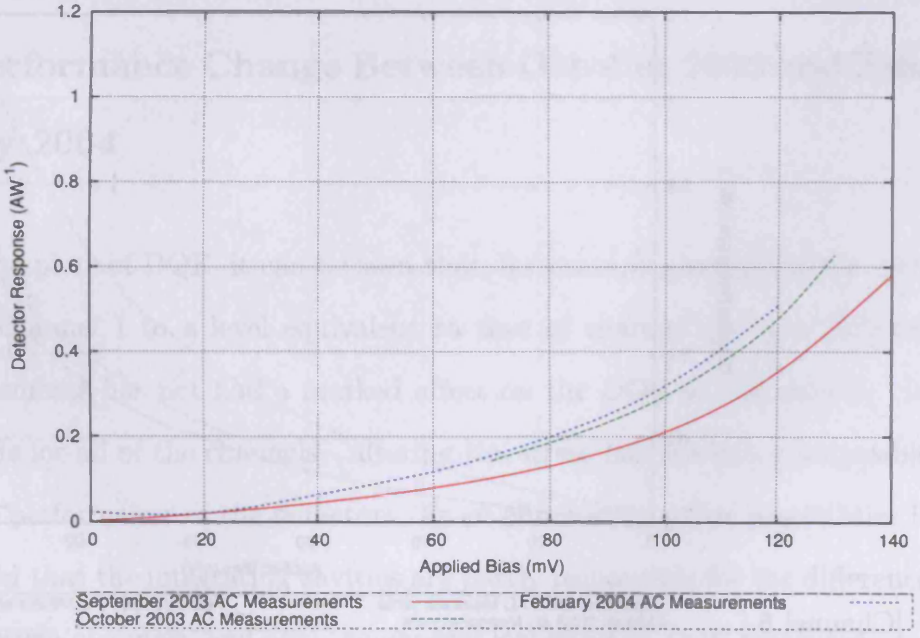

[Channel 4.]

Figure 3.7: Comparison of detector responsivity (AW^{-1}) varying with applied bias (mV) for channels three and four. Data were taken during three separate periods with a cold plate of 3.7 K for all.

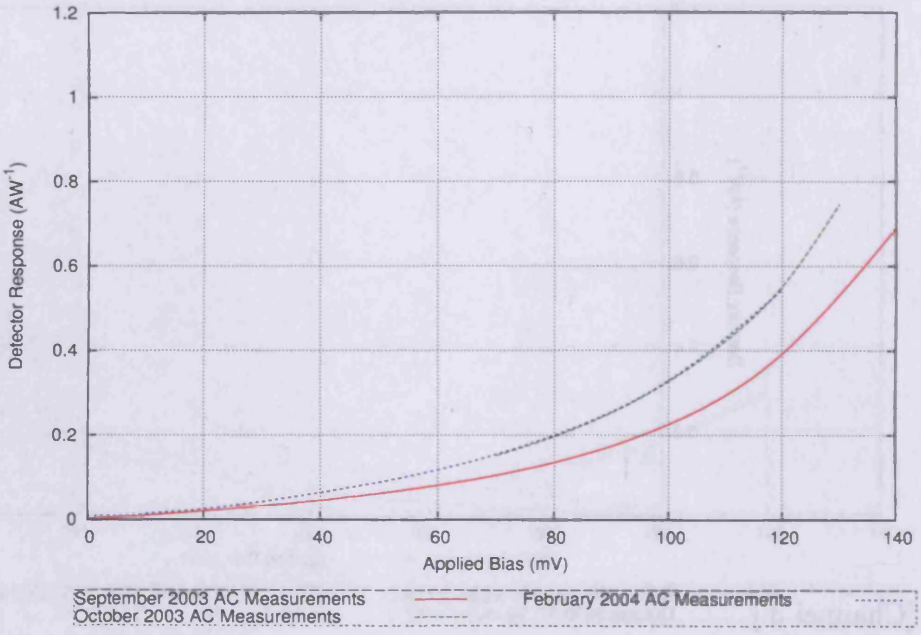

[Channel 5.]

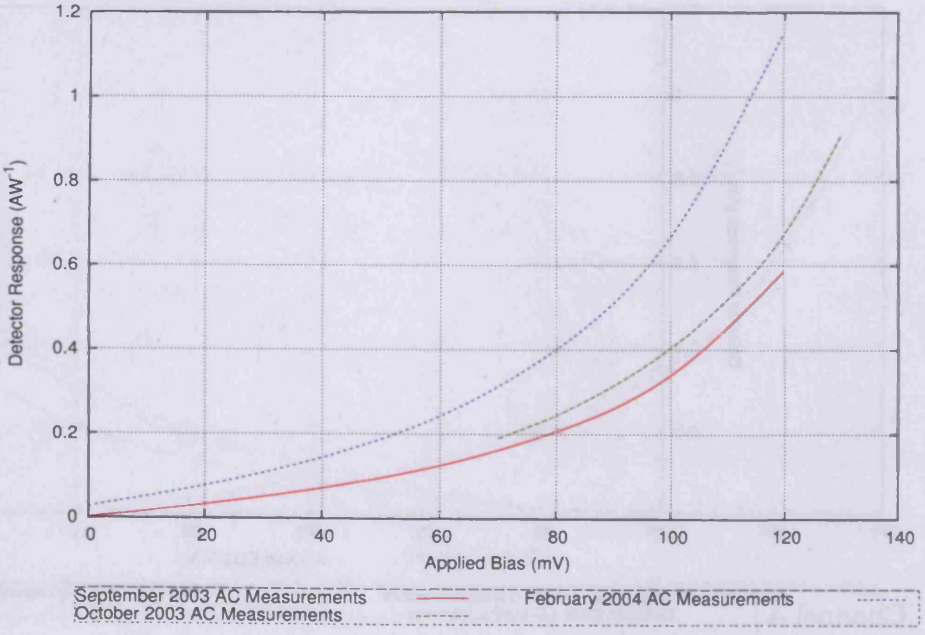

[Channel 6.]

Figure 3.8: Comparison of detector responsivity (AW^{-1}) varying with applied bias (mV) for channels five and six. Data were taken during three separate periods with a cold plate of 3.7 K for all.

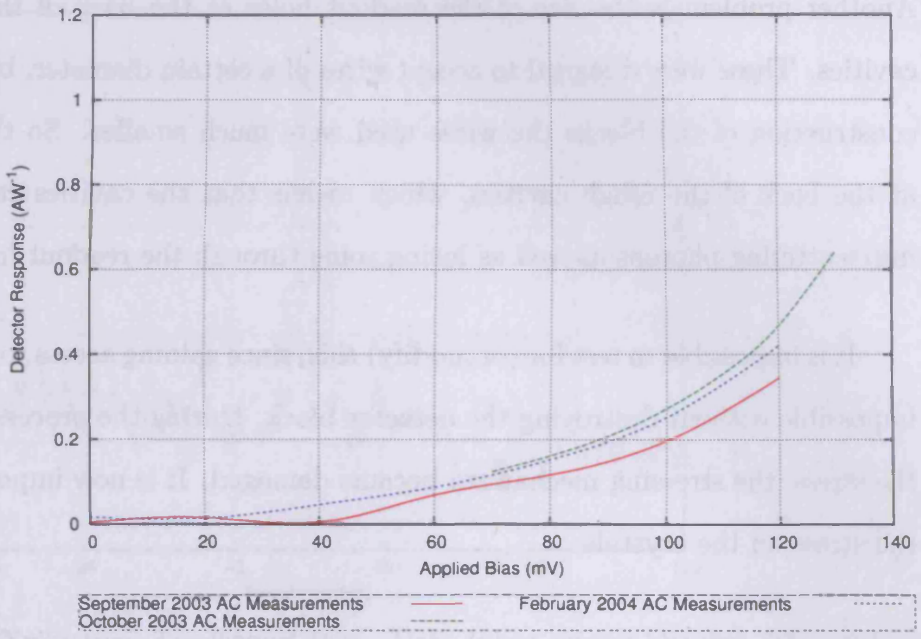

[Channel 7.]

Figure 3.9: Comparison of detector responsivity (AW^{-1}) varying with applied bias (mV) for channel seven. Data were taken during three separate periods with a cold plate of 3.7 K for all.

3.3.3 Performance Change Between October 2003 and February 2004

Looking at the plots of DQE, it can be seen that, for example, increasing the level of stress on channel 1 to a level equivalent to that of channel 4's from October 2003 measurements has not had a marked affect on the DQE or responsivity. In fact this holds for all of the channels - altering the stress has not had a noticeable affect on the performance of the detectors. From eliminating other possibilities it can be implied that the integrating cavities are partly responsible for the difference in DQEs between channels, and also the general low levels of DQE measured.

There are two potential problems with the cavities. The first is the poor finish of the cavities, which has been highlighted by visual inspection. Burrs on the surface and inadequate gold-plating (just like on the Winston cones) are visible.

Another problem is the size of the readout holes at the back of the integrating cavities. These were designed to accept wires of a certain diameter, but during the construction of the blocks the wires used were much smaller. So there are gaps at the back of the rough cavities, which means that the cavities can be absorbing/scattering photons as well as losing some through the readout holes.

It is impossible to test for (or modify) this, since gaining access to the cavities is impossible without destroying the detector block. During the process of increasing the stress, the stressing mechanism became damaged. It is now impossible to alter the stress on the crystals.

3.3.4 Mis-measured DQEs

During this investigation I realised that the October 2003 measurements contained mistakes in estimates of the noise levels that led to misleading values of DQE being derived.

To illustrate this I shall now focus on channel 4. Measuring the signal is fairly straight forward and easy to measure correctly. But when measuring the noise it is more difficult to get it right. Figure 3.10 shows a plot of a noise trace for channel 4 taken from October 2003 with an applied bias of 90 mV, cold-plate temperature of 3.7 K and a heater voltage of 1.001 V.

To approximate the noise at 8 Hz a reading is made from the display of the LABVIEW® software. This is similar to the plot in Figure 3.10. After October 2003 a simple Visual Basic Routine® was written to take the text files that are generated by the LABVIEW® software, plot all channels and approximate the noise around 8 Hz and 80 Hz.

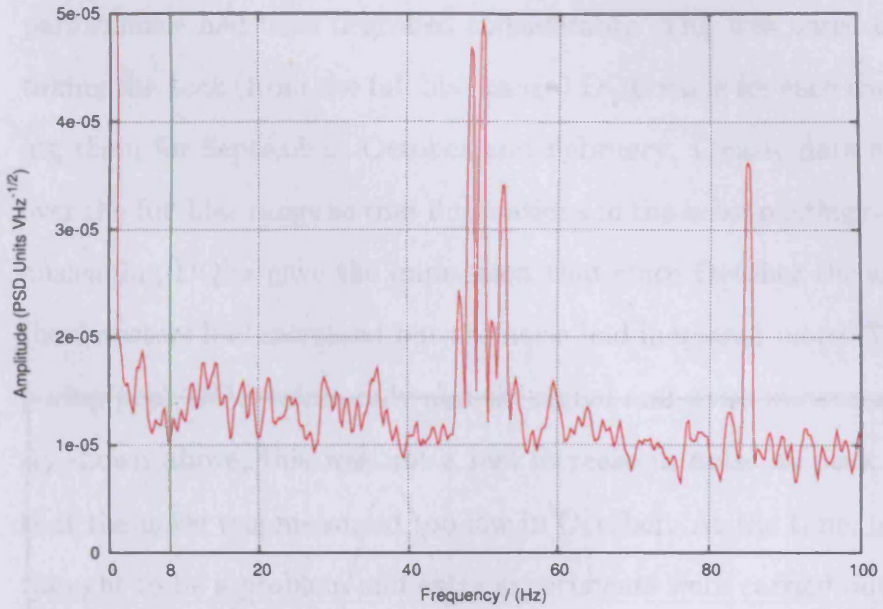

Figure 3.10: Noise trace for channel four. Data taken during October 2003 with an applied bias of 90 mV and a cold plate of 3.7 K.

Figure 3.10 demonstrates an interesting point. Both human eye readings and mathematical averaging gave a value of $1.2 \times 10^{-5} VHz^{-1/2}$. This leads to a DQE of 7.5%, and Channel 4 was quoted as the best channel. Looking at the DQE plot in 3.11 as a function of bias, one can see fluctuations in October's values, but not in September's or February's. The noise reading is taken from a trough, and it is unclear if this sudden drop is real or just a blip. The fluctuations that can be seen in Octobers DQE values as a function of bias for channel 4 compared with the smooth increase in noise that is seen for September or October, leads to the conclusion that the fluctuations are not real.

If this is the case, and the noise is re-read at a mid-point, it can be approximated as $1.4 \times 10^{-5} VHz^{-1/2}$ which gives a DQE of 5.5%. If the DQE graph is re-plotted with these values adjusted, it can be seen that for channel 4 there has been no real change in DQE value between October 2003 and February 2004 as shown in Figure 3.2b. This is in contrast to earlier suggestions that channel 4s

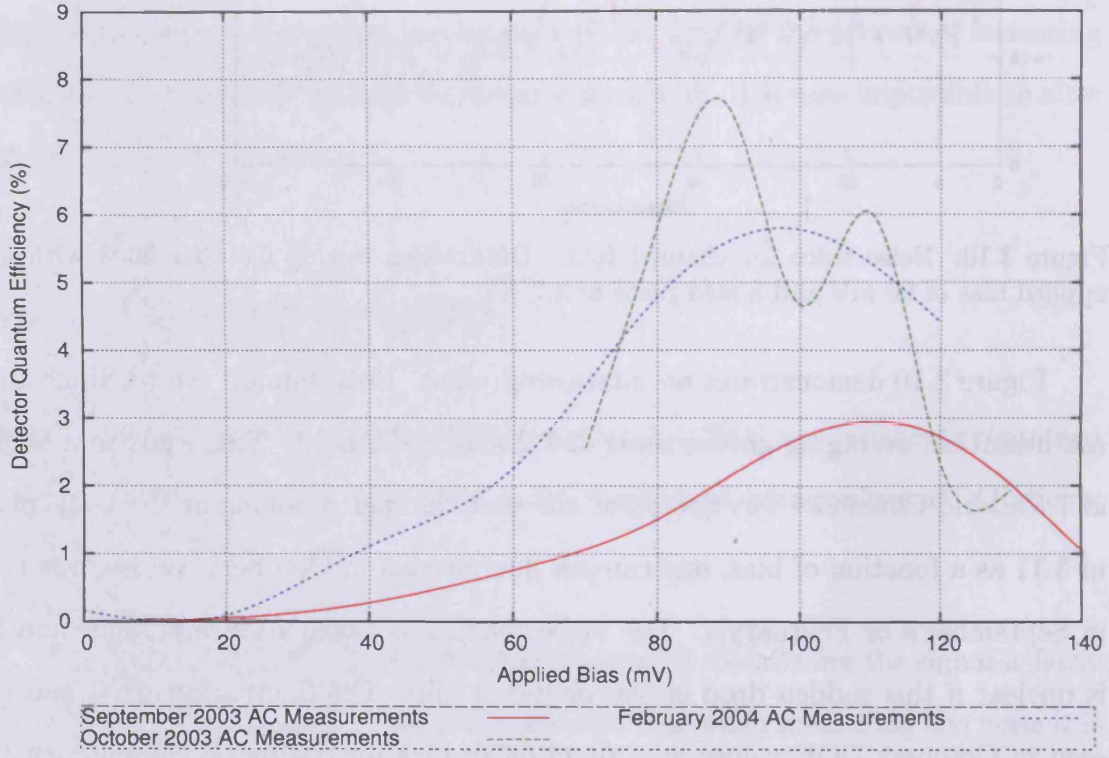

Figure 3.11: Comparison of detector quantum efficiency (%) varying with applied bias (mV) for channel four. Data were taken during three seperate periods with a cold plate of 3.7 K for all.

performance had been degraded considerably. This was based on single readings, taking the *peak* (from the full bias range) DQE value for each channel and comparing them for September, October and February. Clearly data need to be checked over the full bias range so that fluctuations in the noise readings can be seen. These misleading DQEs gave the impression that since October the signal measured by the detectors had increased but the noise had increased more. This was from comparing peak DQE values only and the signal and noise measurements at that bias. As shown above, this was not a real increase in noise at peak bias levels, it was that the noise was measured too low in October. At the time, increased noise was thought to be a problem and extra experiments were carried out to determine this noise source.

3.3.5 Eliminating Sources of Noise

Between October and February the JFETs were replaced with low noise space qualified units (Sudiwala, 2003) that are part of the prototype circuits for PLANCK. These JFETs required a higher operating temperature (100 K) than the previous JFETs. Because of their high sensitivity to temperature, a thermometer was placed on the circuit board. These JFETs are housed in a light-tight box and it was considered possible that light could be leaking from the box, or the heater could be raising the temperature of the detector block.

Photons being emitted from the JFET box and being detected would result in an increase in responsivity. Channel 6 had a marked increase in responsivity, despite having the stress on the crystal reduced. More generally there was no clear connection between measured responses and alterations in stress.

To rule out the effect of the heater on the responsivities, DC measurements were taken at 60 K, 80 K, 90 K, 100 K, and 120 K . For each channel all the VI curves from different temperatures were overlaid. If there was any effect from the JFET heater, it would be expected that the VI traces would vary from temperature to temperature.

From these experiments and the immeasurable differences in the VI traces the JFET heater could be ruled out as a dominant source of noise in the system.

3.3.6 Spectral Response Measurements

To complete the characterisation of the crystals the spectral response of each crystal was measured. These measurements would show what affect altering the stress has had on the crystals. Figure 14 contains the spectral response measurements that were taken during June 2004 and demonstrates that the spectral response of the seven channels are well matched.

Each channel has been self normalised which means that it is impossible to talk of absolute values of the responses. It is possible to compare the response at the frequency that we are interested in with the frequency of maximum response. THUMPER has been designed for use at 200 μm which corresponds to a wavenumber of 50 cm^{-1}. To demonstrate how the detector responds at this wavenumber, Figure 3.13 contains the spectral response measurements of Channel 4 from April 2003 and June 2004.

The comparison between April 2003 and June 2004 allows us to see that for channel 4 the response at $50cm^{-1}$ has increased as a function of maximum since the stress was altered.

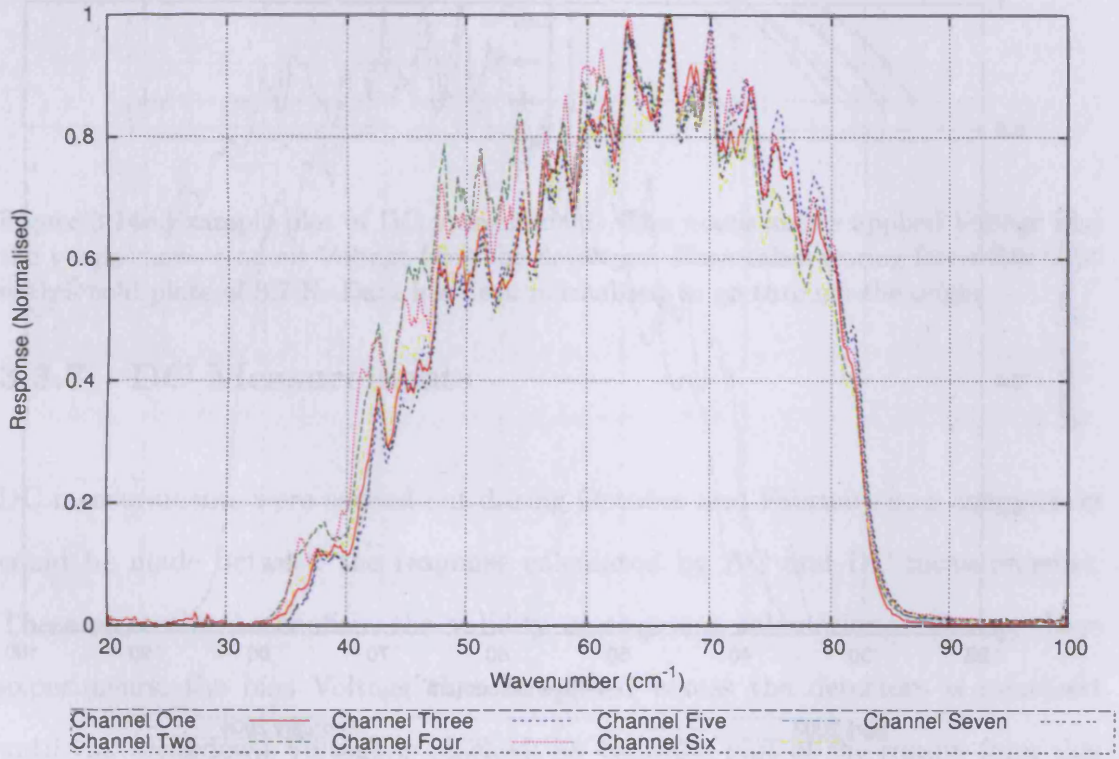

Figure 3.12: Spectral response measurement for all THUMPER's detectors. Data taken during June 2004 with a cold plate of 4.2 K and 90 cm^{-1} low pass edge filters on the cryogenic shields only. Each channel has been normalised against itself.

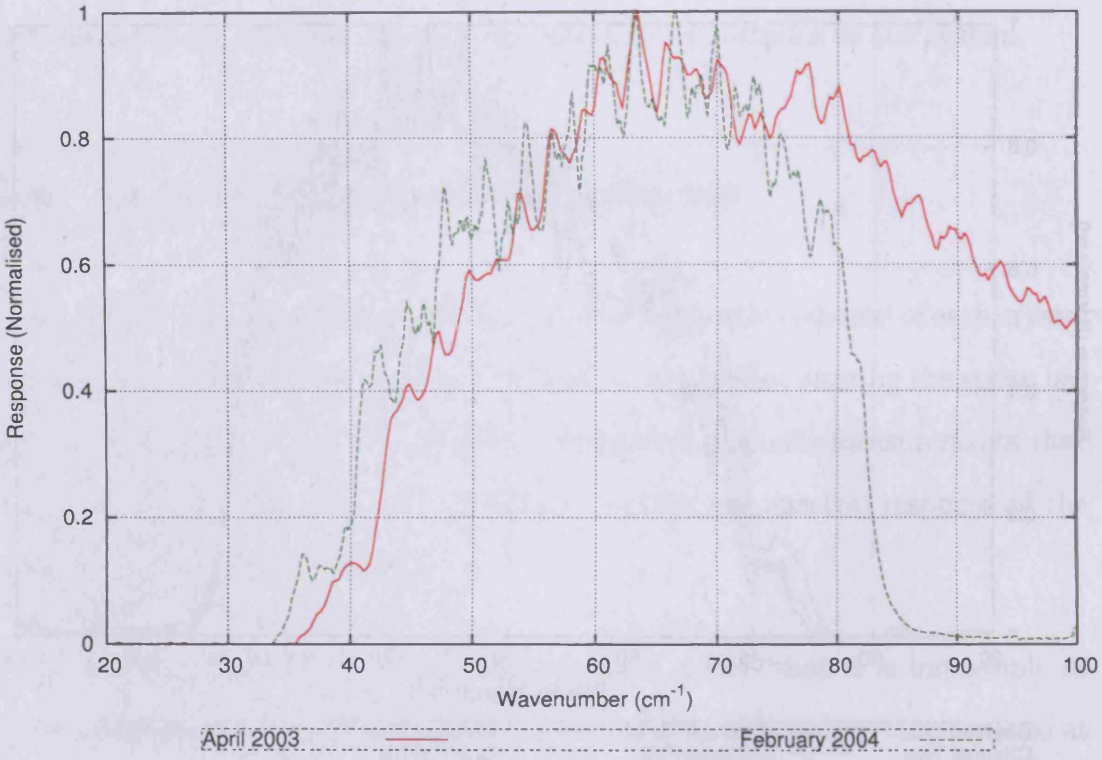

Figure 3.13: Spectral response measurement for channel 4. Data taken during June 2004 with a cold plate of 4.2 K and 90 cm^{-1} low pass edge filters on the cryogenic shields only. April 2003 data taken with a cold plate of 3.7 K and with 150 cm^{-1} filters in place. Both sets of data have been self normalised.

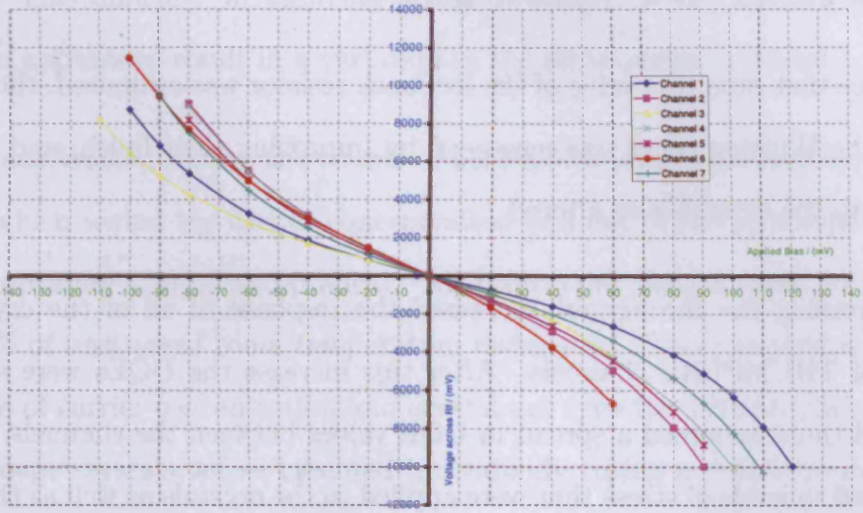

Figure 3.14: Example plot of DC measurement. The x-axis shows applied Voltage and the y-axis shows readout Voltage from the detectors. Data taken during December 2004 with a cold plate of 3.7 K. Data has been normalised to go through the origin.

3.3.7 DC Measurements

DC measurements were carried out during October and February so a comparison could be made between the response calculated by AC and DC measurements. These were able to confirm the validity of response calculations. During these experiments, the bias Voltage that is applied across the detectors is increased until the breakdown Voltage is reached; an example plot of the results from this experiment is in Figure 3.14.

3.4 Conclusions

In September 2003 the DQE was the last of THUMPER's design requirements still to be fulfilled and it was the purpose of these experiments to measure this parameter and monitor the effect that alterations of the detector block had, in an

effort to meet the target of a DQE of 10%.

Since that time: the value of the feedback resistor was optimised, the throughput of the Winston cones was increased by improving their finish, and the stress applied to the crystals was altered.

Increasing the throughput increased the response of all of the crystals and DQEs of THUMPER's channels. After this increase the DQEs were still below 10% and there remained a spread in DQE values between the channels. This was attributed to levels of stress that were applied to the crystals as well as the method of application.

The stress was altered so that the stress was more uniformly applied to the arrays and the levels were generally higher. After this alteration there was no increase in DQE, and no big differences in the spectral response of the crystals.

From eliminating other possibilities it is now understood that the overly large size of the readout holes in the integrating cavities, their poor gold plating and the non-uniform application of stress to the arrays and crystals all contribute to the low DQE.

3.4.1 Non uniform stress

The seven crystals are mounted in the detector block in two $\times 2$ arrays and one $\times 3$ array. The stress is applied vertically through the array and is monitored by the change in room temperature resistance. The channels that had higher DQEs also had higher levels of stress applied to their crystals. This was most pronounced in the central array where it was difficult to apply the stress uniformly to the

crystals. This difficulty in applying stress uniformly to the crystals within an array also appears to result in a variation in the stress across a crystal.

Richard Walker, during the course of his PhD, worked with prototype Ge:Ga crystals which varied the carrier concentration and cut of the prototype crystals' ends (to optimise photon acceptance). All prototypes were stressed to the same level (40% of unstressed room temperature resistance). These experiments led to the choice of carrier concentration and crystal cut type for THUMPER's crystals. The protoype crystals where mounted individually (using a different mechanism) and stressed to levels less than those applied to THUMPER's detectors. Increasing the stress increases the cutoff wavelength of the crystal and it is possible to approximate variations in stress across the crystal by considering te results of the spectral response measurement. Variations in stress will result in variations in wavelength response, such that the greater the variation in stress across the crystal the less steep is the gradient at the longwavelength cut on.

To visualise this, the spectral response measurements from a prototype crystal are superimposed on results from channel 4 from April 2003 and June 2004 as seen in Figure 3.4.1.

It can be seen that the prototype crystal has a narrower wavelength response than channel 4 and this can be attributed to the differences in stressing single crystals and arrays, and the stressing block differences.

3.4.2 Integrating Cavities

The feed-through holes at the rear of the integrating cavities were originally designed with larger electronic readout components in mind. During the process of

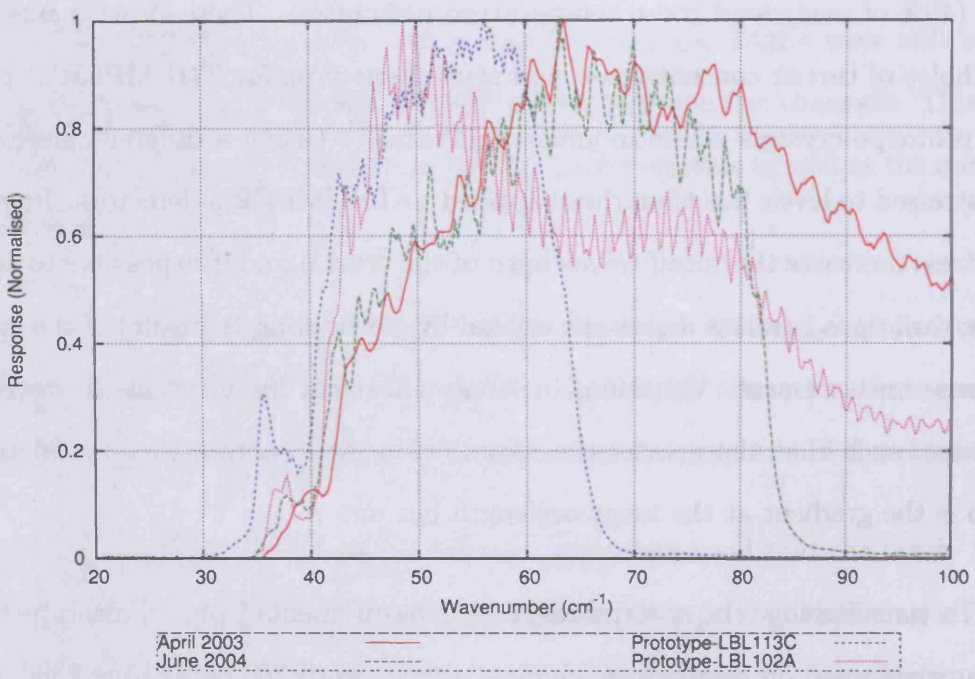

Figure 3.15: Spectral response measurements comparing recent results for channel four with prototype crystals. Data taken during June 2004 with a cold plate of 4.2 K and 90 cm^{-1} low pass edge filters on the cryogenic shields only. April 2003 data taken with a cold plate of 3.7 K and with 150 cm^{-1} filters in place. Prototype data taken by Richard Walker late 2002. LBL113 data were taken at 3.7 K with 70 cm^{-1} low pass edge filters and LBL102 data were taken with 150 cm^{-1} filters. All data are normalised against themselves

manufacture the size of these components was significantly decreased and it is now thought that the excess of hole size is partly responsible for a loss of responsivity.

3.4.3 Summary

During the process of stressing the crystals, the stressing mechanism broke. This means that it is impossible to either alter the stress or plug the feed-through holes at the back of the integrating cavities without rebuilding the detector block. THUMPER is therefore fixed in its current state.

Chapter 4

Commissioning of THUMPER on the JCMT

4.1 Overview of Events

THUMPER was commissioned on the JCMT between February and April 2005: the sequence of events is as follows.

Between 27/02/2005 and 11/03/2005 THUMPER was re-assembled after arriving at the JCMT. Assessment of the performance of THUMPER was carried out during this period to ensure that everything was behaving as it was before THUMPER was shipped. This period shall not be detailed here, as the procedure is identical to that as performed in the lab.

Transferring THUMPER to the right Nasmyth (the other Nasmyth to SCUBA) and the alignment of THUMPER with the JCMT beam took place between 14/03/2005

and 16/03/2005. Testing of the interface between THUMPER and the SCUBA DAQ was between 17/03/2005 and 18/03/2005.

We were awarded a total of eight nights of Director Discretionary Time on the JCMT which were split between two observing runs.

The first observing run began on 20/03/2005 and lasted four nights. During this run the weather was too poor for THUMPER to observe and the time was spent performing further system checks and initial sky dips.

The second observing run was between 06/04/2005 and 09/04/2005 and three of these four nights were suitable for observing. As observations were being made it became apparent that there was a problem in the signal chain. This was noticed when the periods of good weather, which had been predicted to yield positive observational results from THUMPER were not; because of this it was decided to stop using the SCUBA DAQ and operate THUMPER in stand alone mode for the rest of the observing run.

4.2 Setup of THUMPER with JCMT

It was originally intended for THUMPER to be situated on the same Nasmyth as SCUBA, and for a dichroic to be used to reflect 200 μm radiation to THUMPER and transmit wavelengths greater than this to SCUBA. However, THUMPER was being operated singularly in a one off experiment, positioning it on the right Nasmyth which was advantageous in some respects, such as simplifying the optical layout and increasing the working space for commissioning and maintaining the instrument.

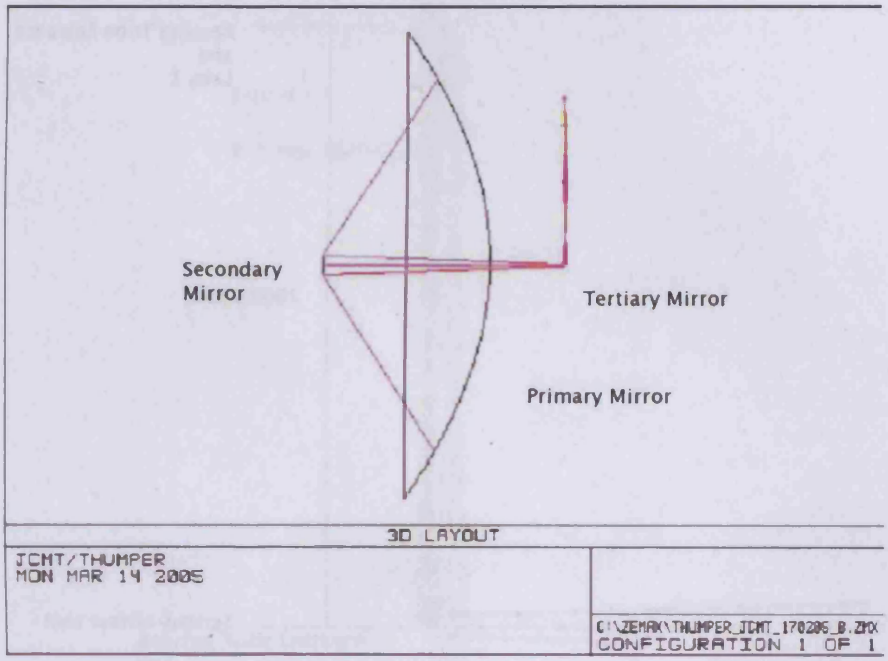

Figure 4.1: Schematic of the JCMT. Dimensions are contained in the text.

4.2.1 Optical Design

The JCMT is a Cassegrain telescope, capable of Nasmyth focusing, and comprising a parabolic primary mirror of 15 m diameter, a hyperbolic secondary of 0.75 m diameter and a flat tertiary mirror to direct the f/12 beam to the desired instrument. A schematic diagram is shown in figure 4.1. The distance between the vertices of the primary and secondary mirror is 5.13391 m.

A fourth year undergraduate project, supervised by Phillip Mauskopf, redesigned the optical system used by THUMPER. Paul Hargreaves, the student who worked on this, came up with a simple solution involving two lenses, manufactured from High Density PolyEthylene (HDPE), positioned either end of the elevation bearing tube.

The Tertiary Mirror Unit (TMU) is a motorised flat mirror that is used to

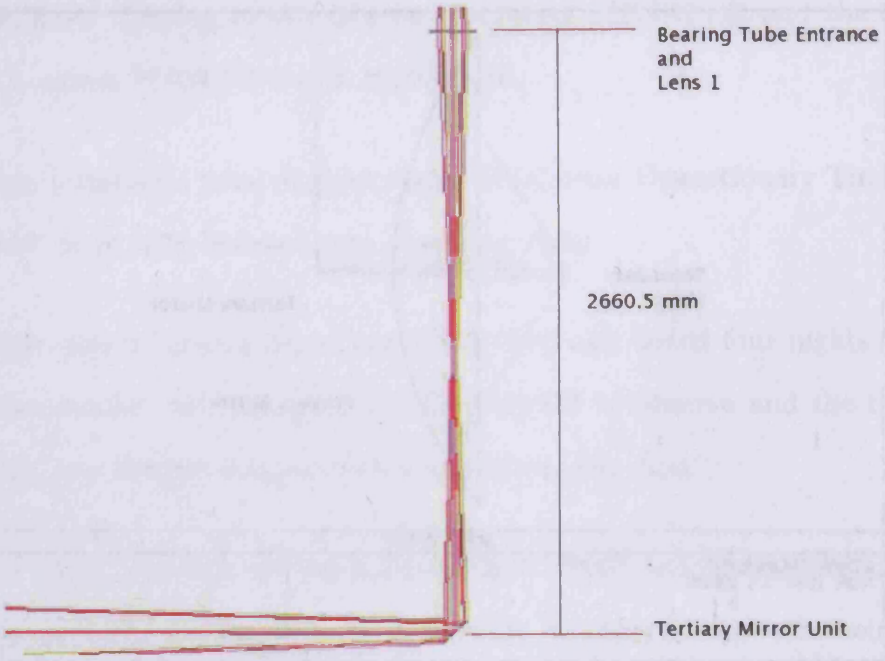

Figure 4.2: Detail of the optical setup at the JCMT. Shown is the TMU reflecting the beam toward the first lens and bearing tube entrance.

direct the beam toward the relevant instrument, either within the receiver cabin or at one of the Nasmyth foci; figure 4.2 shows the TMU reflecting the beam toward the first lens which is positioned just inside the entrance to the elevation bearing tube, (in this figure the entrance to the tube and the lens are indistinguishable). Figure 4.6 shows a photograph of the lens inside the tube.

The beam passes through the bearing tube and a second lens which is mounted on the optical bench (Figure 4.3).

After this final lens, the beam enters THUMPER through the cryostat window, is collimated by mirror T5 onto the flat mirror T6 which reflects it onto THUMPER's focal plane array (Figure 4.4). Figure 2.3.2 is a photograph of THUMPER's cold plate which shows the mechanical components which relate to this optical diagram.

Figure 4.3: Detail of the optical setup at the JCMT. Shown is the entrance and the exit of the bearing tube and both the lenses. The length of the bearing tube is 182.5 cm. Lens 2 is 16.5 cm from the exit of the bearing tube.

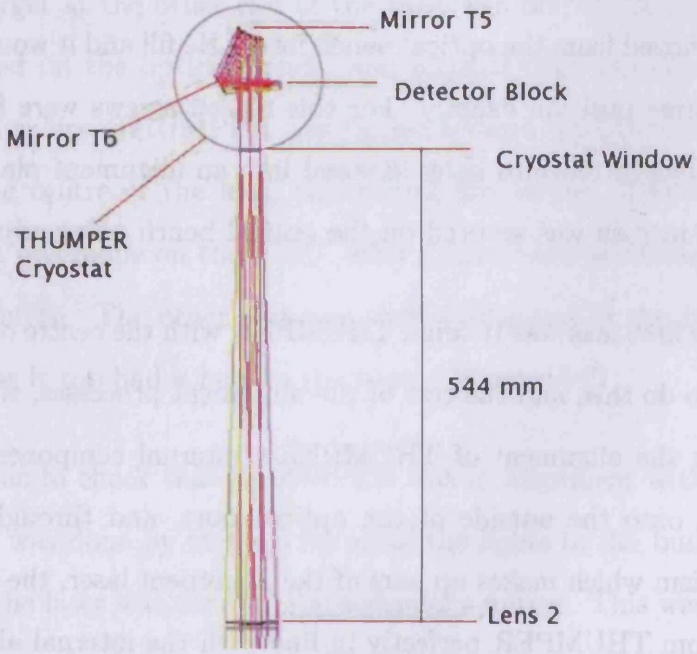

Figure 4.4: Detail of the optical setup at the JCMT. Shown is exit of the bearing tube, the second lens and THUMPER's optical components.

4.3 Installation of THUMPER on JCMT

THUMPER was integrated with the JCMT during the week beginning 14/03/2005. The first three days were taken up with the optical alignment, and the next two days were used to link THUMPER with the SCUBA DAQ; THUMPER was then ready for it's first night of observation on 20/03/2005.

4.3.1 Alignment of THUMPER with JCMT beam

For THUMPER to be coupled to the JCMT, to enable it to observe using the telescope, it needed to be aligned with the JCMT beam. This was a relatively straight forward procedure achieved using a laser alignment system.

The observing run was separated into two four night periods with a fortnight gap, and this long time between observations meant that THUMPER would need to be removed from the optical bench for a LHe fill and it would need to be returned to the same position exactly. For this reason screws were fitted to the lid of the OVC, which fitted into holes screwed into an alignment plate (Figure 4.5), whose position in turn was secured on the optical bench using adjustable markers.

The first task was to align THUMPER with the centre of the elevation bearing tube. To do this, and the rest of the alignment processes, the same laser that was used for the alignment of THUMPER's internal components was used. This is screwed onto the outside of the optical port, and through the use of a mirror mechanism which makes up part of the alignment laser, the laser is able to project away from THUMPER perfectly in line with the internal alignment.

THUMPER was positioned on the optical bench, but not secured down, so

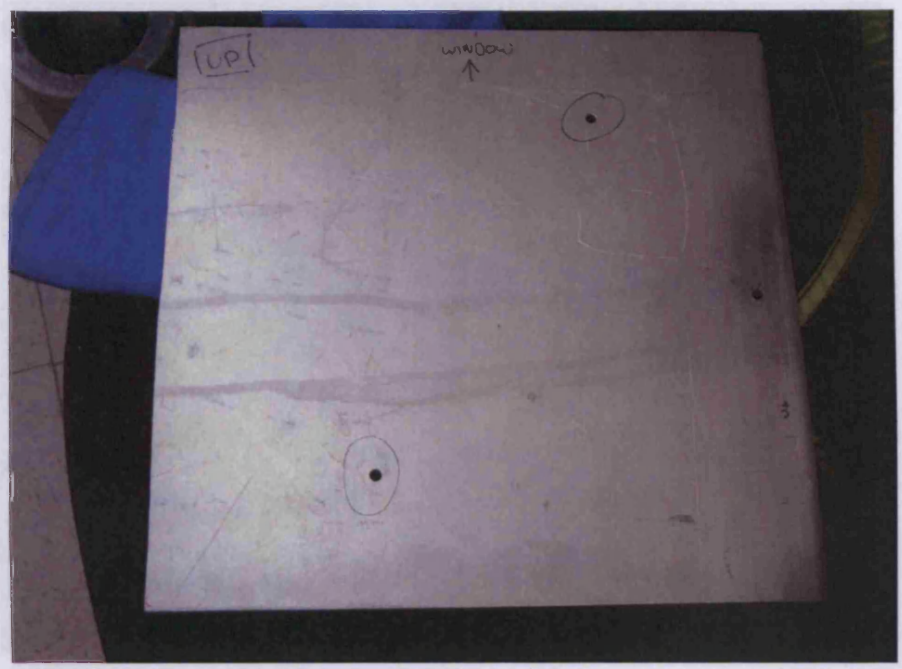

Figure 4.5: The spacer plate that was used to locate THUMPER on the optical bench.

that it could still be freely moved around. At the end of the bearing tube closest to the TMU, a crosshair was made using string and tape, to form a target for the laser. Acting as a target at the other end of the tube was one of the lenses, Lens 2, which was mounted on the optical bench, and aligned with the centre of the tube using string and rulers. THUMPER was jiggled around until the laser passed through a hole in the centre of the lens, and struck the string. The string was removed, and a mark was made on the TMU, after it had been positioned to pass radiation to the Nasmyth. The other lens was then positioned in the tube using the laser as a guide as it too had a hole in the centre (Figure 4.6).

The final task was to check that THUMPER was in alignment with the secondary mirror which was done by turning off all of the lights in the building and checking to see that the laser was striking the secondary mirror. This was successful and a final alignment check was performed to see how it was affected by tilting the dish. This was performed by turning on the laser attached to THUMPER,

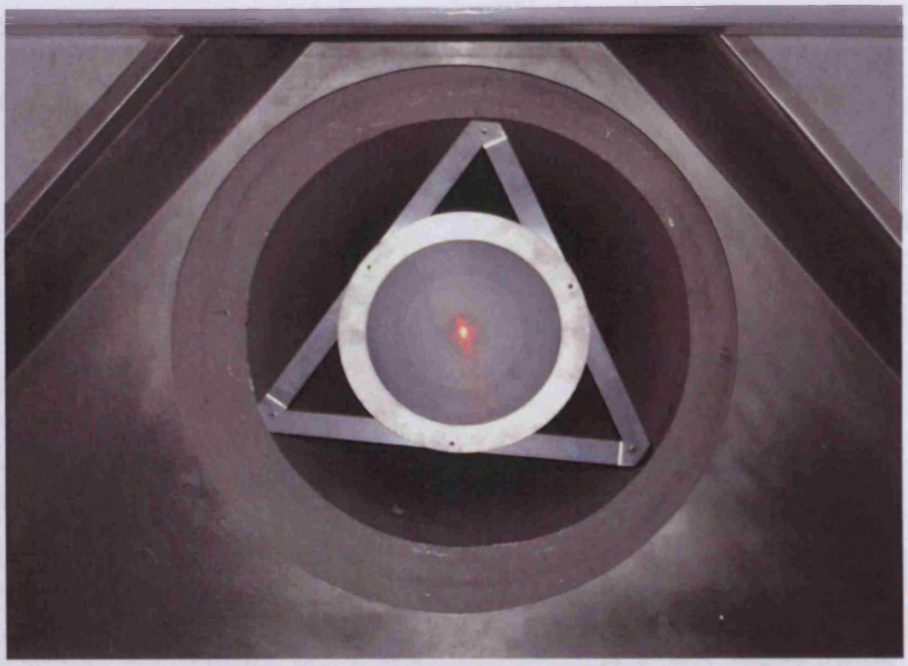

Figure 4.6: Lens in the receiver cabin of the JCMT with laser passing through alignment hole.

checking that it was still striking the TMU in the same place, and then tilting the dish while two people stayed in the receiver cabin to observe if the laser still struck the TMU in the same place, which it did. Figure 4.7 shows THUMPER on the optical bench after successful alignment; visible is the spacer plate, which is underneath THUMPER and secured to the optical bench, the chopper wheel and the second lens which was positioned just behind the exit of the Nasmyth bearing tube.

4.3.2 THUMPER Integration with SCUBA DAQ

After the successful alignment of THUMPER with the JCMT beam the final stage of installing THUMPER on the JCMT was integrating with SCUBA's DAQ system. Although THUMPER was not to be used at the same time as SCUBA, as intended in the original design, it was decided that THUMPER would still use

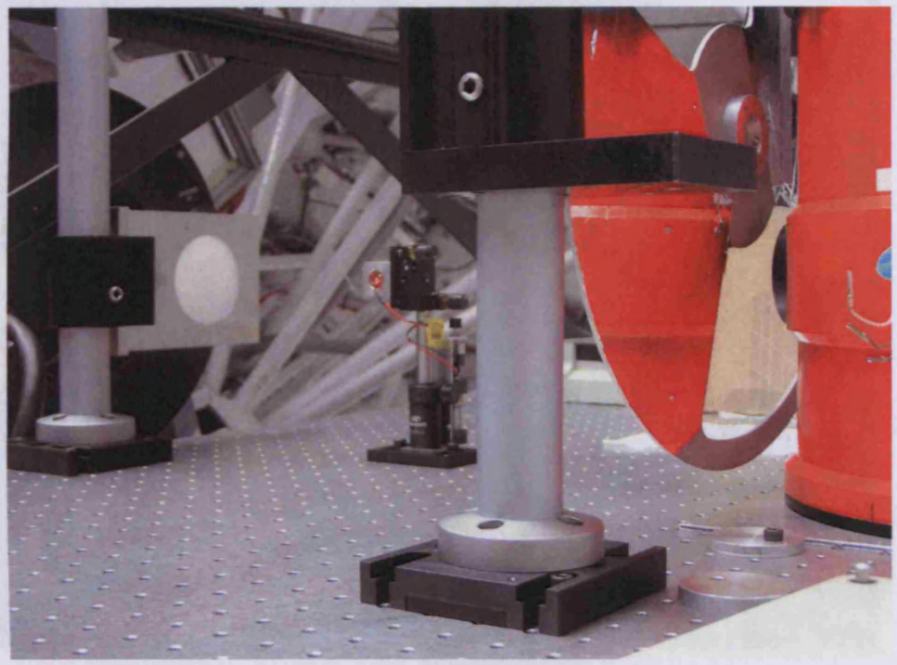

Figure 4.7: THUMPER secured to the optical bench after optical alignment.

SCUBA's DAQ system so that the data reduction software that was in place for SCUBA could be used by THUMPER.

Because SCUBA's DAQ is located next to SCUBA, on the opposite Nasmyth to THUMPER, a cable was needed to run from THUMPER's readout box around the stationary parts of the telescope across to the other Nasmyth, a distance of ~20 m. THUMPER did not directly connect into the DAQ, an isolator box was used to provide electrical isolation between THUMPER and SCUBA and is shown in Figure 4.8.

The isolator box needed to be powered separately, introducing another check, and possible error, point for THUMPER's operation, which should be noted. Although the initial testing of the entire DAQ chain was successful, later problems were attributed to this isolator box.

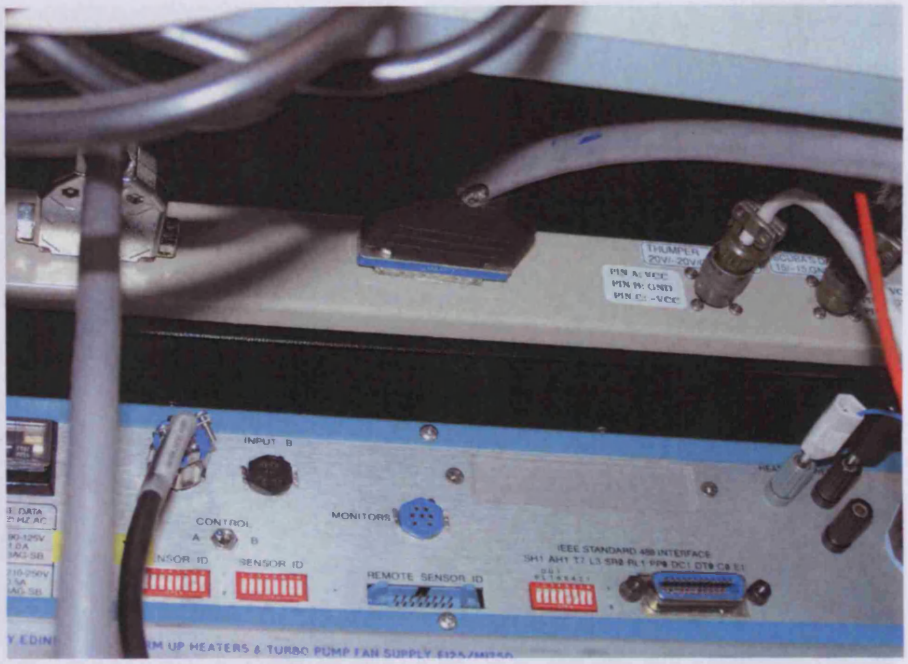

Figure 4.8: Isolator Box.

Initial Integration

THUMPER was connected to the isolator box which bridges THUMPER and the DAQ system, and this enabled THUMPER's signals to be read using the data analysis software, SURF (Jenness and Lightfoot, 2003). SURF is a set of tasks necessary for reducing demodulated SCUBA data obtained from the James Clerk Maxwell Telescope. It was intended for THUMPER to use this software for it's data reduction. A known signal was then passed through the signal chain, and for this purpose an illuminator, or reverse bolometer, had been positioned on THUMPER's coldplate. This was powered up to flash a sine wave illumination of 8 Hz at the detectors.

Once the signal had passed through the DAQ chain it was stored in a data file as raw voltages and it was easy to display the output for each channel on screen. Even though the illuminator signal was a sine wave, it couldn't be expected to

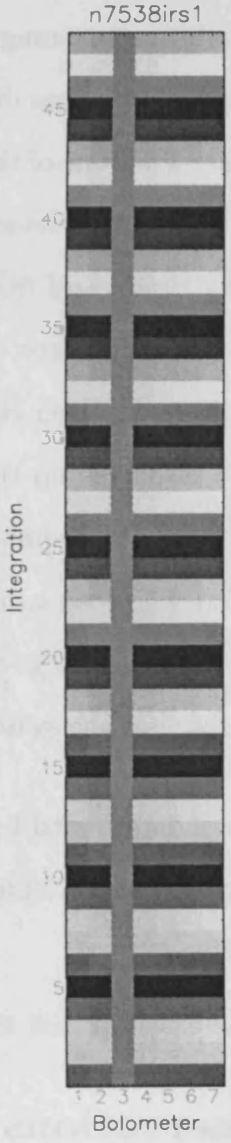

Figure 4.9: Display output from SURF demonstrating a working DAQ system. All seven channels are plotted against integration time. Channel 3 has 1000 times lower gain to test the system. Grey scale is the same extinction corrected Volts as Figures 4.10 and 4.11.

simply see a sine wave on the display as the DAQ system acts like a lock in amplifier and the sine wave is constructively interfered with the reference wave.

These initial tests of the signal chain that were performed were quite simple, though unfortunately, non quantitative, meaning that it was known that the system was working, but once a problem arose it was difficult to say how well the system had been working. Shown in figure 4.9 is one of the plots that was used to determine if the system was working. The x-axis is detector number (1-7), and the y-axis is integration number (effectively time), and from this plot it appears that all the channels are working apart from channel three. This is because channel three had it's gain set to 1000 times less than the other channels as part of the test and it's Voltage levels are too low to be displayed on the scales of this plot. This can be illustrated by looking at figure 4.10, which shows the voltage output from channel three against time; a value of 2.0 mV peak to peak is measured. And comparing this with figure 4.11, a plot showing the voltage output of channel one to be around 2.0 V peak to peak, demonstrates that the system was behaving in a logical way.

At this time THUMPER was determined to have been successfully integrated with the JCMT and was ready for the first night of observing on 20/03/2005; this setup is pictured in Figure 4.12.

4.4 Planetary Observations

The first observing run lasted for four nights and during this run the weather was too poor for THUMPER to observe, so further system checks and initial sky dips were carried out.

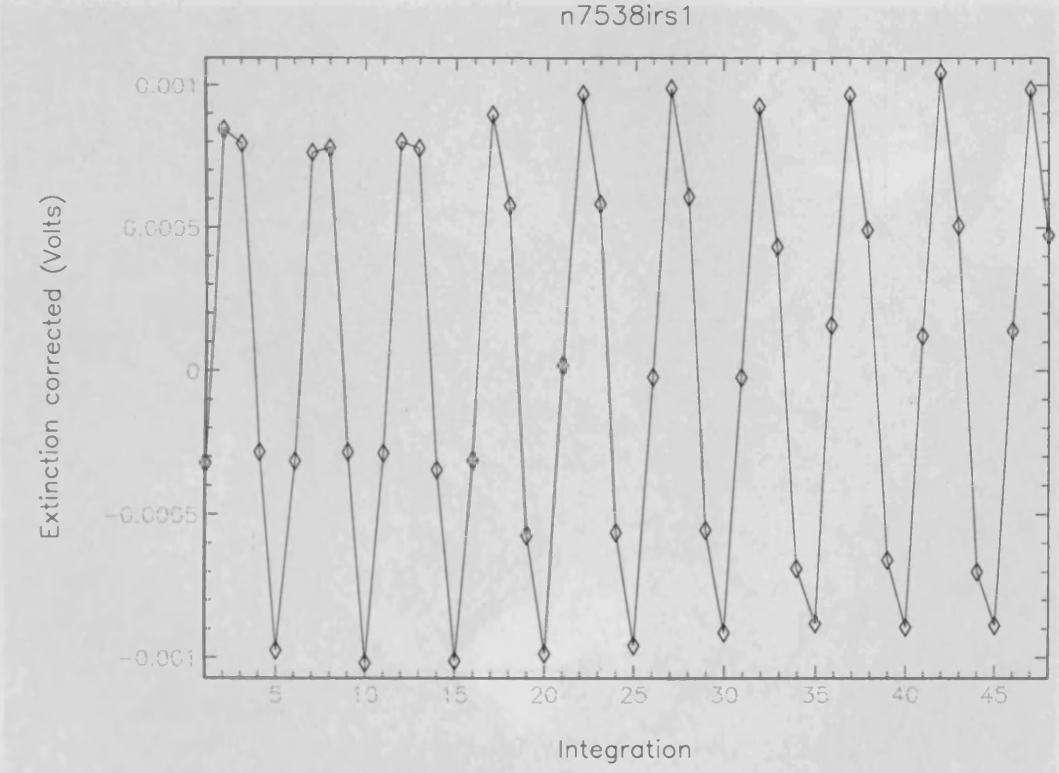

Figure 4.10: Display output from SURF demonstrating the affect of gain on channel 3. Each integration is 5 seconds.

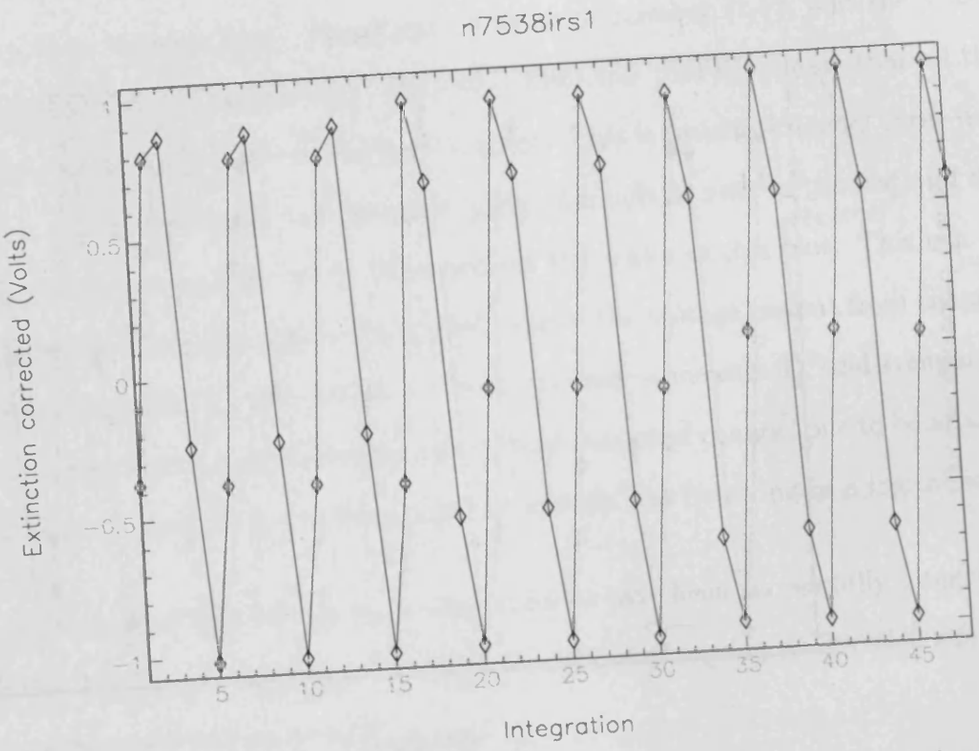

Figure 4.11: Display output from SURF demonstrating the effect of gain on channel 1. Each integration is 5 seconds.

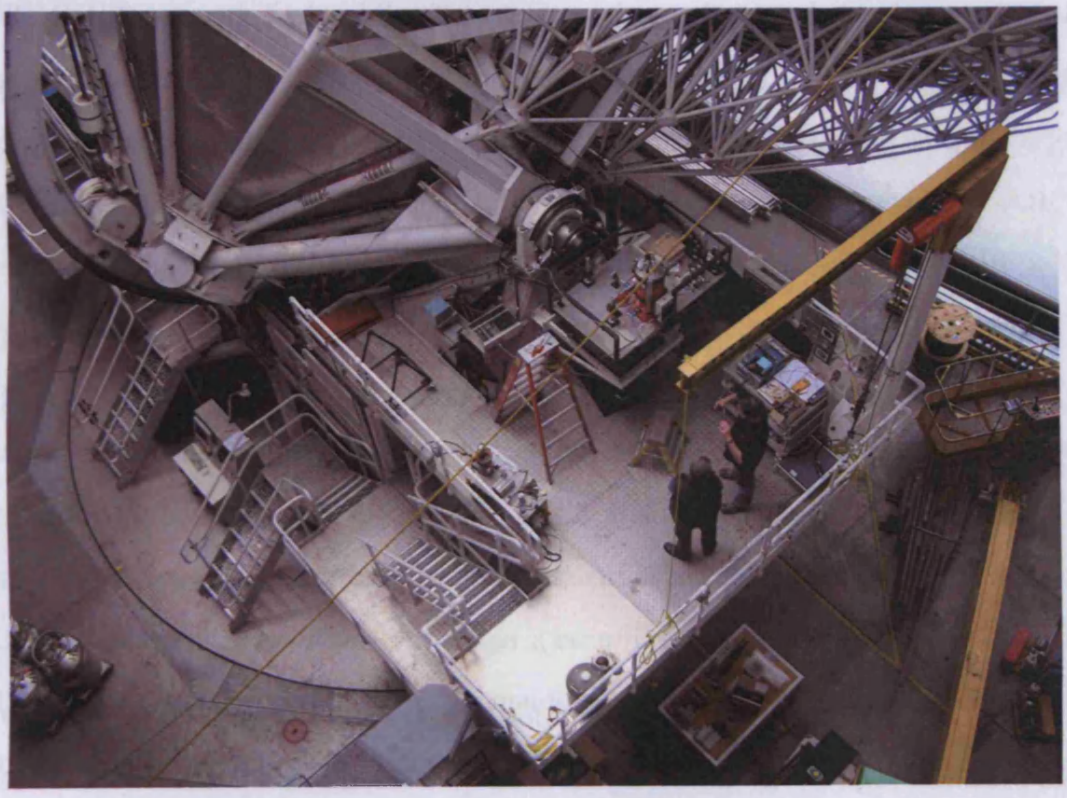

Figure 4.12: THUMPER on JCMT.

The second run was between 06/04/2005 and 09/04/2005 and three of these four nights were potentially suitable for THUMPER to observe. Because these were the first nights observing with THUMPER, the basis for predicting whether conditions were suitable had to be laboratory measurements and modelling of the transmission of 200 μm radiation through the atmosphere.

During the first night of the second run good weather coincided with Jupiter being at a suitable height that a detection was feasible. And, because THUMPER had been powered up for preliminary calibration checks, it was possible to begin observing as soon as these conditions arose. Data were initially analysed using ORAC (Jenness and Economou, 2003) and SURF. The very low voltages (of order 1×10^{-6} V) implied that there was a problem, which could have been somewhere in the signal chain, or, more problematically, with THUMPER's response in theoretically observable conditions. To rule out the former, a signal of around a Volt was formed over the detectors by chopping using a reflective wheel and a black body source. This gave the same negligible result in SURF, so the isolator box was checked again and the gain was increased by a factor of a thousand (to the level that had been used when observing Jupiter), again the result was the same in SURF. It was concluded that there was a problem in the signal chain that would not be readily solved, so THUMPER was operated separately from the SCUBA DAQ. This was done by firstly using the Lock-In amplifier and then by using the LABVIEW procedure. Both these tests showed that THUMPER was working within the laboratory specifications, but was unable to detect a signal from Jupiter. This latter result was not too unexpected as the weather conditions had changed for the worse making a detection of Jupiter impossible.

Mars was due to rise a few hours later in the night, and until then calibration measurements were made, as well as a repetition of the illuminator tests that were

carried out a few days earlier. These tests confirmed that THUMPER was working within laboratory specifications but that there was a problem in the DAQ chain that could not be diagnosed at that time.

Through necessity, and for the rest of the observing run, the Voltage outputs from THUMPER were measured using a combination of the Lock-in amplifier and a LABVIEW program that had been written to evaluate the performance of THUMPER in the laboratory. The advantage of the Lock-in amplifier over the LABVIEW procedure was that it was capable of a much quicker response to a change of Voltage; it's disadvantage was that it was able to take only one channel input and had no capacity for storing or averaging data. The LABVIEW program was capable of storing and averaging the data but the only data it stored was the output from a fast Fourier transform, the raw voltage data were discarded. This has made post observation analysis of these data difficult.

4.5 Skydips

On the occasions when the sky was totally opaque we measured the relative responsivity of the seven channels by measuring the sky emission at zenith. This is essentially a flat, extended source, and allowed us to make a flat-field of our focal plane array. This remained remarkably constant, and was also consistent with our sensitivity measurements made in the laboratory.

During the times when we could carry out astronomical observations we calibrated the sky transmission using the method of sky-dipping. This entails measuring the sky emission at several positions between zenith and horizon, and modelling the profile as a function of zenith distance, z. The emission is predicted to have the

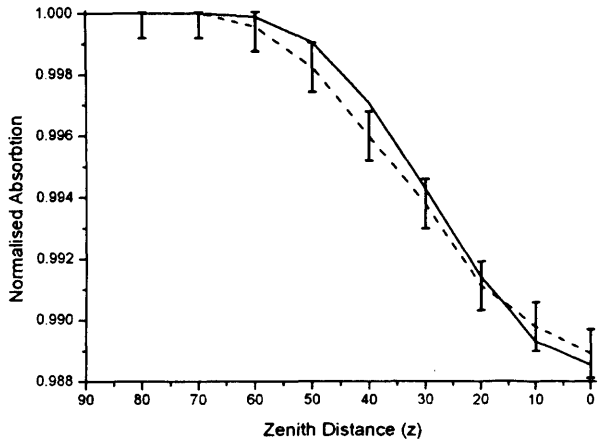

Figure 4.13: Plot of a typical set of sky-dip data. Normalised emission is plotted against zenith distance. The data-points are shown, along with estimated error-bars, joined by a dashed line. The solid line is a fit to the data used to obtain $\tau_{1.5THz}$. See text for details.

form $(1 - e^{-\tau secz})$, and hence a fitting routine can be used to calculate the optical depth, τ.

Figure 4.13 shows the result of a typical sky-dip. On the x-axis is plotted zenith distance z from 90° to 0°, while the y-axis gives the emission measured from the sky at a given value of z, normalised to the peak emission at 90°. The data-points with error-bars are shown connected by a dashed line, while the solid line shows the model fit to the data for an optimised value of the optical depth, τ.

Throughout our observations, the JCMT water vapour monitor (WVM) measured the atmospheric opacity at 183 GHz and from this calculated the opacity at 225 GHz (for historical reasons) in the standard way in which it records these data (e.g. Archibald et al., 2002). The WVM uses a pick off mirror mounted just above and to one side of the tertiary mirror. This means that it is looking along the same line of sight as the primary instrument which is particularly useful in variable weather conditions. It updates its estimate of the 225-GHz opacity every 1.2 seconds. Consequently, at the time of each sky-dip we know the value of the

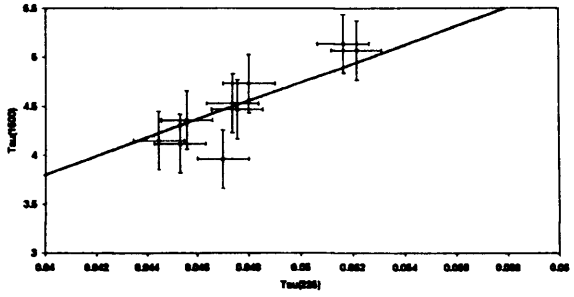

Figure 4.14: Plot of $\tau_{1.5THz}$ versus τ_{225GHz}. The data are shown as crosses. The solid line is a least-squares fit to the data. The best fit straight line that we find is $\tau_{1.5\mathrm{THz}} = (95 \pm 10) \times \tau_{225\mathrm{GHz}}$.

225-GHz opacity, so we can plot it against our measured 1.5-THz opacity.

Figure 4.14 shows the resultant plot of $\tau_{1.5THz}$ versus τ_{225GHz}. The data are shown as crosses. Our sky model calculations (see above) predict a linear relation between these two frequencies over the observed range of values. The solid line is the resulting least-squares fit to the data. The best fit straight line that we find is:

$$\tau_{1.5\mathrm{THz}} = (95 \pm 10) \times \tau_{225\mathrm{GHz}}.$$

This result is consistent with our model predictions and can also be compared with those obtained by previous workers. For example, Matsushita et al. (1999), found a relation of the form $\tau_{1.5\mathrm{THz}} = (105 \pm 32) \times \tau_{225\mathrm{GHz}}$ for the observing site at Pampa la Bola in Chile.

These latter authors used an FTS to measure the atmospheric opacity across the different wavebands, whereas we are comparing our data to WVM data. Nevertheless, recent work shows that provided all relevant effects are taken into consideration, the results from FTS and WVM measurements generally agree well (Pardo et al. 2004). Hence our result is fully consistent with previous work. Therefore we

can use this relation to calibrate our subsequent measurements.

4.6 Planet maps

4.6.1 Jupiter

The first astronomical object we imaged was Jupiter. Figure 4.15 shows our 200-μm map of Jupiter. It was constructed from two consecutive maps of Jupiter, taken immediately one after the other, over the airmass range 1.25 to 1.27. The two maps both show the same structure, and so they were co-added to increase the signal-to-noise ratio. We note that the source is not exactly centred in the image, being misaligned by ~30 arcsec. The telescope absolute pointing accuracy (based on measurements made with other instruments) at this time was $\leq$3 arcsec. This implies that our system alignment was not perfect. This is not surprising given that this was the first time that THUMPER had been mounted on JCMT and this was the first-light astronomical image.

The flux density of Jupiter at this wavelength can be predicted from planetary modelling (Griffin et al., 1986; Orton et al., 1986; Griffin & Orton 1993). Based on this, we expect the peak flux density of Jupiter to be 34 kJy/beam. During the observations the measured value of τ_{225GHz} was 0.0625. Using our relation above, between 1.5THz and 225GHz, this corresponds to a value of $\tau_{1.5THz}$ of ~5.9.

Therefore the observed flux density at the telescope is predicted to be 21 Jy/beam. The total integration time per point of the two co-added maps was 100 seconds. The peak was detected at a level of ~3.3 σ. Therefore we calculate from the Jupiter data that the 1σ 1s sensitivity of the JCMT-THUMPER combination is

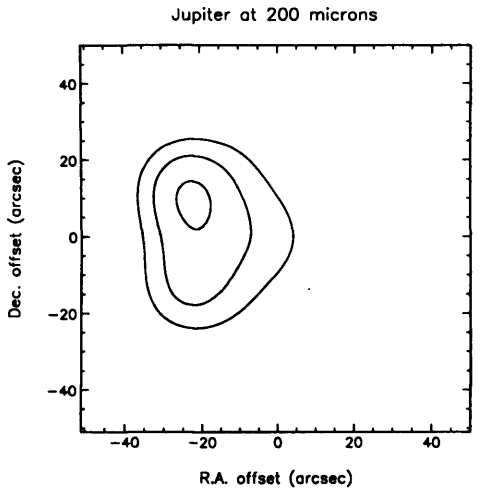

Figure 4.15: First-light astronomical image taken with THUMPER: A 200-μm isophotal contour map of Jupiter. The field of this image roughly corresponds to the size of the THUMPER array. The centre of the array is at (0,0). Contour levels are at 50, 70 & 90% of peak. The fact that the image appears slightly non-circular shows that part of the error-beam of the telescope may be affecting the data. The optical alignment is also slightly offset.

$\sim$63$\pm$10 Jy.

We note that our detection is not at the 5-σ level. However, we believe it is a real detection for a number of reasons: the source was seen in several pixels simultaneously; the structure in the two maps that we took was the same; the source appeared in the same place in both maps; and the NEFD we calculate from the measurements is consistent with that predicted from laboratory measurements of the detector system. In re-griding the map onto an RA-Dec grid as shown in Figure 4.15 some smoothing naturally occurred, as a pixel scale of 5 arcsec was adopted.

The full-width at half-maximum (FWHM) of Jupiter in our map is $\sim$46$\times$38 ($\pm$8) arcsec. At the time of the observations, the diameter of Jupiter was 42 arcsec. When convolved with our 14-arcsec beam, this becomes 44.2 arcsec. Hence our observations are consistent with this. However, the non-circularity visible in the map shows that we are also detecting part of the telescope error beam, which is

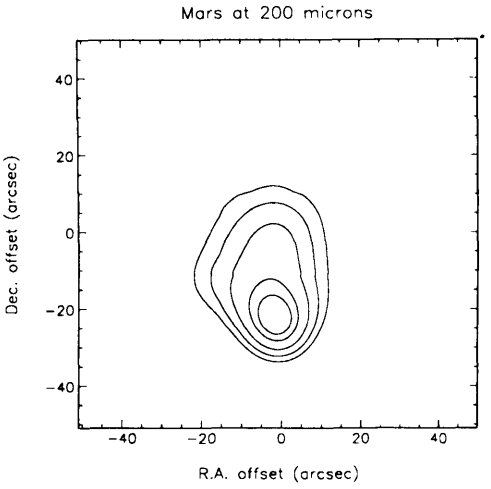

Figure 4.16: A 200-μm isophotal contour map of Mars taken by THUMPER on JCMT. The contour levels are at 50, 60, 70, 80 & 90% of peak. Once again the array centre is at (0,0). The alignment is improved in R.A. The extension to the north is the telescope error beam, which probably also extends to the south, although this was not mapped.

predicted to be significant at this wavelength. We could not trace the error beam further in these data due to their low signal-to-noise ratio.

It is also possible that if we did not have the instrument exactly in focus then this would also contribute to the apparent non-circularity of the beam. We focused the instrument using our model of the telescope and our calculation of the optimal focal position. However, we did not have time to check the focus on-source before Jupiter began to set.

4.6.2 Mars

Later in the night we imaged Mars as it was rising, from airmass 1.30 to 1.29. Figure 4.16 shows our map of Mars. Once again the source is not centred, although we have managed to improve the alignment in R.A. at least, though an adjustment in the DEC pointing is clearly needed. The flux density of Mars at this wavelength can be predicted from planetary modelling in the same way as that of Jupiter

quoted above (Griffin et al., 1986; Orton et al., 1986; Griffin & Orton 1993). Based on this, we expect the peak flux density of Mars to be 8.1 kJy/beam. During the observations the measured value of τ_{225GHz} was 0.0455. Using our relation above, between 1.5 THz and 225 GHz, this corresponds to a value of $\tau_{1.5THz}$ of ~4.32.

Therefore the observed flux density at the telescope is estimated to be 30 Jy/beam. The integration time per point of the map was 50 seconds. The peak was detected at a level of ~3.2 σ. Therefore we calculate from the Mars data that the 1σ 1s sensitivity of the JCMT-THUMPER combination is ~66±10 Jy.

We note once again that our detection is not at the 5-σ level. However, we believe it is also a real detection for similar reasons to those quoted above: the source was seen in several pixels simultaneously; and the NEFD we calculate from the measurements is consistent with that predicted from laboratory measurements of the detector system and with that seen in the Jupiter data.

The map of Mars shows a slightly different morphology from that of Jupiter. The map shows some evidence that the brightest region is more centrally peaked, and that this central peak sits on an extended plateau. Conversely, Jupiter is better fitted by a single gaussian. For Mars the centrally peaked core is of order ~15 arcsec across, with a more extended lobe to the north. The core is consistent with the FWHM that would be expected from Mars, since at the time of the observation the diameter of Mars was 6 arcsec. When convolved with our beam this produces a gaussian of FWHM 15.2 arcsec, consistent with the image in Figure 4.16.

The extended emission to the north is most likely to be the error-beam of the telescope. The level of the extended error-lobe is roughly two-thirds of the magnitude of the main beam. This may also extend to the south and south-east,

but our map does not extend far enough in these directions to say. Once again the instrument focus may be adding to the problem. By the time we repeated the map the shift was coming to an end and the sun had risen. Subsequently, the conditions worsened (the sky noise level increased) and we did not detect Mars again in day-time. Our mean 1σ 1s sensitivity measured on the planets is therefore $\sim$65$\pm$10 Jy.

4.7 The Sun

Once the Sun had risen we pointed the telescope at the Sun, when it was in the airmass range 1.44 to 1.43, and detected it clearly in all channels, at high levels of signal-to-noise ratio of up to 560 σ. Obviously, we did not map the full extent of the Sun, but rather used it as a bright, uniform, extended black-body source, and chopped across the limb of the Sun. We estimate that the emission from the Sun is $\sim$1.1 MJy/beam. It was at $\sim$1.4 airmasses during our observation, and τ_{225GHz} was 0.047 ($\tau_{1.5THz}$ $\sim$4.5). We used 5-second integrations, so we estimate our 1σ 1s sensitivity on the Sun to be $\sim$9 Jy (1σ 1s).

This is a factor of $\sim$7 better than that estimated from the essentially point-like planet Mars. This implies that only roughly one-seventh ($\sim$15%) of the total power incident upon the JCMT dish at 200 μm is focused into a 14-arcsec central beam. We had predicted that, due to the surface inaccuracies of the JCMT dish (which was not designed to operate at this high a frequency), there would be significant power in the side-lobes.

The measurement of the surface accuracy of the dish which is closest in time to our observations was taken on 2005 February 13, at which time the dish surface

accuracy was found to be 23.8 μm rms (Wouterloot 2005). Using the standard calculation of Ruze efficiency we estimate that a dish of this accuracy would concentrate $\sim$11% of the total power into a 14-arcsec beam. This is consistent with the $\sim$15% we estimate here based on the ratio of sensitivities measured on Mars and the Sun. Hence we see that all of our observations are self-consistent.

4.8 Summary

In this chapter I have outlined the observations that were carried out with THUMPER on the JCMT. Weather limited the amount of available observing time. Nevertheless we successfully characterised the atmospheric transmission at 200 μm on Mauna Kea. In addition we made the first 200 μm ground based astronomical images when we mapped Jupiter and Mars. Upgrades to the JCMT prevented further observing runs. The results of the THUMPER observing run are presented in Ward-Thompson et al. (2005).

Chapter 5

Methanol Masers and Infrared Counterparts

5.1 The Methanol Maser Multibeam Survey

The Methanol Multibeam (MMB) Survey is a Galactic Plane survey for both 6.668 GHz methanol and 6.035 GHz excited OH, observing between $0° < l < 360°$ and $|b| \leq 2°$. The survey will take about 200 days, split between the Parkes telescope in the southern hemisphere and the Lovell telescope in the northern. All detections will have high-resolution follow-up observations using the Australian Telescope Compact Array (ATCA) and the Multi-Element Radio Linked Interferometer Network (MERLIN). In addition to the Galactic Plane survey, the MMB project will incorporate a survey of the Small and Large Magellanic Clouds and a pulsar survey piggyback. For further details, see Cohen et al. (2007), Green et al. (2007).

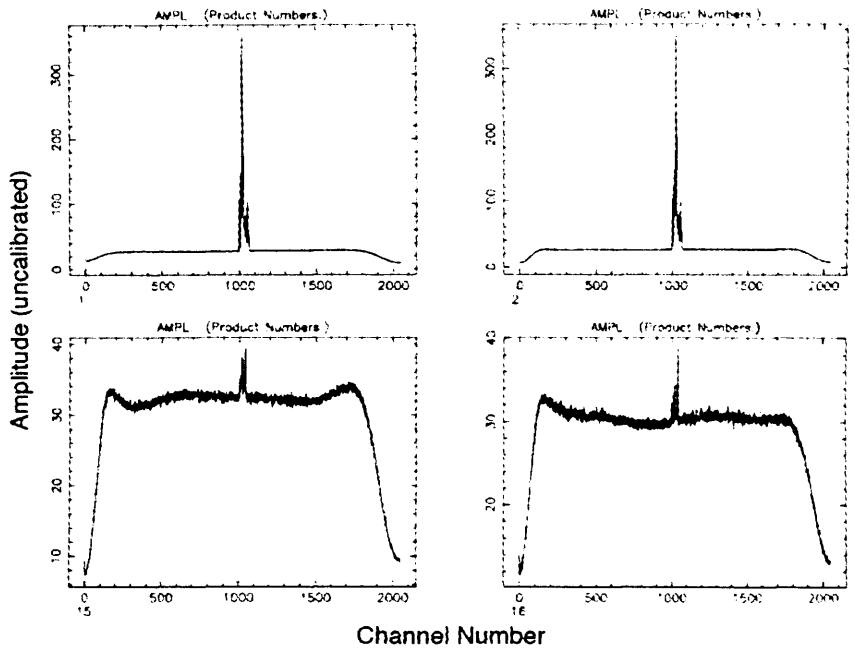

Figure 5.1: First light of the MMB survey, maser source G309.21+0.48. Top spectra are 6.668 GHz methanol in both left and right polarisations, bottom are 6.035 GHz OH in both polarisations.

As explained in section 1.6.4, the survey of the Galactic Plane for this particular transition of methanol maser can also be considered as a search for all the sites of high mass star formation that lie there. These sites are then used to search through IR point source catalogues (section 5.2) so that SEDs of these sources can be constructed (section 6.1). This will begin the process of characterising these sources. A description of the conditions which give rise to maser emission is given in section 1.6.

The survey uses a new seven beam receiver which was constructed as a joint project between Jodrell Bank Observatory and the Australia National Telescope Facility. The receiver has an hexagonal array of seven identical feeds capable of dual circular polarisation over a large bandwidth. The receiver was commissioned at Parkes during January 2006 and took first light on the 22^{nd} of January. Figure 5.1 shows the first light image.

The Parkes observations of the MMB survey are over 60% complete and have yielded 518 maser detections of which 218 are new. The Parkes stage of the survey will be complete in 2008, at which point the receiver will move to Jodrell to complete the Galactic survey by 2010. The final MMB catalogue of 6.668 GHz methanol should thus be complete by 2011.

5.1.1 Survey and observational details

A bandwidth of 4 MHz is used by the correlator for the observations at Parkes, which, at 6.668 GHz, equates to 180 kms^{-1}. However, a velocity range of only 150 kms^{-1} is taken as fully usable due to band edge effects. The centre velocities and range for observations have been determined from the Galactic CO emission of Dame, Hartmann and Thaddeus (2001). To fully cover the required velocities there is one setting for $|l| > 20°$, two for $6° < |l| < 20°$, three for $2° < |l| < 6°$ and four for $|l| < 2°$. More velocity settings are needed closer to the Galactic centre because that is where there is a greater dynamical range. Figure 5.2 is a longitude-velocity map taken from Dame et al. 1987 who surveyed the entire Galactic Plane in CO. The map shows the greater range of velocities around the Galactic centre. It should be noted that the full extent of the centre velocities are not mapped on this figure, it is merely shown to illustrate the greater range there compared to those at further longitude.

The correlator has 2048 frequency channels for each IF and polarisation, resulting in 28 × 2048 spectra which are dumped every five seconds. Across the 4 MHz band at 6.668 GHz, the 2048 channels give a resolution of 0.0879 kms^{-1} which is less than the typical minimum velocity width of methanol masers (0.1 kms^{-1}).

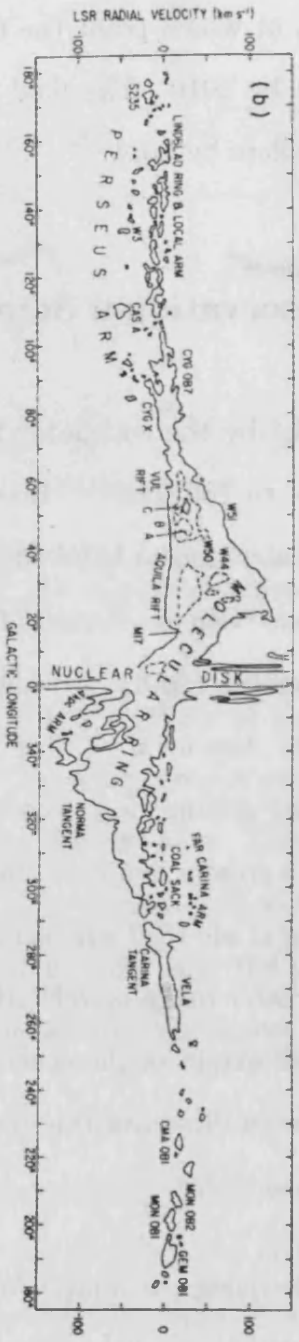

Figure 5.2: Longitude-velocity CO map of the Galactic Plane. Taken from Dame et al. 1987.

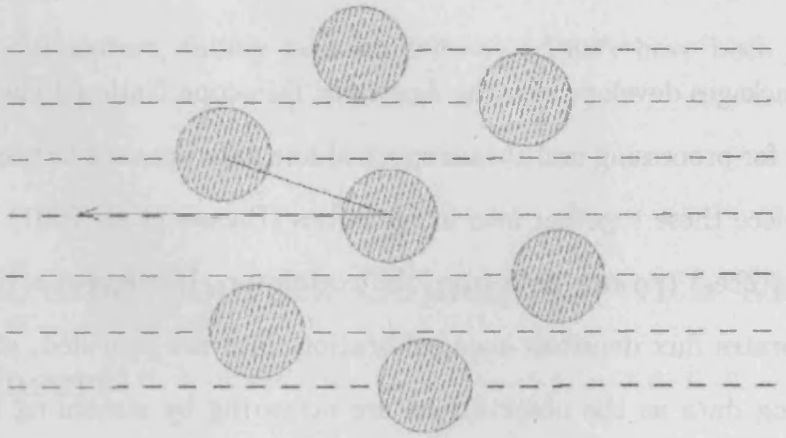

Figure 5.3: Multibeam footprint, oriented at 19.1° to the Galactic Plane.

The survey is observing the entire Galactic Plane to a latitude of ± 2°. This area is split into blocks which are 2° in longitude and 4° in latitude. To sample these blocks the receiver beam pattern is scanned in longitude, taking 20 minutes to complete the 2°, then moved in latitude by 1.23 arcmins and scanned back. The beam pattern is then shifted by 15 arcmins to begin the next scan pair; the beams of the receiver have a FWHM of 3.2 arcmins at 6.68 GHz and are separated by 6.46 arcmins, giving a total footprint which is 15 arcmins wide. This beam pattern is rotated to an optimal angle of 19.1° with respect to the scan direction (see Figure 5.3) to maintain equal beam spacings (Condon, Broderick and Seielstad 1989). To fully sample a 2° by 4° block 32 scans are required, which, at 20 minutes each means a block is observed in 10 hours. For the majority of the survey, i.e. away from the Galactic centre, only one pass is needed for each block. There is negligible RFI at 6 GHz at the Parkes site, which also aids observations.

5.1.2 Data Reduction

Software packages developed by the Australia Telescope National Facility (ATNF) specifically for processing multibeam spectral line data are used to process the data and then piece these together into image cubes (Barnes et al. 2001). LIVEDATA is used to process the raw data from the correlator. It removes a bandpass estimate, calibrates flux densities once calibration data are provided, and is capable of processing data as the observations are occurring by streaming the raw data dumps from the correlator. The output are single dish FITS files, one for each scan, which are gridded together using GRIDZILLA. AIPS is used to produce final images.

5.1.3 Survey Results

In the first 18 months after commissioning the new receiver, observations have been made at Parkes over 53 days, completing 106° of longitude. This represents 64% of the Parkes part of the survey and 32% of the total survey. The observations have yielded 518 methanol maser detections, of which 218 represent new sources. Most of the new detections are below 4 Jy, typically around 1 Jy peak intensity, with linewidth FWHMs of less than 0.2 kms^{-1}. The detections include several far-side outer Galaxy masers.

5.1.4 High Resolution Follow Up

The positional accuracy of the masers detected by Parkes is around 30 arcsec. These detections are then observed with MERLIN and ATCA to attain sub-arcsec

accuracy. All 218 of the new sources have been observed and positioned using ATCA, and 30 sources, falling between $20° < l < 30°$, have been observed by MERLIN.

5.2 Infrared Sources Coincident with Methanol Masers

As of April 2007, when I carried out the analysis described in this chapter, 518 Methanol masers were known to reside in the Plane of the Galaxy. This number includes masers that had been observed prior to the MMB survey as well as the 218 new detections. Of these 518, 321 had been positioned with sub-arcsec accuracy, and these positions were used to search through the ISO point source catalogue. Methanol masers which were within 30 arcsec of an ISO source (as found in the point source catalogue) were then used to search through the 2MASS, IRAS and MSX catalogues. After further work which highlighted source confusion, 2MASS data were discarded. A brief description of ISO, IRAS and MSX follows.

5.2.1 ISO

The Infrared Space Observatory (ISO) (Kessler et al. 1996) was the first orbiting infrared observatory for pointed observations and was launched in 1995. Its 0.6 m primary mirror was cooled to liquid helium temperatures and enabled ISO to observe with considerable sensitivity with spatial resolutions between 1.5 and 90 arcsec. ISO comprised four instruments: two spectrometers (SWS (de Graauw et al. 1996) and LWS (Clegg et al. 1996)), a camera (ISOCAM) (Cesarsky et al.

1996), and an imaging photo-polarimeter (ISOPHOT) (Lemke et al. 1996).

Only observations that were made as part of the ISOGAL (Schuller et al. 2003) survey were directed at the Galactic Plane and as a result the only ISO images used in this work were from that survey.

ISOGAL

ISOGAL was a 7 and 15 micron survey of the inner Galactic disk performed with the ISO camera, ISOCAM, and mostly produced images with 6" pixels. Its sensitivity was approximately 10 mJy at both wavelengths. This makes it about 100 times more sensitive than IRAS at 12 μm.

There were 255 hours of observation and an more than 20 square degrees of sky was observed, mostly at the two wavelengths. The observed fields sample the inner Galactic disk, mostly with $|l| < 30$ deg. and $|b| < 1$ deg (Schuller et al. 2003).

The ISOGAL sources were systematically cross-identified with the I, J, K sources of the DENIS survey.

5.2.2 DENIS

In coordination with the ISOGAL project, dedicated observations with the DENIS (Deep Near Infrared Survey of the Southern Sky) instrument on the ESO 1 metre telescope at La Silla (Epchtein et al. 1994). DENIS observed at 0.82, 1.25 and 2.15 μm, with limiting magnitudes of 18.5, 16.5 and 14.0 respectively.

5.2.3 IRAS

The Infrared Astronomical Satellite (IRAS) was a joint project of the US, UK and the Netherlands. The IRAS mission was launched in 1983 and performed an unbiased, all sky survey at 12, 25, 60 and 100 μm, the average sensitivity of each band being: 0.7, 0.65, 0.85 and 3,0 Jy, respectively (Beichman et al. 1988).

5.2.4 MSX

The Midcourse Space Experiment (MSX) was launched in early 1996 into a 900 km, near-Sun-synchronous orbit. Its wavelength of operation was from 4.2 to 26 μm; the bands in the MSX point source catalogue were: 4.29, 4.35, 8.28, 12.13, 14.65 and 21.34 μm, with a sensitivity between 1.1 and 1.3 Jy at 12.13 μm. (Egan et al. 1999). As well as a variety of other experiments MSX fully surveyed the Galactic Plane up to a latitude of 5 degrees.

5.3 Results from the Point Source Catalogues

Only 57 of the 321 accurately positioned Methanol Masers were in an ISOGAL observational field, and of these 57, 45 were within 30 arcsec of an ISO source, as defined in the ISO Point Source Catalogue. Velocity, flux and positional information for all 57 masers are displayed in table 5.1.

Methanol Maser Number	Galactic Longitude Degrees	Galactic Latitude Degrees	Velocity kms^{-1}	Maser Flux Jy
MM 01	330.283	0.493	-88.5	2.6
MM 02	330.226	0.290	-75.3	0.9
MM 03	334.138	-0.023	-31.2	2.4
MM 04	338.069	0.011	-40.1	0.8
MM 05	338.075	0.012	-53	18.8
MM 06	338.075	0.009	-38.2	3.5
MM 07	358.722	-0.126	10.6	3.2
MM 08	358.809	-0.085	-56.2	7.2
MM 09	358.931	-0.030	-15.9	4.5
MM 10	359.138	0.031	-4	15.6
MM 11	359.436	-0.102	-53.6	4.2
MM 12	359.436	-0.104	-52	26.8
MM 13	358.841	-0.737	-20.7	9
MM 14	358.841	-0.738	-17.6	1.6
MM 15	0.496	0.188	0.8	10
MM 16	0.376	0.040	37	0.7
MM 17	0.475	-0.010	28.9	2.7
MM 18	0.836	0.184	3.5	8.1
MM 19	0.666	-0.029	72.2	33.7
MM 20	0.677	-0.025	73.4	4.4
MM 21	0.673	-0.029	66	0.4
MM 22	0.667	-0.034	55.2	0.4
MM 23	0.672	-0.031	58.2	4.5
MM 24	0.665	-0.036	60.4	2.1
MM 25	1.008	-0.237	0.2	14
MM 26	21.880	0.014	20.6	5.5
MM 27	25.710	0.044	95.5	386
MM 28	28.607	0.018	106.4	1.8
MM 29	30.371	0.483	19.4	0.7
MM 30	30.819	0.273	104.6	5
MM 31	30.781	0.231	48.8	27
MM 32	30.790	0.205	85.7	29
MM 33	30.011	-0.273	106.1	1.5
MM 34	30.010	-0.274	103.2	1.1
MM 35	30.980	0.216	111.1	1
MM 36	30.898	0.162	101.8	79
MM 37	30.850	0.122	27.6	0.59
MM 38	30.420	-0.232	103	13
MM 39	31.061	0.094	16.2	24
MM 40	31.122	0.063	48	1.1
MM 41	334.307	-0.079	-36.8	1.5
MM 42	334.635	-0.015	-30	36.4
MM 43	358.906	0.106	-18.2	1.7
MM 44	22.357	0.066	80	10
MM 45	25.826	-0.178	91.5	65
MM 46	337.710	0.089	-72.6	5
MM 47	337.705	-0.053	-54.6	173
MM 48	0.212	-0.001	49.2	3.5
MM 49	0.665	-0.042	49.1	65
MM 50	0.657	-0.041	52	3
MM 51	0.651	-0.049	48	31.7
MM 52	0.647	-0.055	51	3.4
MM 53	0.695	-0.038	68.5	26
MM 54	1.147	-0.124	-20.8	4.6
MM 55	2.536	0.198	3	40
MM 56	30.424	0.466	7.9	1.2
MM 57	31.076	0.457	25.2	0.2

Table 5.1: Velocity, flux and positional information for 57 Methanol masers which are in an ISOGAL observational field. Methanol masers 1 to 45 are associated with an ISO source. Methanol masers 46 to 57 are not associated with an ISO source.

The 45 sites with ISO sources associated with Methanol maser emission were then used to search through the MSX, 2MASS and IRAS catalogues. After this initial search through the various point source catalogues, it was decided to not pursue 2MASS data; the large number of sources found within a radius of 10 arcsec of a Methanol maser site led to confusion and made it difficult to determine whether the source was at the same distance, or actually lay in front of the maser. Table 5.2 shows the association between Methanol masers, MSX, DENIS and ISO sources and the relevant flux densities.

MM Number	DENIS I 0.79 μm	DENIS J 1.22 μm	DENIS K 2.14 μm	MSX B1 4.29 μm	MSX B2 4.35 μm	MSX A 8.28 μm	MSX C 12.13 μm	MSX D 14.65 μm	MSX E 21.34 μm	ISO 6.7 μm	ISO 6.8 μm	ISO 7.7 μm	ISO 14.3 μm	ISO 14.9 μm
MM 01	-	-	-	-1.09E+01	-5.91E+00	1.39E+00	1.42E+00	2.70E+00	1.67E+01	1.56E+00	-	-	5.55E-03	-
MM 02	-	-	-	-1.09E+01	-5.91E+00	8.60E-01	1.42E+00	8.05E-01	-1.37E+00	4.66E-01	-	-	8.89E+01	-
MM 03	1.22E-02	3.55E-02	1.10E-01	-1.58E+00	-8.50E+00	1.90E-01	-8.50E-01	8.00E-01	1.54E+00	2.53E-34	-	-	7.11E-01	-
MM 04	-	-	-	-	-	-	-	-	-	-	-	1.50E+00	1.96E+00	-
MM 05	-	-	-	-	-	-	-	-	-	-	-	1.53E+00	1.89E+00	-
MM 06	-	-	-	-	-	-	-	-	-	-	-	-	-	-
MM 07	-	5.48E-03	6.02E-01	-	-	-	-	-	-	-	9.12E-02	-	-	5.15E-02
MM 08	4.85E-05	6.53E-04	8.94E-02	-1.19E+01	-6.42E-01	1.58E-01	-5.87E-01	-4.23E-01	-1.19E+00	-	2.00E-01	-	-	-
MM 09	-	7.56E-03	2.99E+00	-1.73E-01	-9.34E-01	9.46E-01	1.29E+00	2.10E+00	2.30E+00	-	1.27E+00	-	-	4.87E+00
MM 10	1.99E-04	3.93E-03	5.39E-01	-8.65E+00	-4.67E+00	3.81E-01	6.69E-01	8.50E-01	2.05E+00	-	2.11E-01	-	-	9.64E-01
MM 11	-	-	9.54E-02	-1.29E+01	-6.98E+00	1.28E-01	1.29E+00	4.77E+00	1.82E+01	-	-	-	-	2.38E+00
MM 12	-	-	1.26E-01	-1.29E+01	-6.98E+00	1.28E-01	1.29E+00	4.77E+00	1.82E+01	-	-	-	3.94E-02	-
MM 13	-	-	-	-8.34E+00	-4.50E+00	1.87E+00	1.87E+00	7.26E-01	2.52E+00	-	-	-	-	-
MM 14	-	-	-	-8.34E+00	-4.50E+00	1.87E+00	1.87E+00	7.26E-01	2.52E+00	-	-	-	-	-
MM 15	-	-	-	-6.08E+00	-3.28E+00	3.66E-01	6.10E-01	6.30E-01	1.67E+00	-	1.56E-01	-	-	-
MM 16	-	1.80E-03	2.65E-01	-8.65E+00	-4.67E+00	1.76E-01	-4.76E-01	5.58E-01	-1.09E+00	-	8.17E-02	-	-	-
MM 17	-	8.37E-04	1.83E-01	-	-	-	-	-	-	-	4.88E-02	3.84E-02	-	-
MM 18	-	-	-	-9.24E+00	-4.99E+00	9.99E-01	1.25E+00	7.18E-01	2.26E+00	-	8.89E+01	-	1.24E+00	1.11E+00
MM 19	2.79E-04	3.79E-03	2.27E-01	-	-	-	-	-	-	-	4.45E-02	-	-	-
MM 20	-	-	-	-	-	-	-	-	-	-	-	-	-	-
MM 21	-	-	-	-	-	-	-	-	-	-	-	-	-	-
MM 22	-	-	-	-	-	-	-	-	-	-	6.73E-02	-	-	2.91E-02
MM 23	-	-	-	-	-	-	-	-	-	-	-	-	-	-
MM 24	-	-	-	-	-	-	-	-	-	-	-	-	-	-
MM 25	-	-	-	-8.65E+00	-4.67E+00	2.78E-01	-4.76E-01	-3.41E-01	-1.09E+00	-	-	1.01E-01	8.39E-02	7.52E-02
MM 26	-	-	-	-	-	-	-	-	-	-	-	3.91E+00	8.32E+00	-
MM 27	-	-	-	-1.12E+01	-6.04E+00	7.70E-01	9.21E-01	9.45E-01	-1.42E+00	-	-	3.02E+00	-	8.95E+00
MM 28	-	9.97E-04	-	-3.34E+00	-1.80E+00	2.89E+00	7.36E+00	9.83E+00	2.97E+01	-	-	-	-	-
MM 29	-	-	-	-	-	-	-	-	-	-	-	8.39E-02	3.22E-01	2.88E-01
MM 30	-	-	1.96E-01	-1.02E+01	-5.51E+00	9.37E-01	1.43E+00	2.80E+00	1.47E+01	-	-	1.79E+00	-	3.02E+00
MM 31	-	-	-	-1.02E+01	-5.51E+00	4.35E-01	-5.38E-01	-3.94E-01	-1.22E+00	-	-	1.45E-01	-	2.58E-01
MM 32	-	-	-	-1.02E+01	-5.51E+00	7.46E-01	8.86E-01	5.27E-01	-1.22E+00	-	-	6.86E-01	-	2.17E-01
MM 33	1.79E-03	9.44E-02	1.32E+00	-	-	-	-	-	-	1.05E-01	-	-	1.31E-02	-
MM 34	1.79E-03	9.44E-02	1.32E+00	-	-	-	-	-	-	1.05E-01	-	-	1.31E-02	-
MM 35	-	-	-	1.97E+01	-5.51E+00	9.35E-01	1.23E+00	1.04E+00	-1.22E+00	1.32E+00	1.19E+00	9.38E-01	-	8.47E-01
MM 36	-	-	-	-	-	-	-	-	-	-	-	8.47E-01	-	-
MM 37	-	-	4.16E-01	1.16E+01	-6.75E+00	4.63E-01	6.17E-01	4.75E-01	-1.50E+00	-	-	3.28E-01	-	2.33E-01
MM 38	-	-	-	-	-	-	-	-	-	-	-	3.28E-01	-	8.39E-02
MM 39	-	-	-	1.85E+01	-6.04E+00	6.73E-01	9.29E-01	1.02E+00	3.89E+00	-	-	1.08E+00	-	8.63E-01
MM 40	-	-	-	-1.12E+01	-6.04E+00	3.59E-01	-6.01E-01	-4.34E-01	-1.23E+00	-	-	-	-	3.77E-02
MM 41	1.04E-03	8.85E-03	1.07E+00	-9.99E+00	-5.39E+00	6.96E-01	6.71E-01	6.66E-01	-1.25E+00	3.28E-01	-	-	8.05E-02	-
MM 42	4.85E-04	1.24E-03	2.03E-02	-9.99E+00	-5.39E+00	1.63E-01	-5.49E-01	-3.94E-01	1.22E+00	7.64E-02	-	-	-	-
MM 43	-	1.16E-02	1.85E-01	-1.29E+01	-6.98E+00	1.77E-01	-6.94E-01	4.90E-01	-1.41E+00	-	7.68E-02	1.13E-01	-	1.22E-01
MM 44	2.98E-02	3.93E-02	2.20E-02	-1.12E+01	-6.04E+00	1.38E+00	2.17E+00	1.51E+00	6.30E+00	1.59E-01	-	-	2.67E-01	-
MM 45	-	-	4.52E-02	-	-	-	-	-	-	6.15E-01	-	-	5.61E-02	-

Table 5.2: Association between Methanol masers, DENIS, MSX and ISO sources, and the flux densities in Jy.

5.4 ISO IMAGES

To check the validity of the source associations with the maser sites, ISO images were accessed from the ISO archive. Displaying these images together with the positions of the maser sites and associated point sources from the ISO/MSX/IRAS catalogues, it became apparent that the peak of the ISO source was not necessarily where the maser lay, in fact, it rarely was. For consistency, the peak value from the eight surrounding pixels was recorded. This was then combined with data from the DENIS, MSX and IRAS point source catalogues, with the IRAS and DENIS data being used as upper limits to form the first SEDs.

Figures 5.4 to 5.22 present the ISO images which were retrieved from the ISO archive. Overlaid on these maps are the positions of the associated ISO, IRAS and MSX sources, as well as the methanol masers. The ISO sources which are plotted on the maps have been positioned using data from the ISOGAL point source catalogue. The errors in the IRAS and MSX positions are represented by ellipses and diamonds respectively. The errors in the positions of the methanol masers are negligible in relation to the pixel scale of the images.

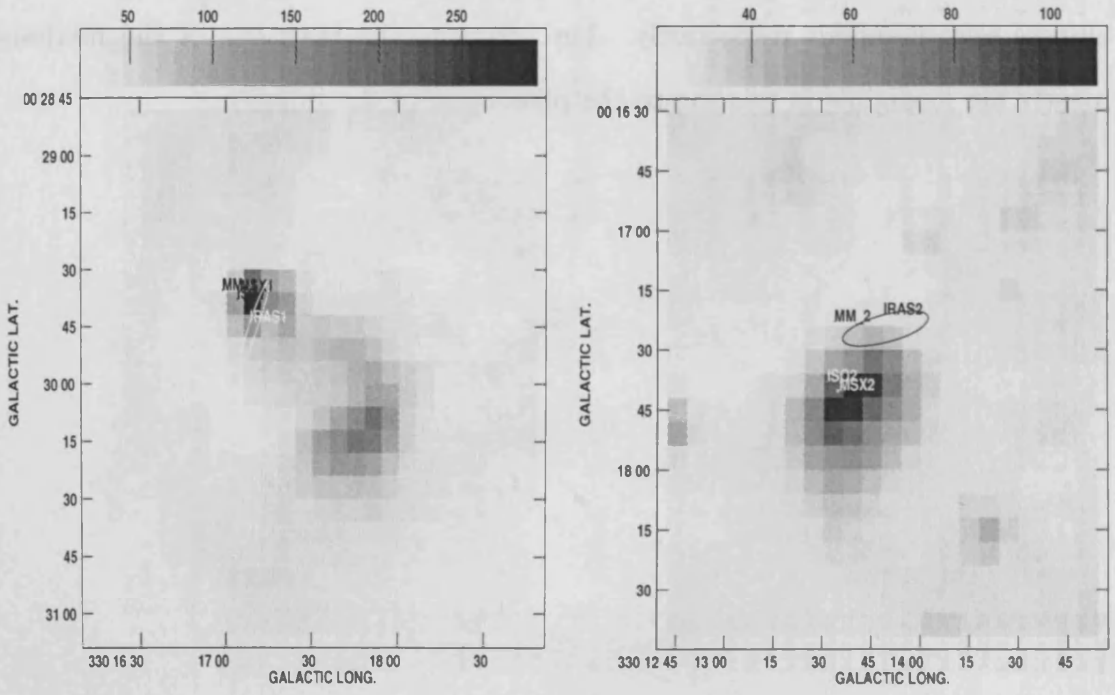

Figure 5.4: ISO images associated with methanol maser 1 (left) and 2 (right)

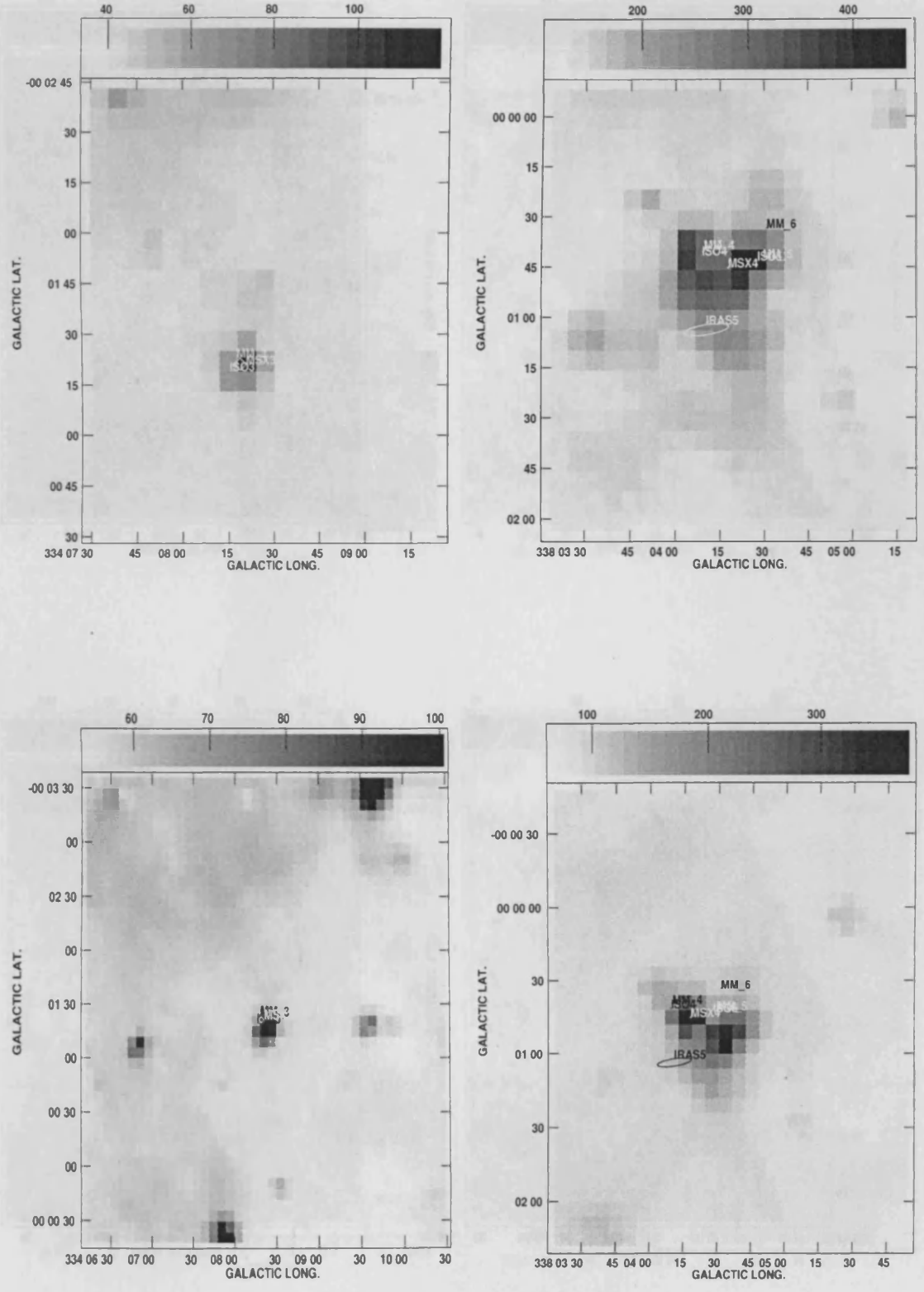

Figure 5.5: ISO images associated with methanol maser 3 (left) and 4, 5 & 6 (right).

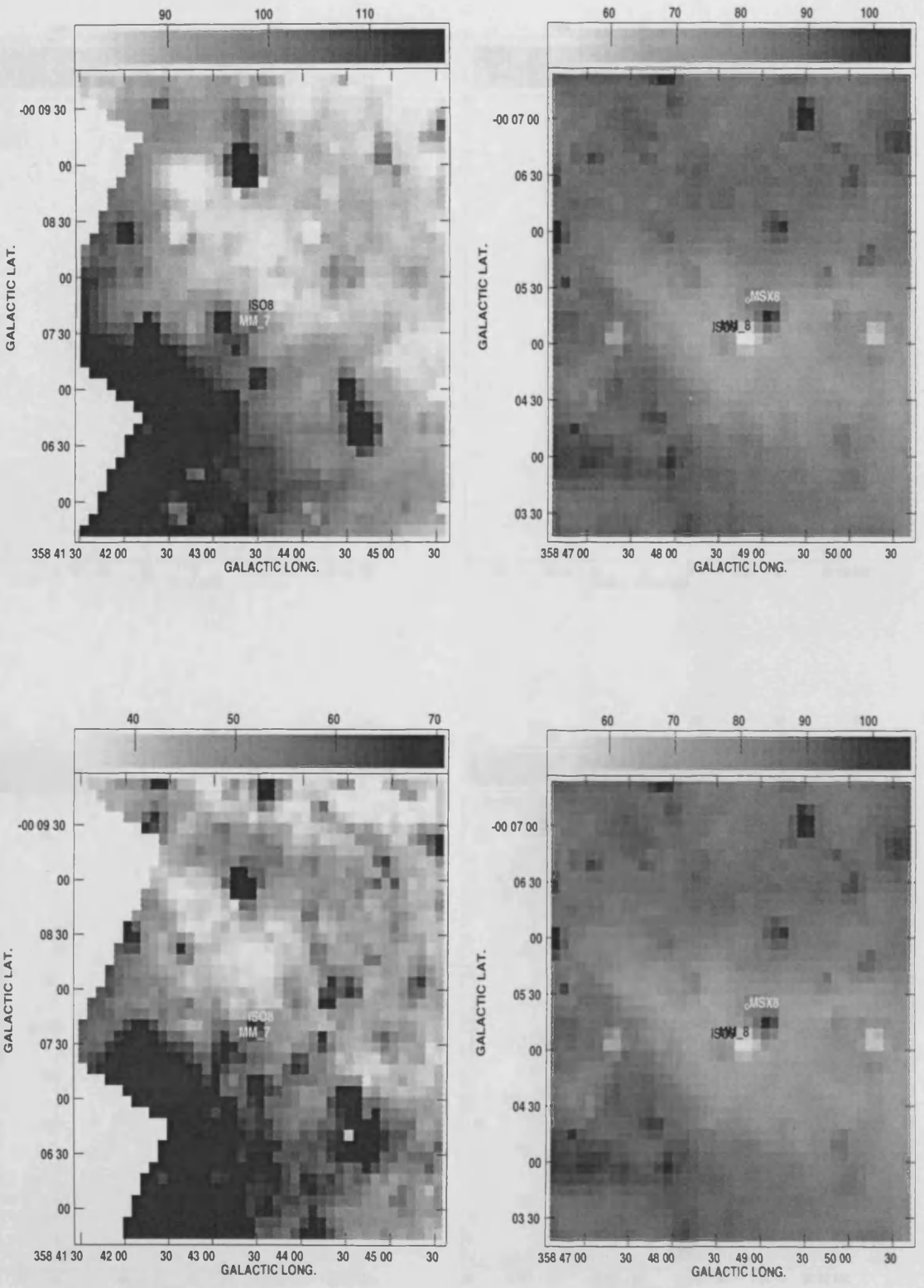

Figure 5.6: ISO images associated with methanol maser 7 (left) and 8 (right).

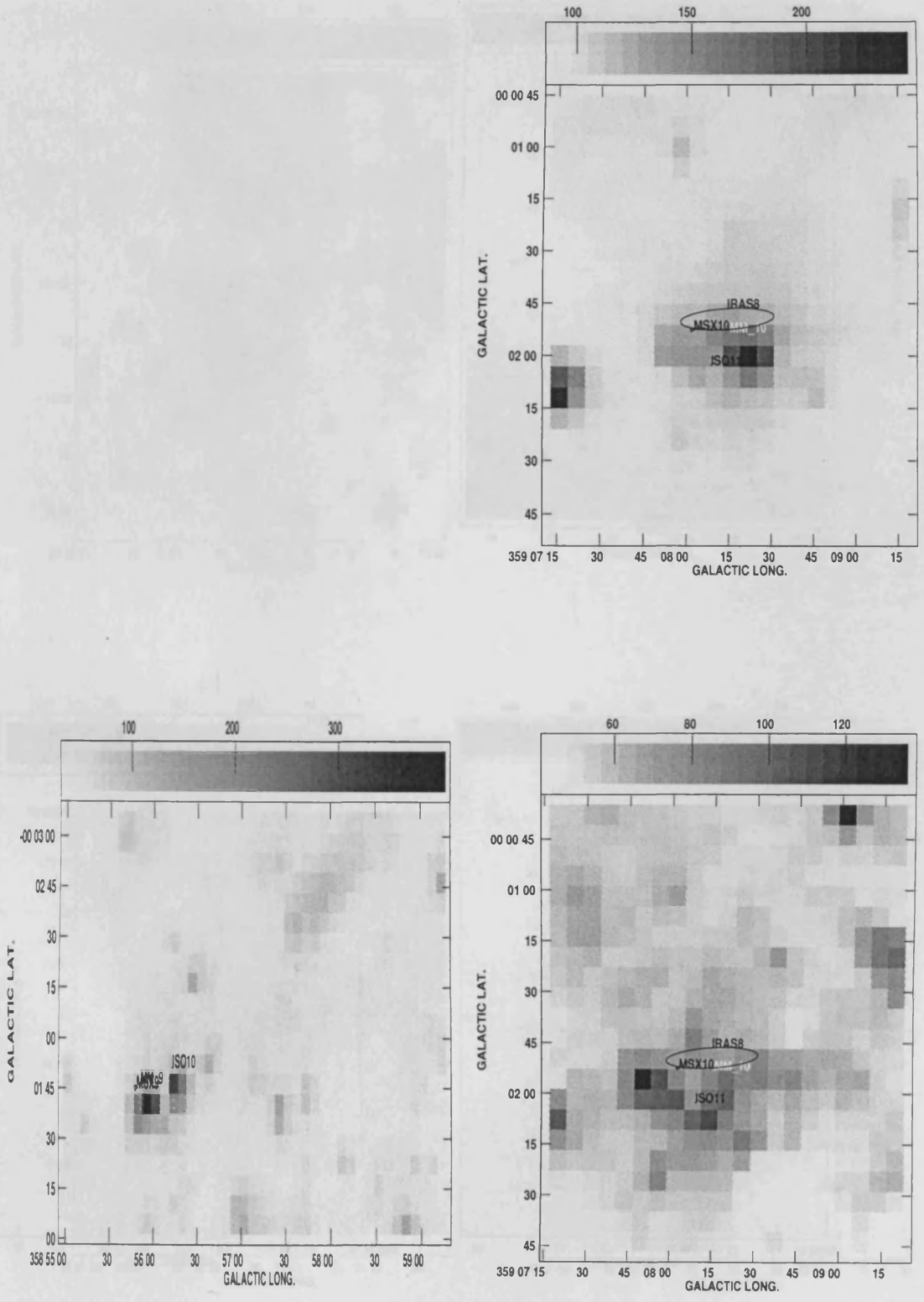

Figure 5.7: ISO images associated with methanol maser 9 (left) and 10 (right).

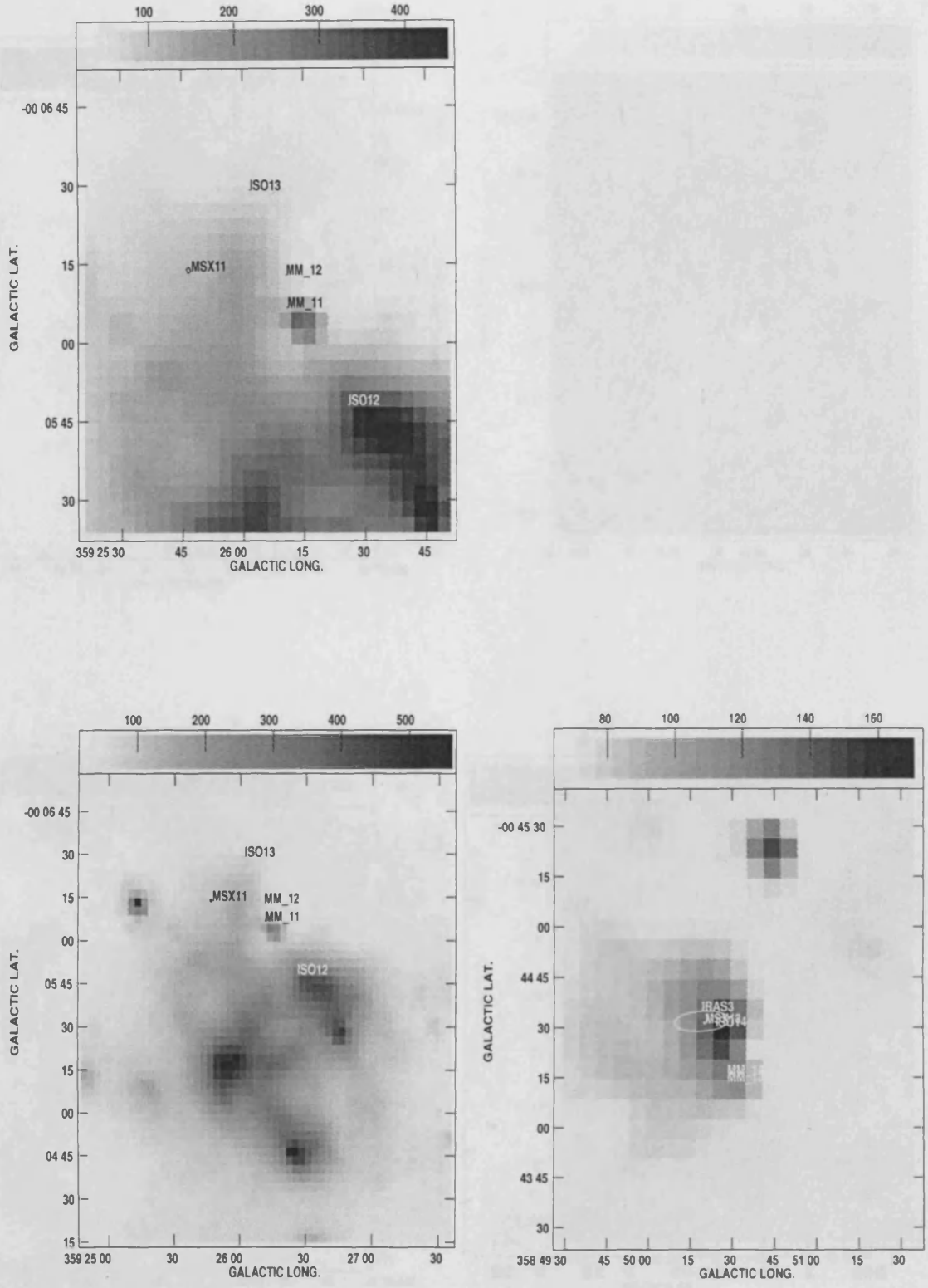

Figure 5.8: ISO images associated with methanol maser 11 & 12 (left) and 13 & 14 (right).

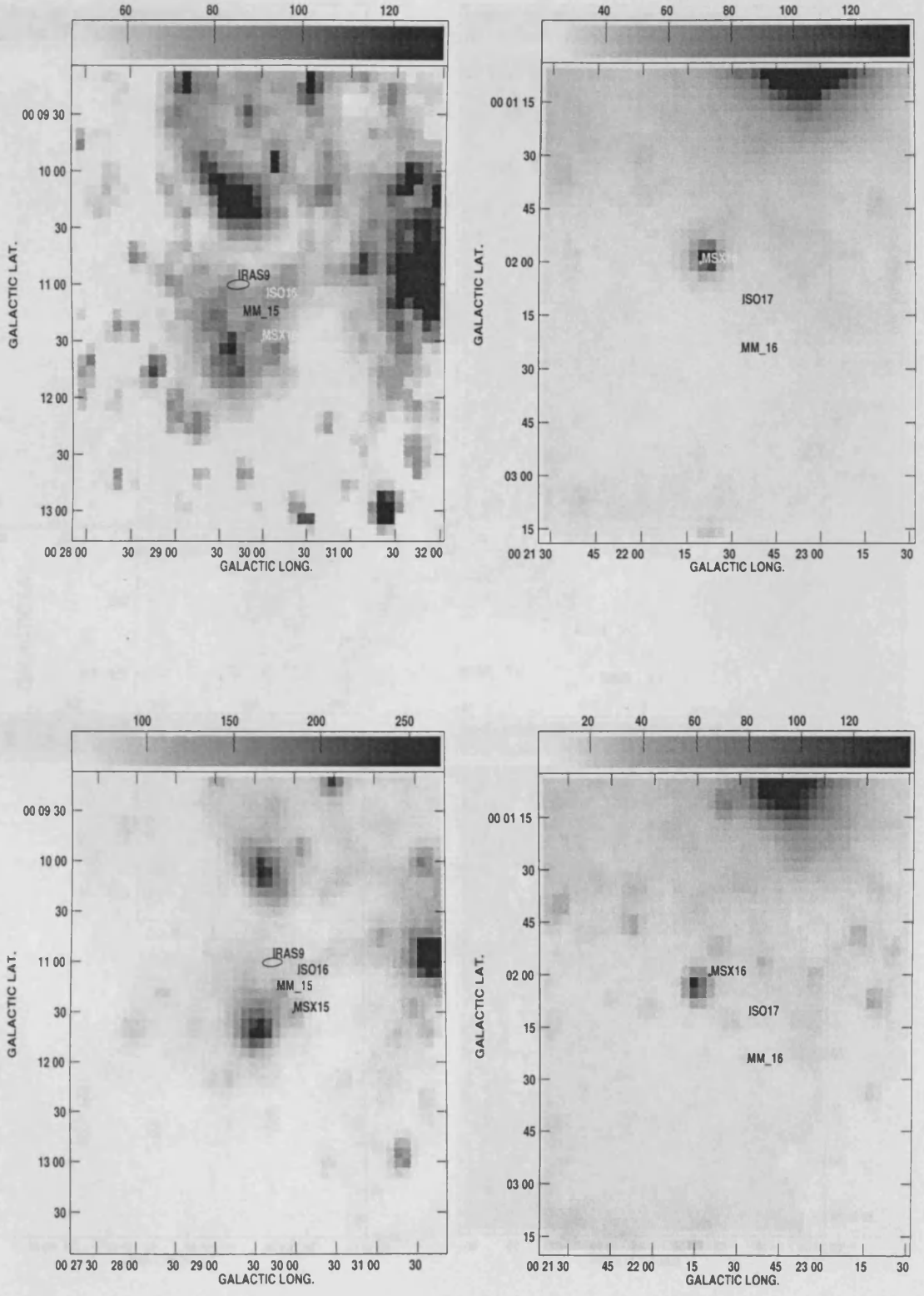

Figure 5.9: ISO images associated with methanol maser 15 (left) and 16 (right).

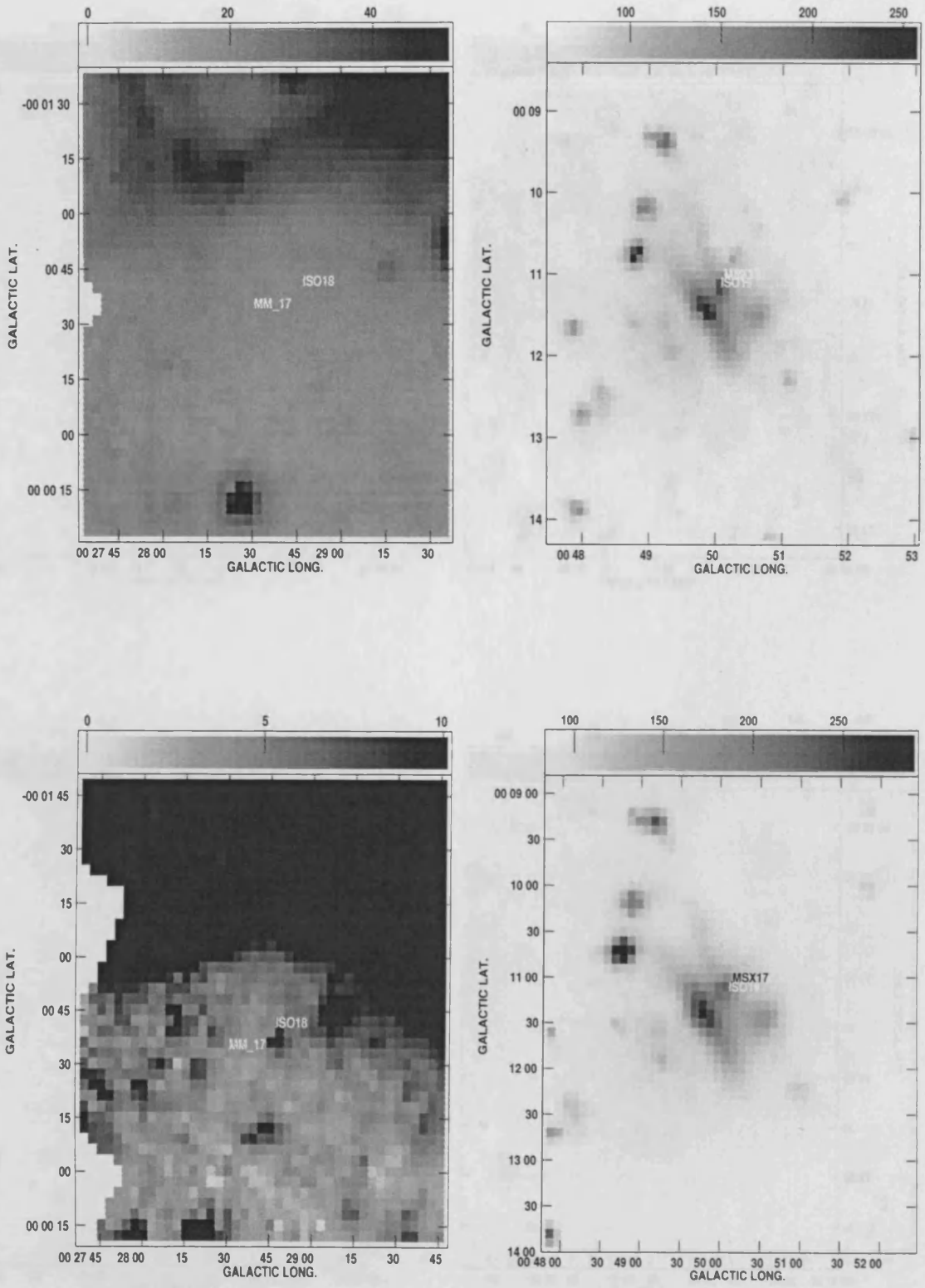

Figure 5.10: ISO images associated with methanol maser 17 (left) and 18 (right)

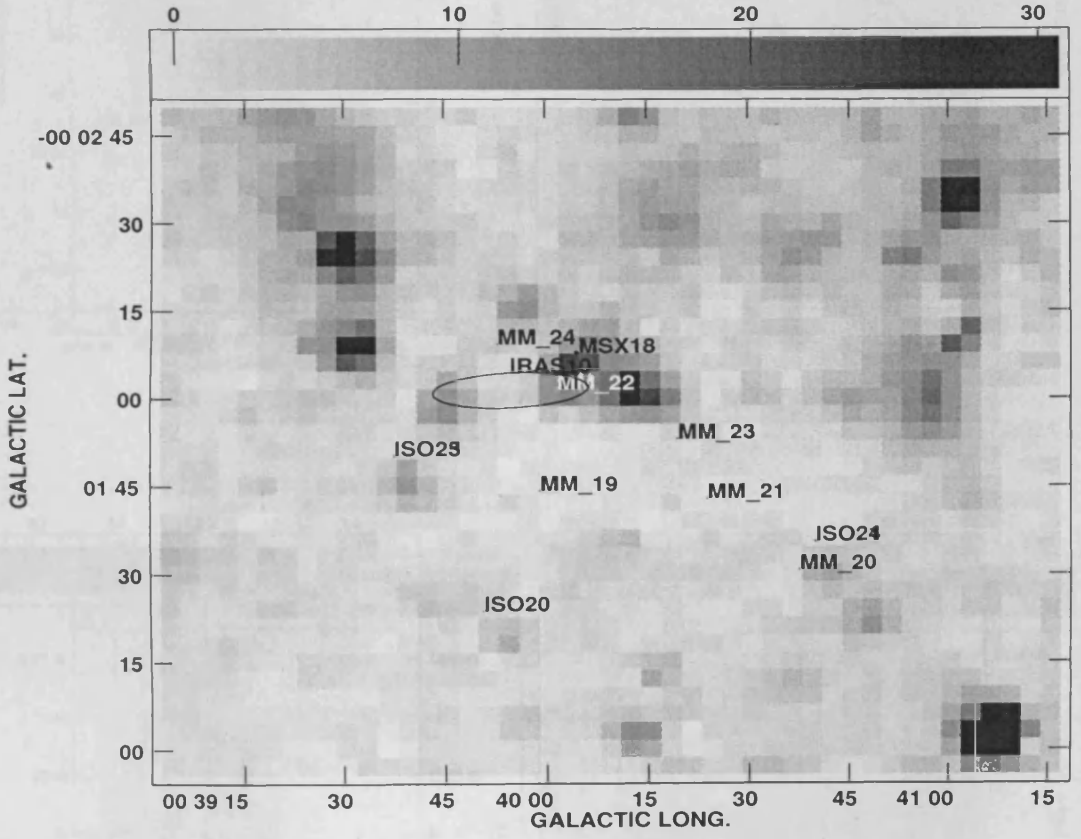

Figure 5.11: ISO images associated with methanol masers 19, 20, 21, 22, 23 and 24

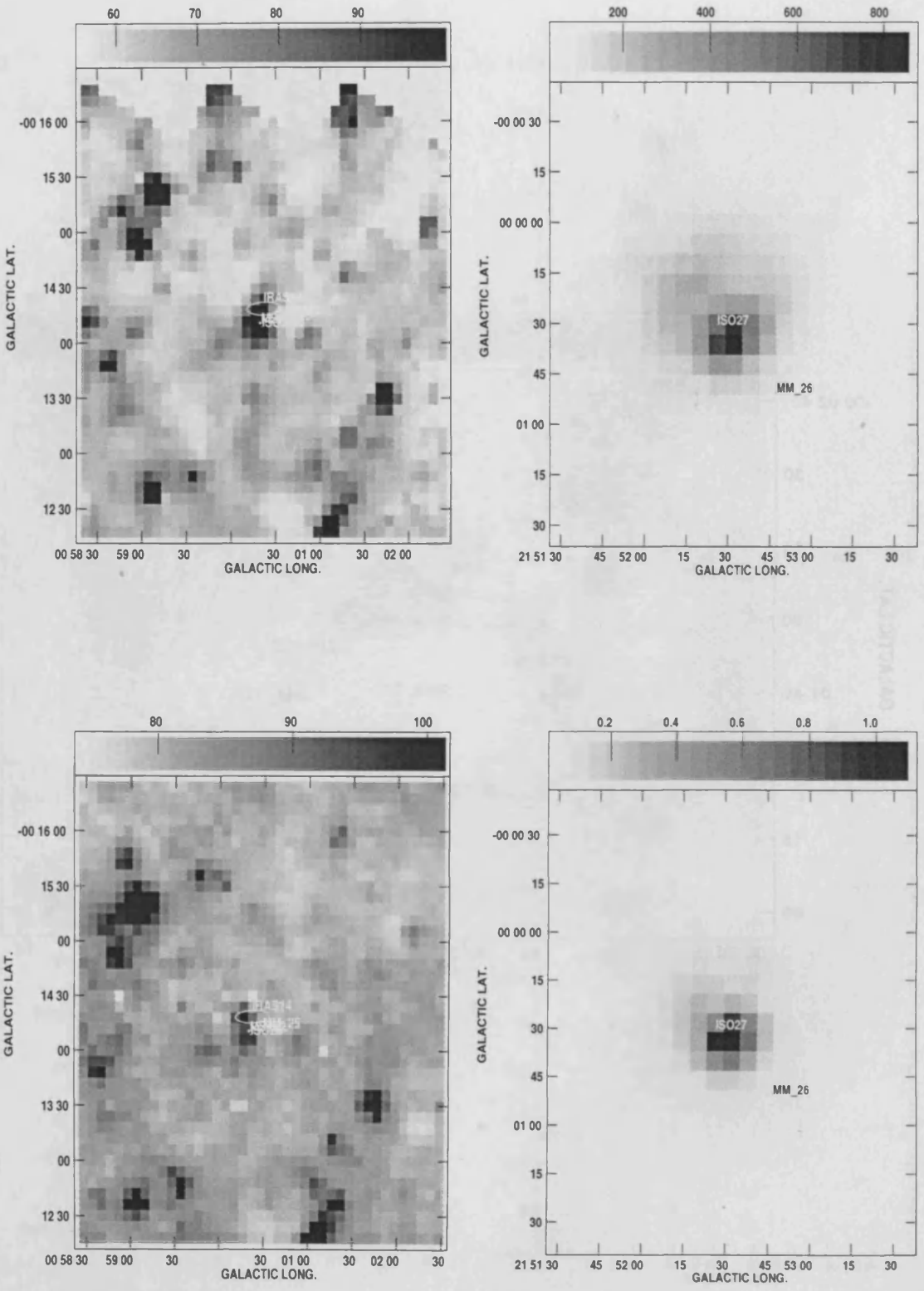

Figure 5.12: ISO images associated with methanol maser 25 (left) and 26 (right).

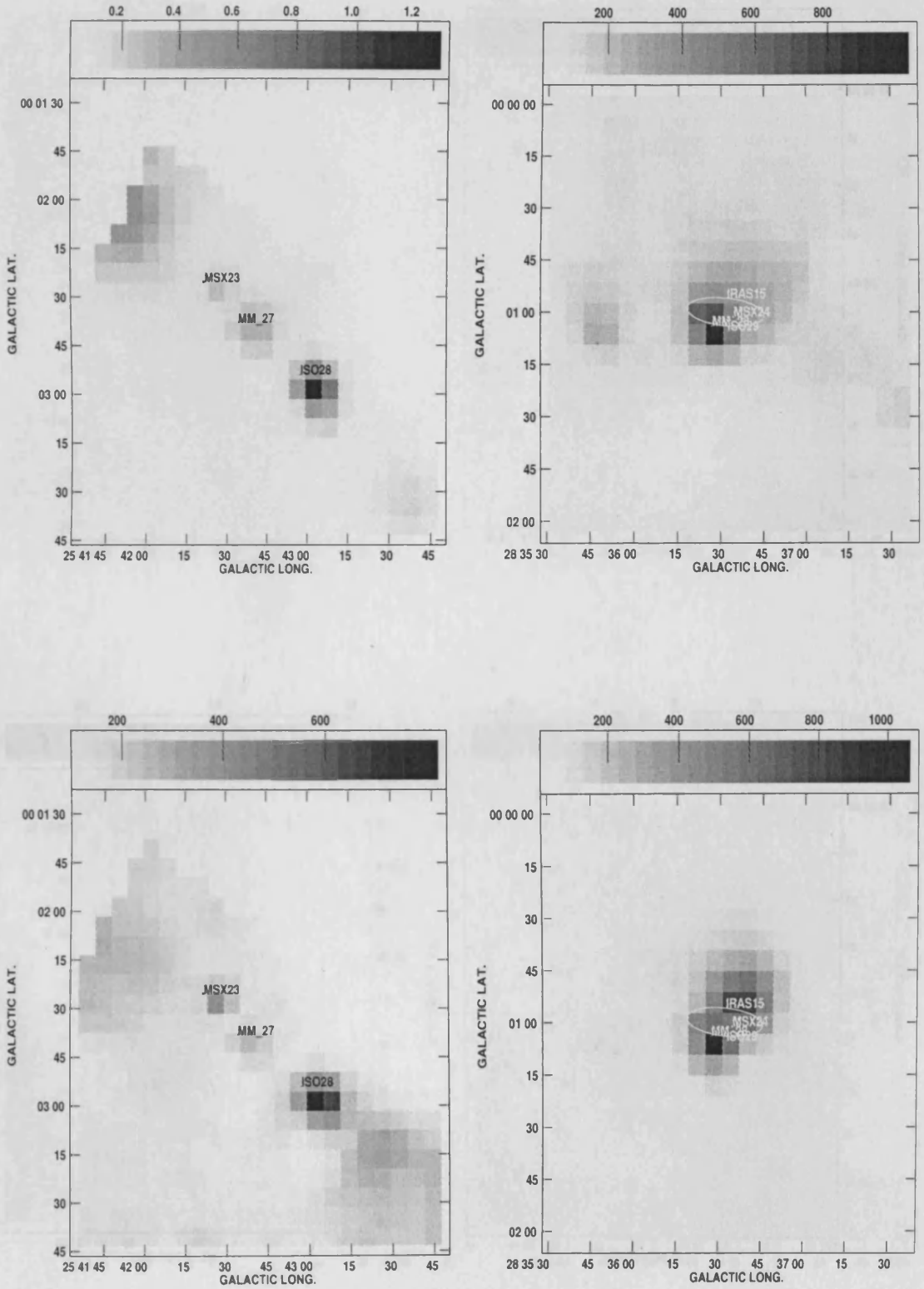

Figure 5.13: ISO images associated with methanol maser 27 (left) and 28 (right).

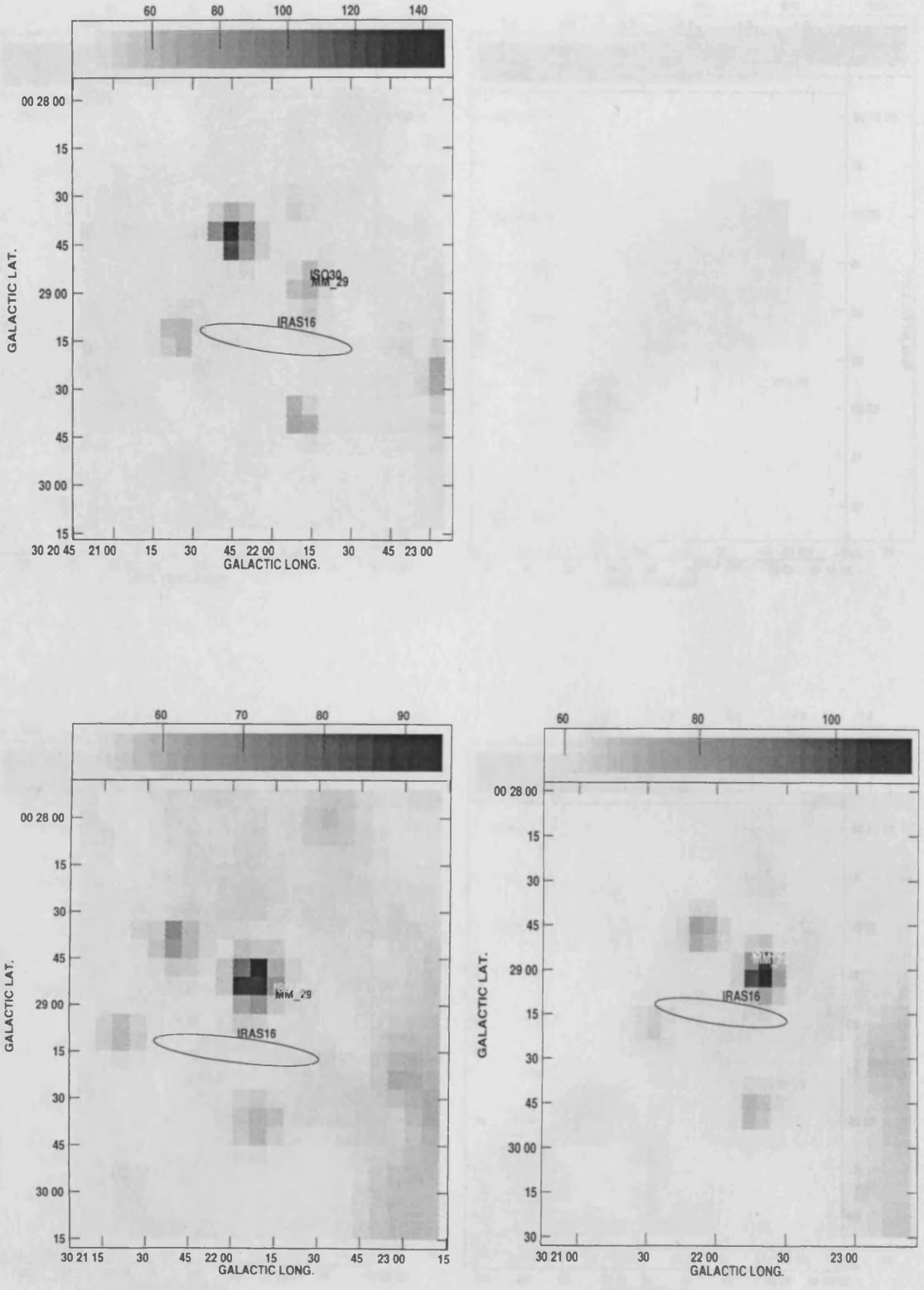

Figure 5.14: ISO images associated with methanol maser 29

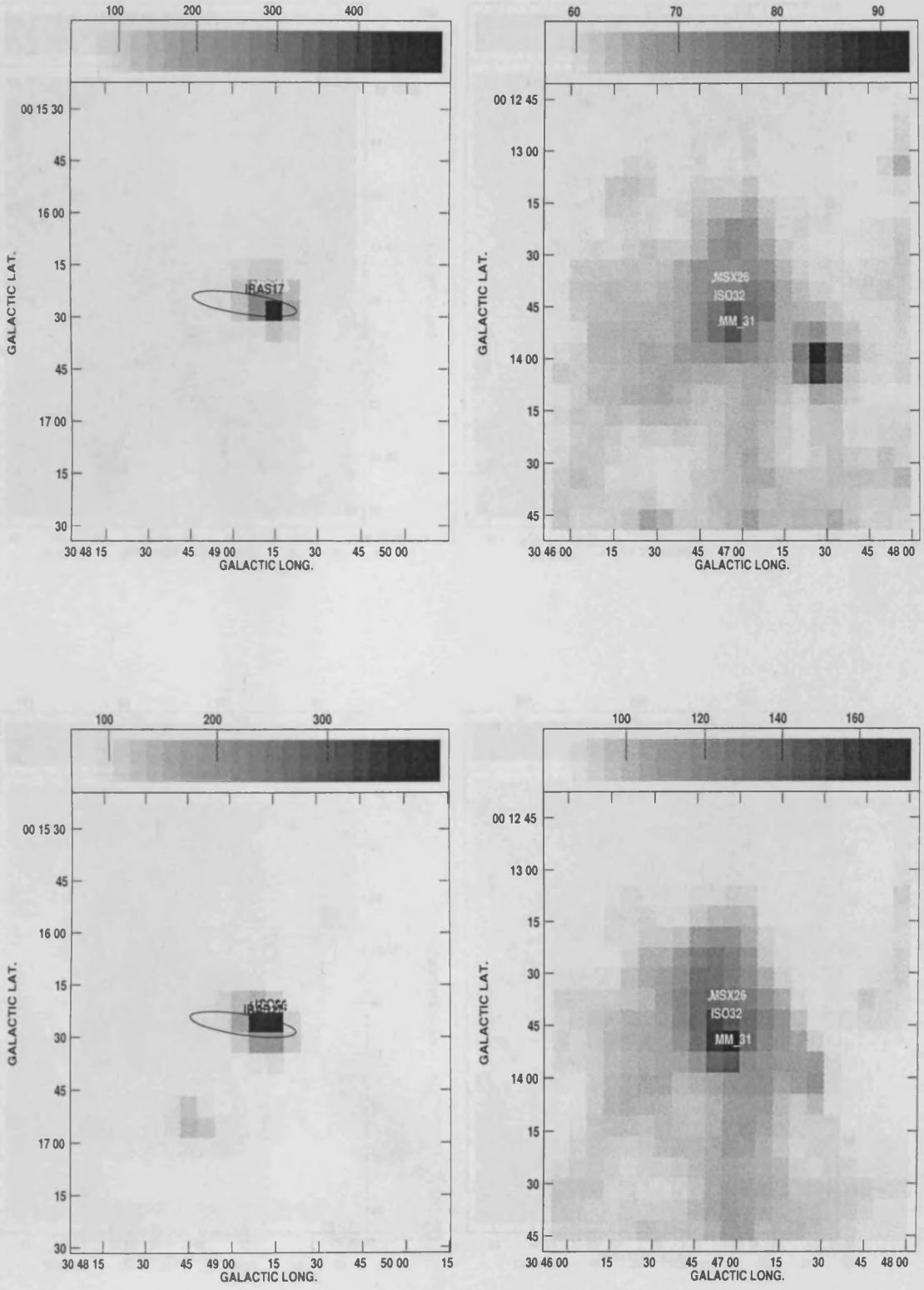

Figure 5.15: ISO images associated with methanol maser 30 (left) and 31 (right).

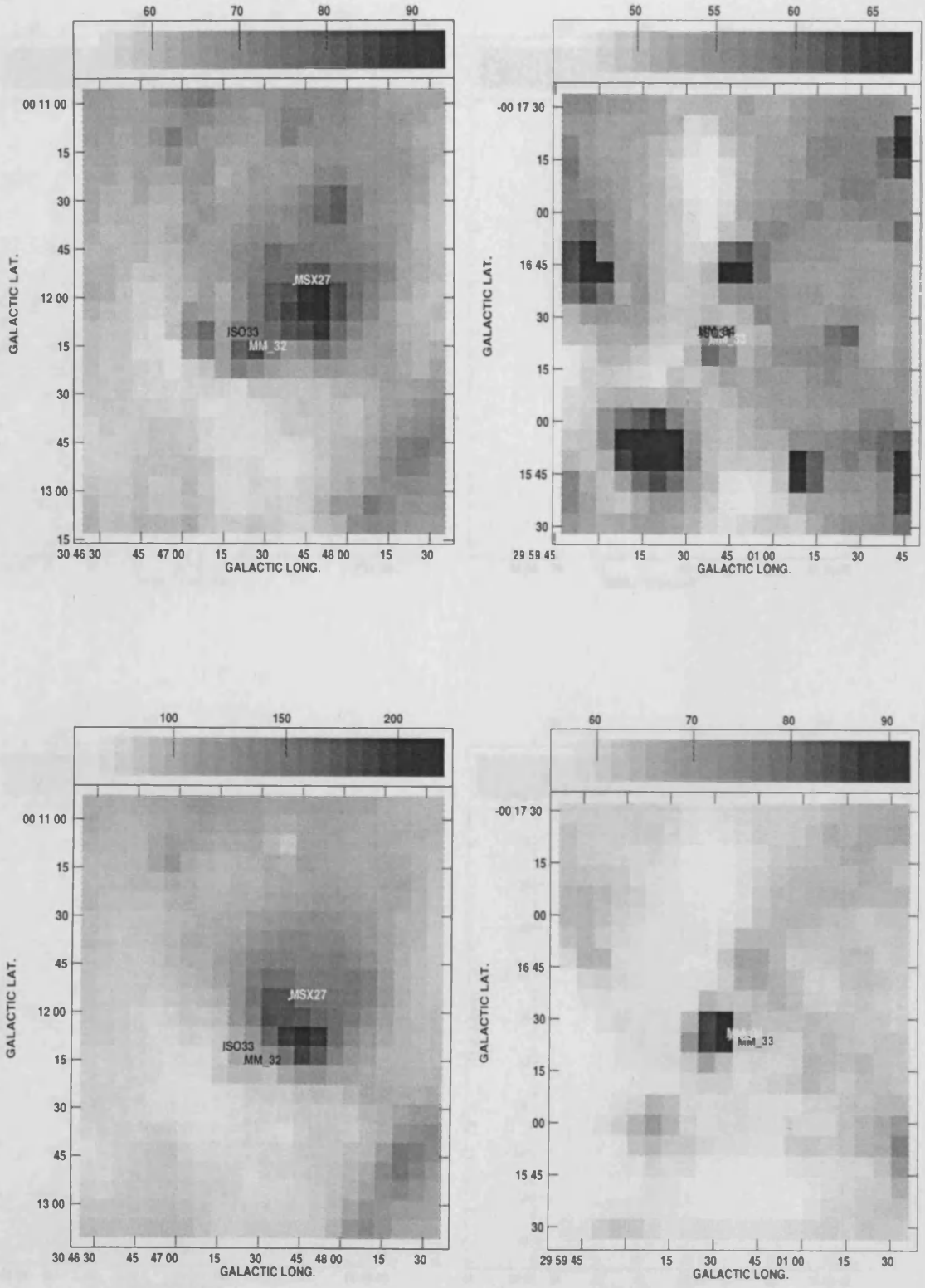

Figure 5.16: ISO images associated with methanol maser 32 (left) and 33 & 34 (right).

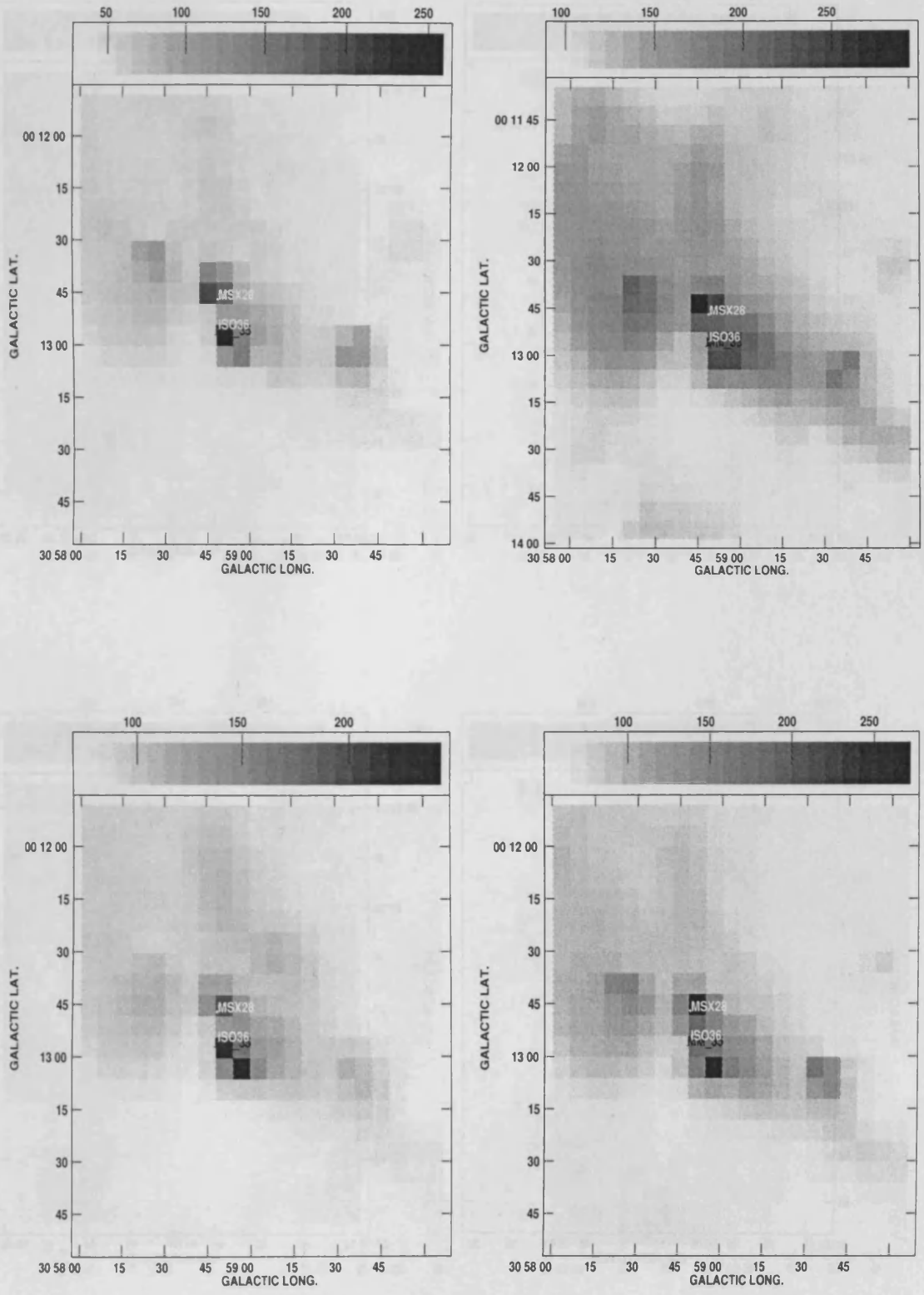

Figure 5.17: ISO images associated with methanol maser 35

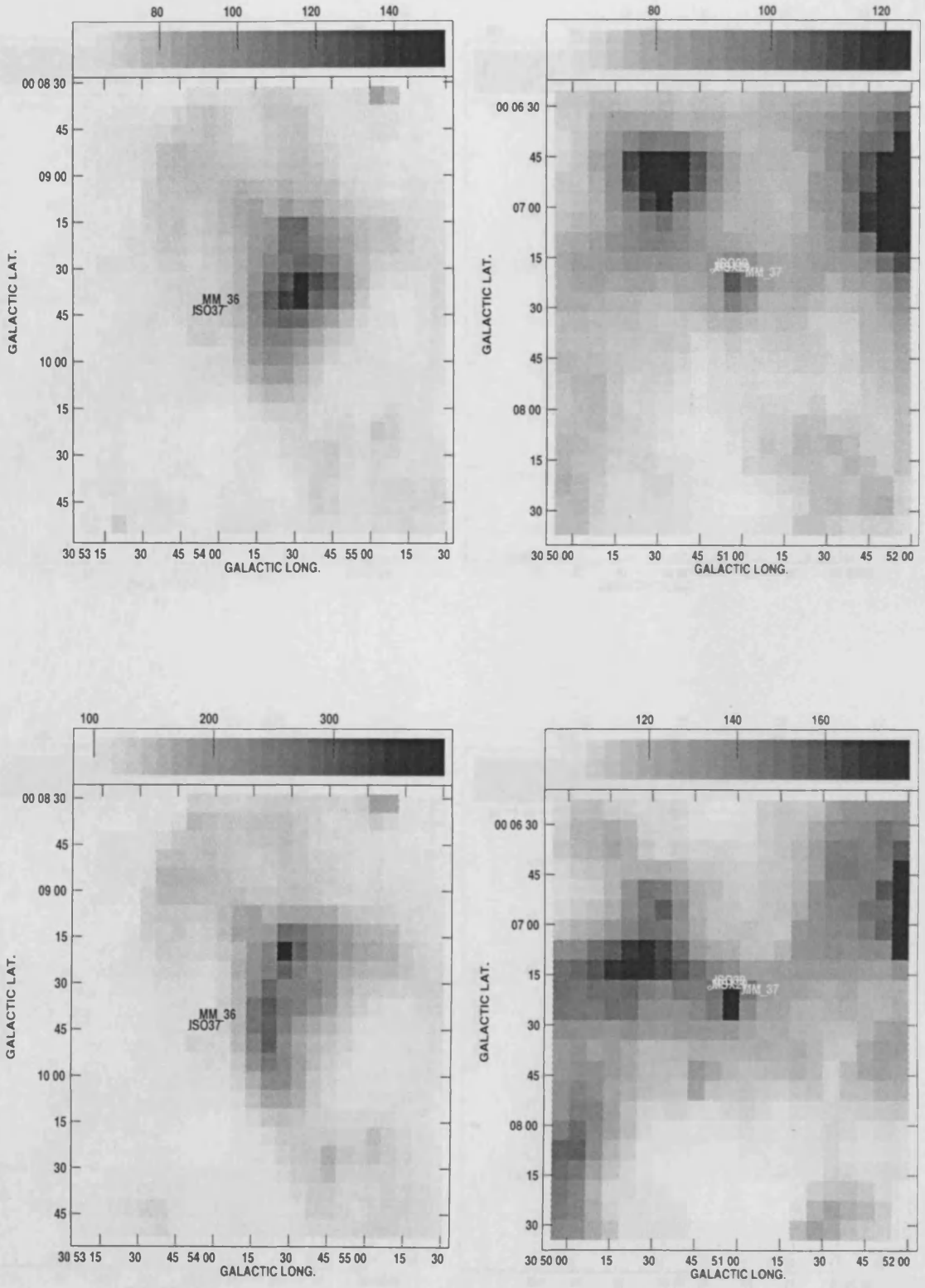

Figure 5.18: ISO images associated with methanol maser 36 (left) and 37 (right).

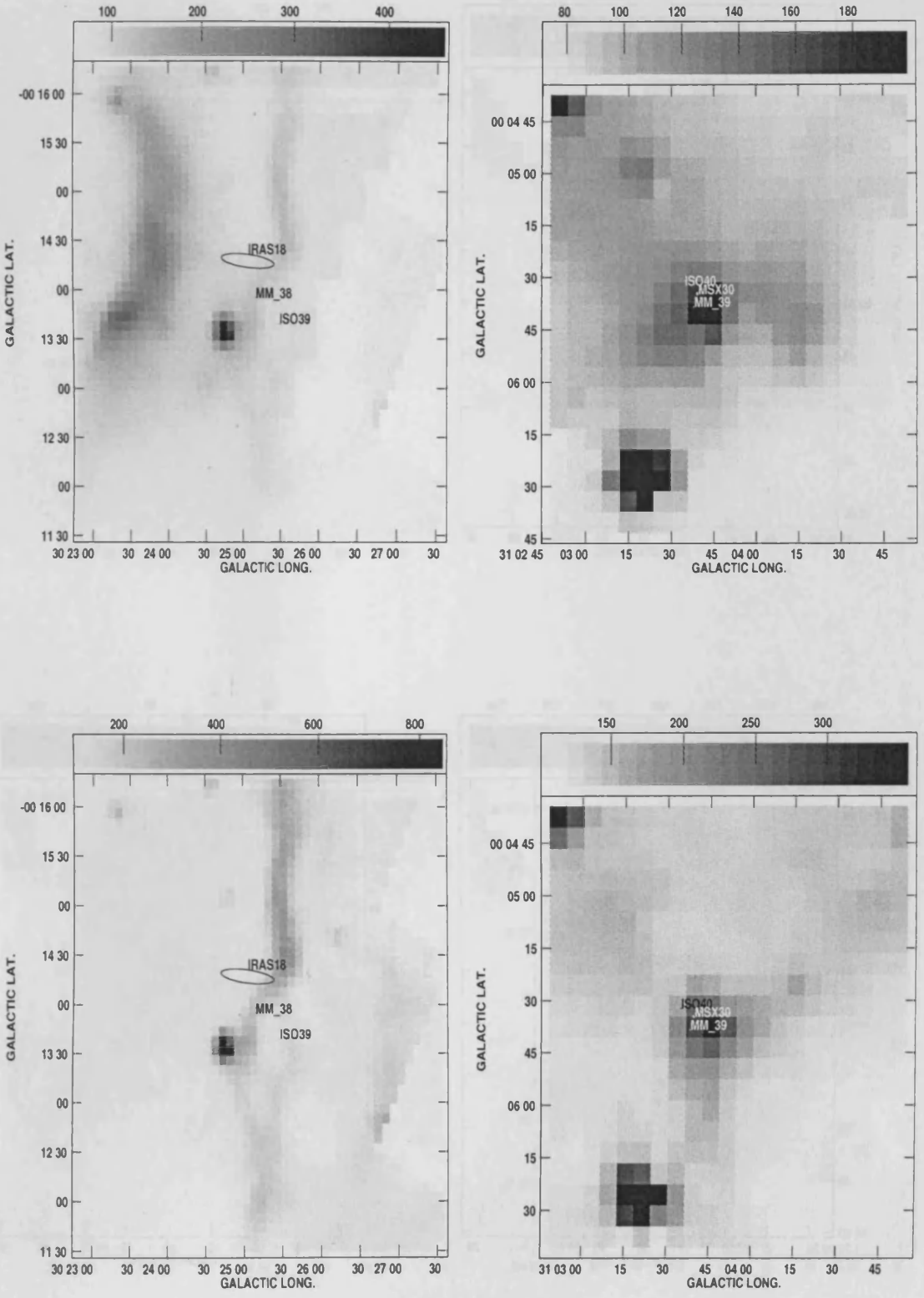

Figure 5.19: ISO images associated with methanol maser 38 (left) and 39 (right).

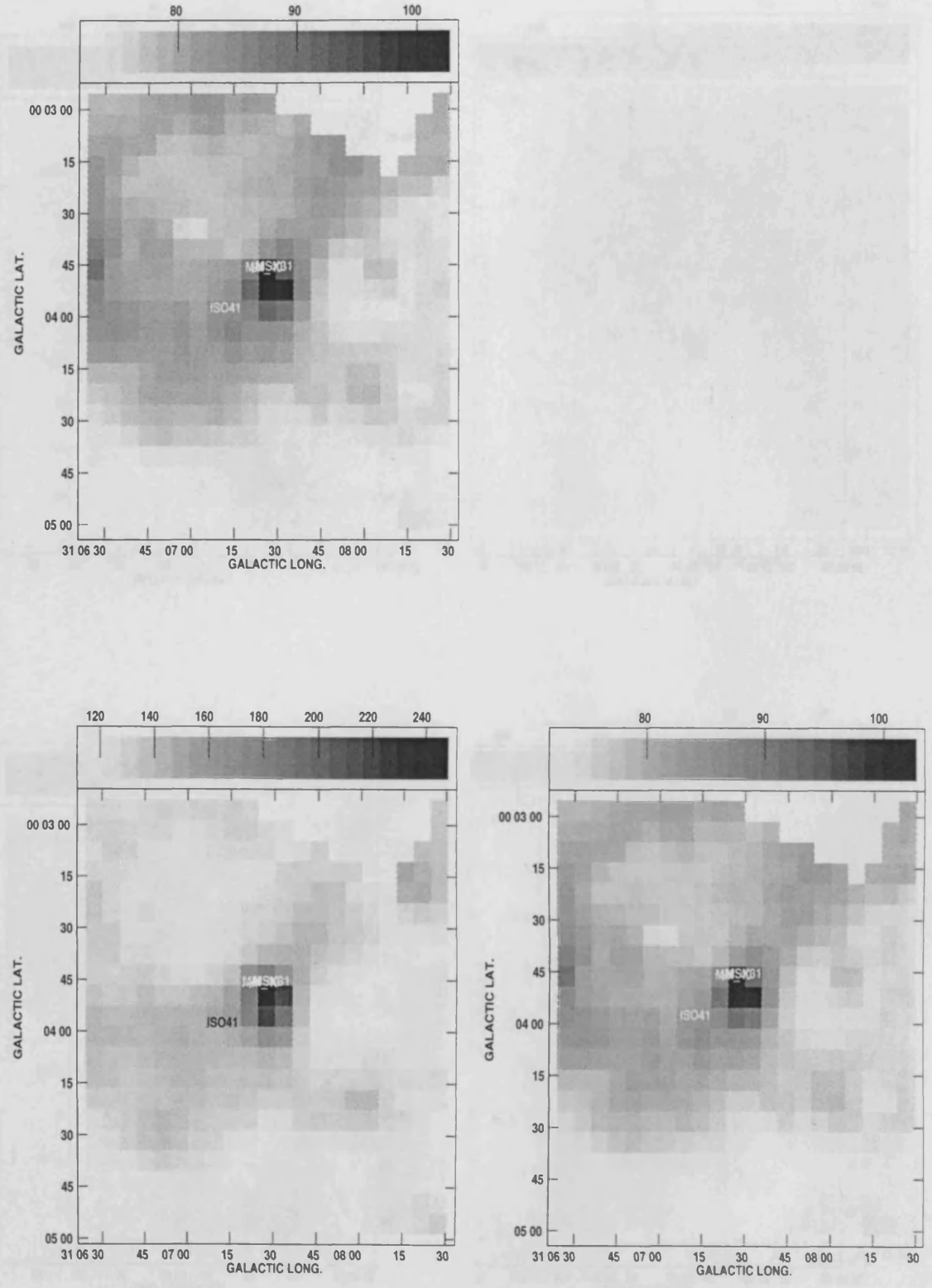

Figure 5.20: ISO images associated with methanol maser 40

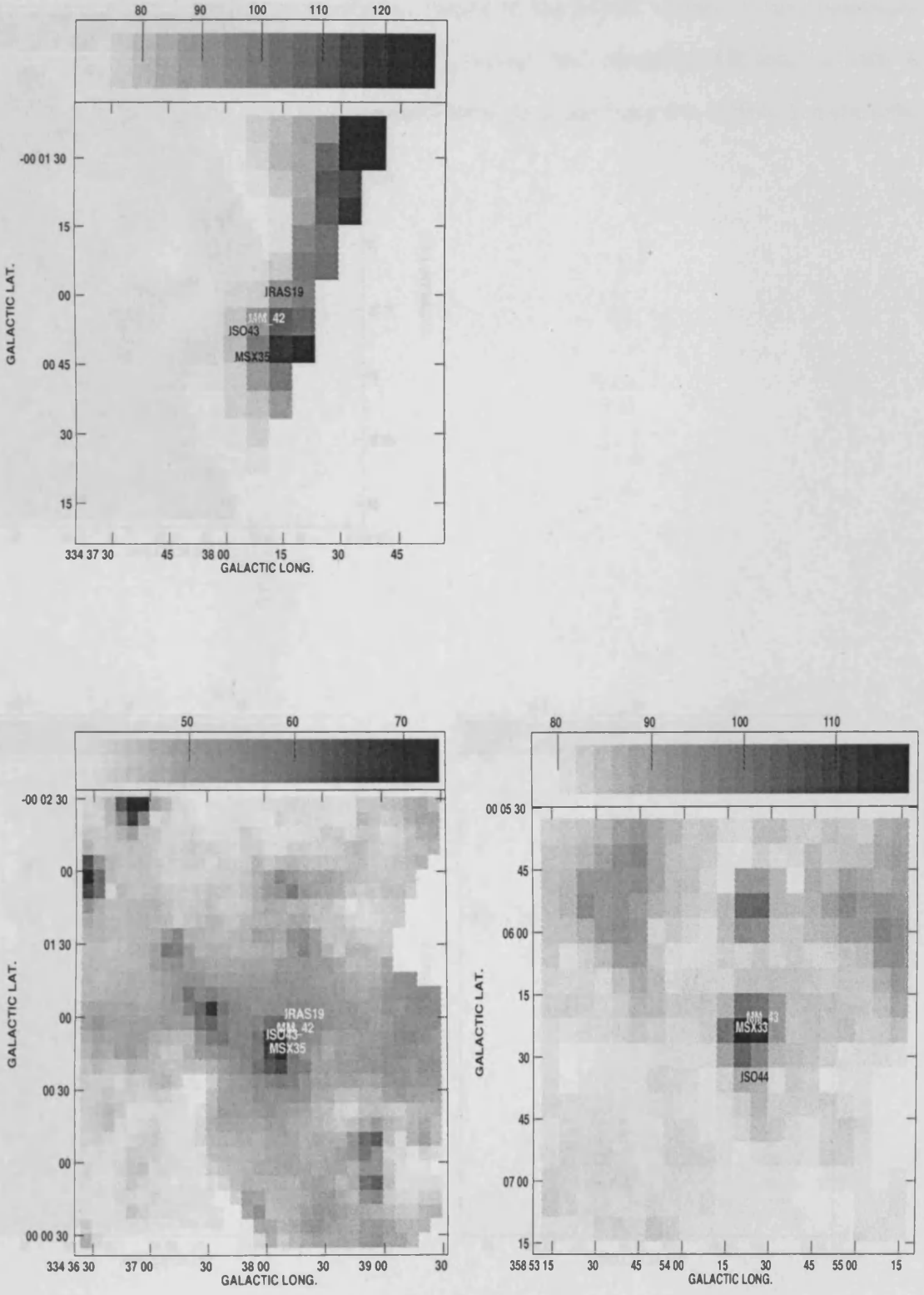

Figure 5.21: ISO images associated with methanol maser 42 (left) and 43 (right).

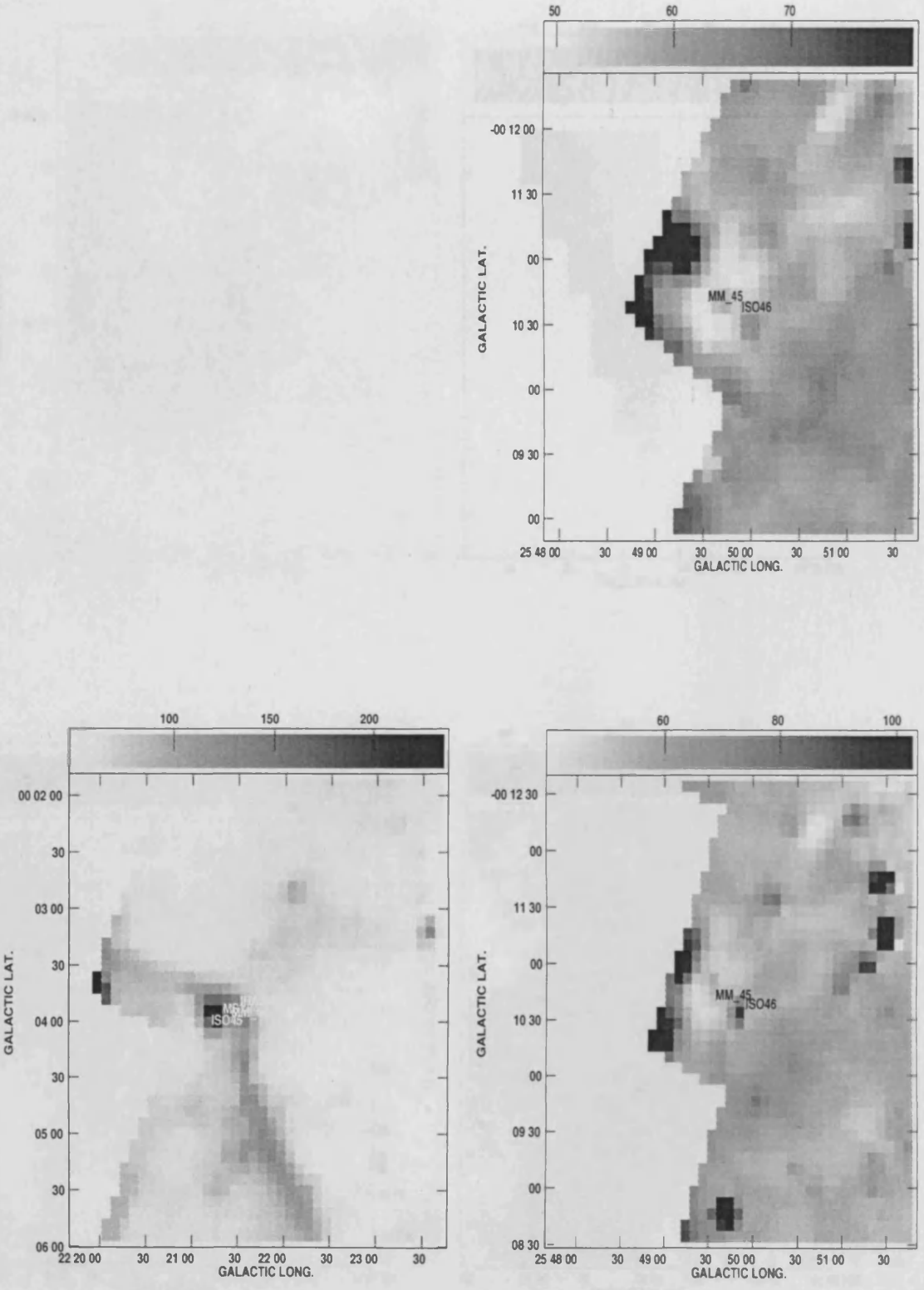

Figure 5.22: ISO images associated with methanol maser 44 (left) and 45 (right).

5.5 Summary

In this chapter I have presented the results of the MMB survey. I have compared the maser detections with the ISOGAL survey, and identified IR sources with 45 of the masers. In the next chapter I analyse and compare the different data sets.

Chapter 6

Discussion and Data Analysis

6.1 SEDs

SEDs were constructed from the MSX, DENIS and ISO data and are displayed in Figures 6.1 to 6.6. Log-log least squares fits were made to the data to measure the gradient of the data, thus enabling α to be determined, where α is the spectral index (see below).

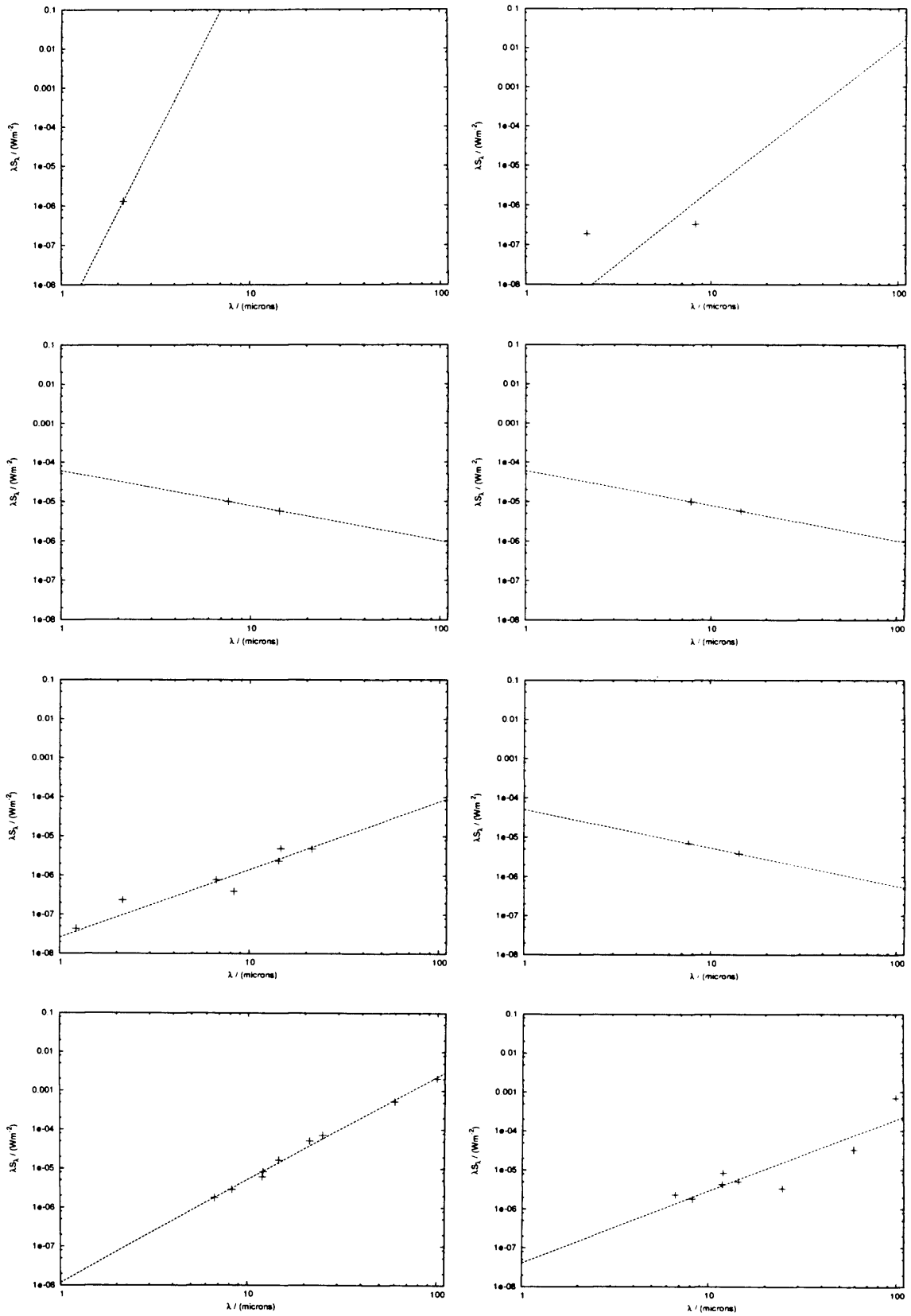

Figure 6.1: SEDs for IR sources associated with methanol masers 1 (bottom left) to 8 (top right)

6.2 Distance Measurement and Correction

Data of the observed methanol masers contains velocity information which has had Doppler correction applied to it as part of the observing process. The velocities are corrected to the local standard of rest (LSR) kinematic frame, which is based on the average velocity of the stars in our solar neighbourhood. This is currently accepted to be 16.5 kms^{-1} towards l = 53°, b = 25° (Binney and Tremaine 1987).

Because we are observing masers that are in the Galactic Plane, and we assume that they are moving in circular orbits, the observed line of sight velocities are related to the angular velocity by geometry, as follows.

It is possible to derive a relation between the radial velocity v_r and the angular velocity ω(R) of the maser:

$$v_r = R_0(\omega(R) - \omega_0(R_0))sinlcosb \tag{6.1}$$

in which R_0 is the distance of the Sun to the Galactic centre, $\omega_0(R_0)$ is the angular velocity at the position of the Sun. Because the angular velocity of the masers is determined by the rotation of the Galaxy it is possible to work out the distance of the masers from the centre of the Galaxy, and thereby from us, if the rotation curve of the Galaxy is known.

The rotation curve of the Galaxy has been measured several times, most recently by Brand and Blitz (1993), who used a sample of HII regions, reflection nebulae and their associated molecular clouds to calculate the velocity field of the Galaxy. They found a best fit to the rotation curve to have the form:

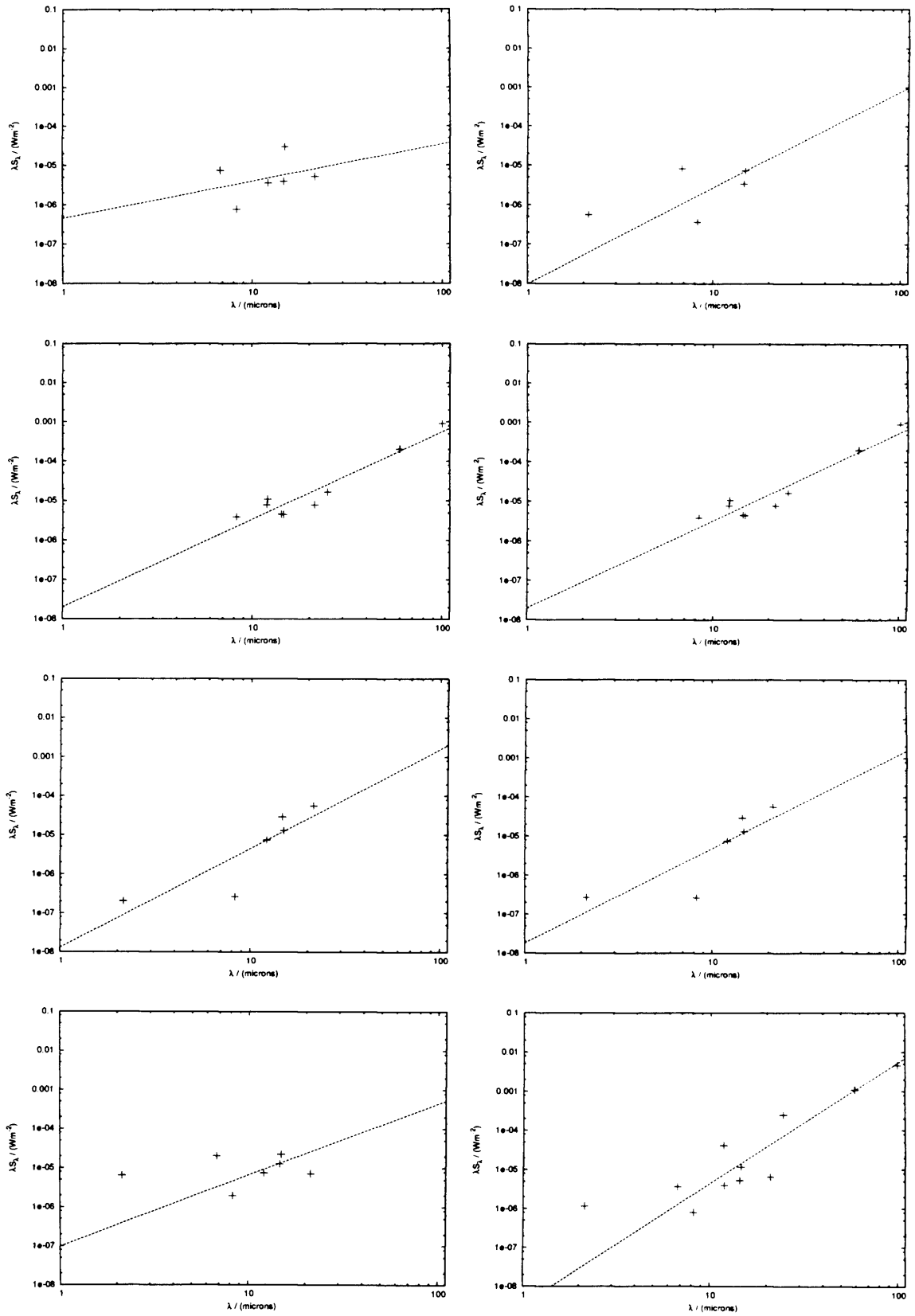

Figure 6.2: SEDs for IR sources associated with methanol masers 9 (bottom left) to 16 (top right)

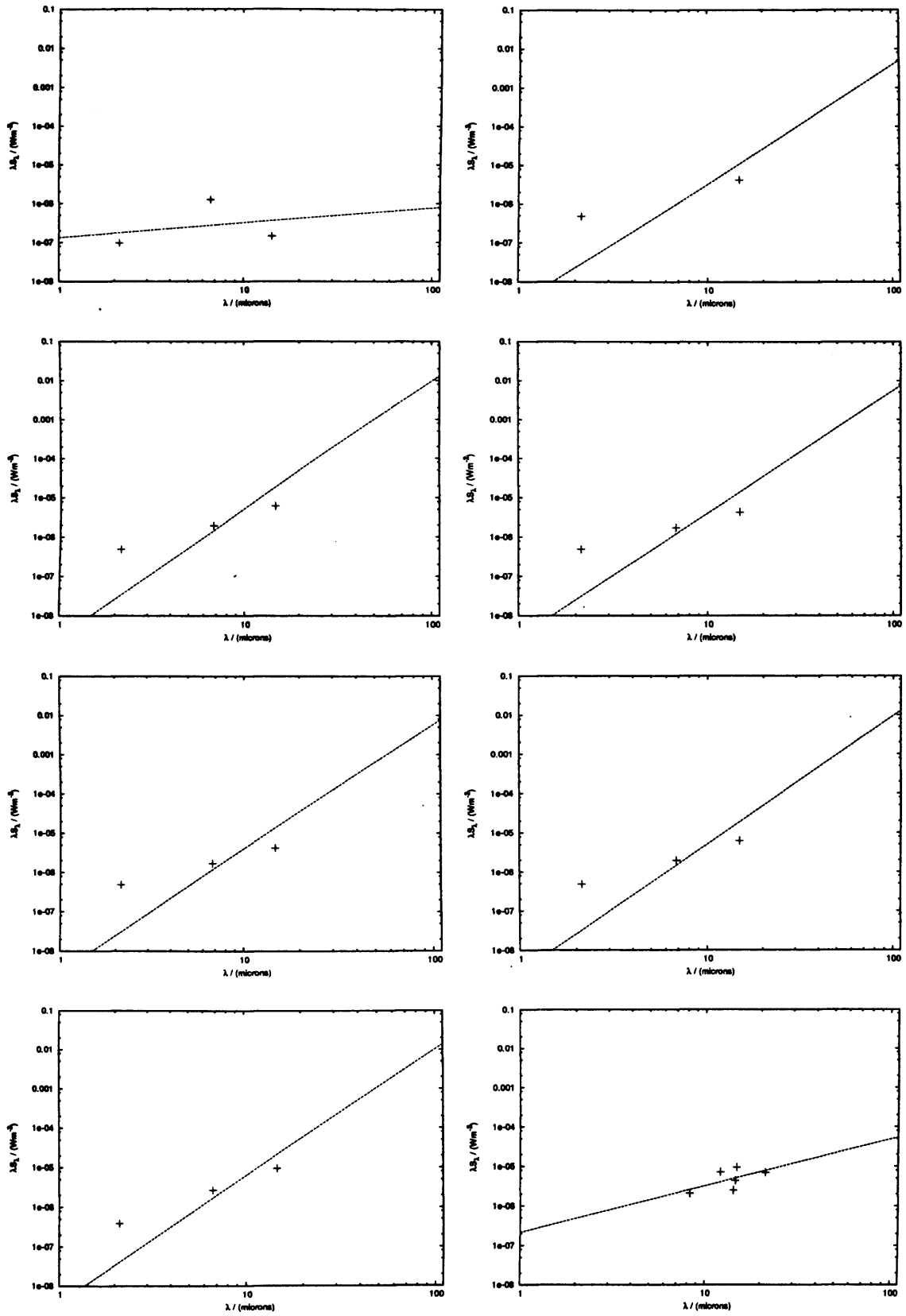

Figure 6.3: SEDs for IR sources associated with methanol masers 17 (bottom left) to 24 (top right)

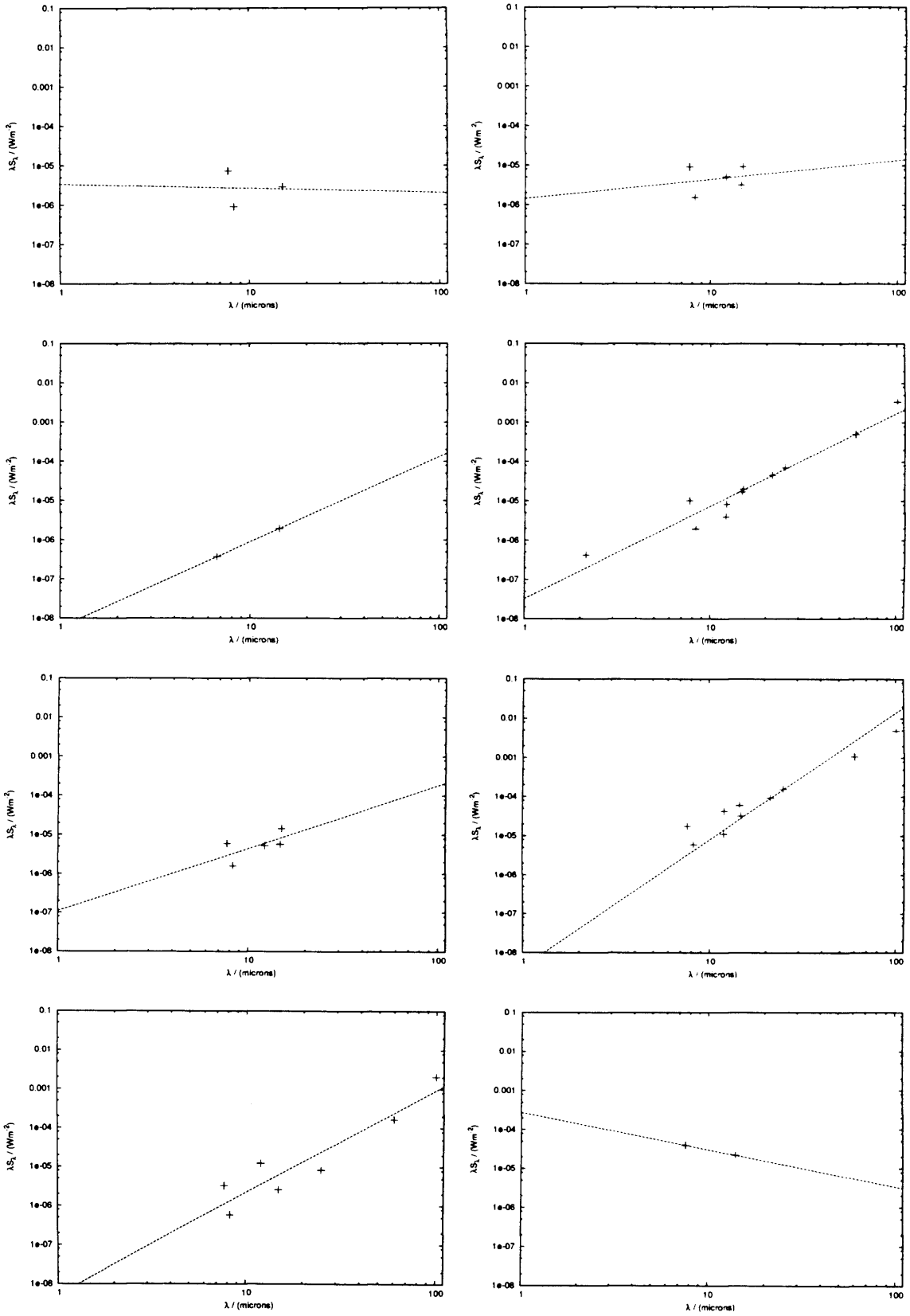

Figure 6.4: SEDs for IR sources associated with methanol masers 25 (bottom left) to 32 (top right)

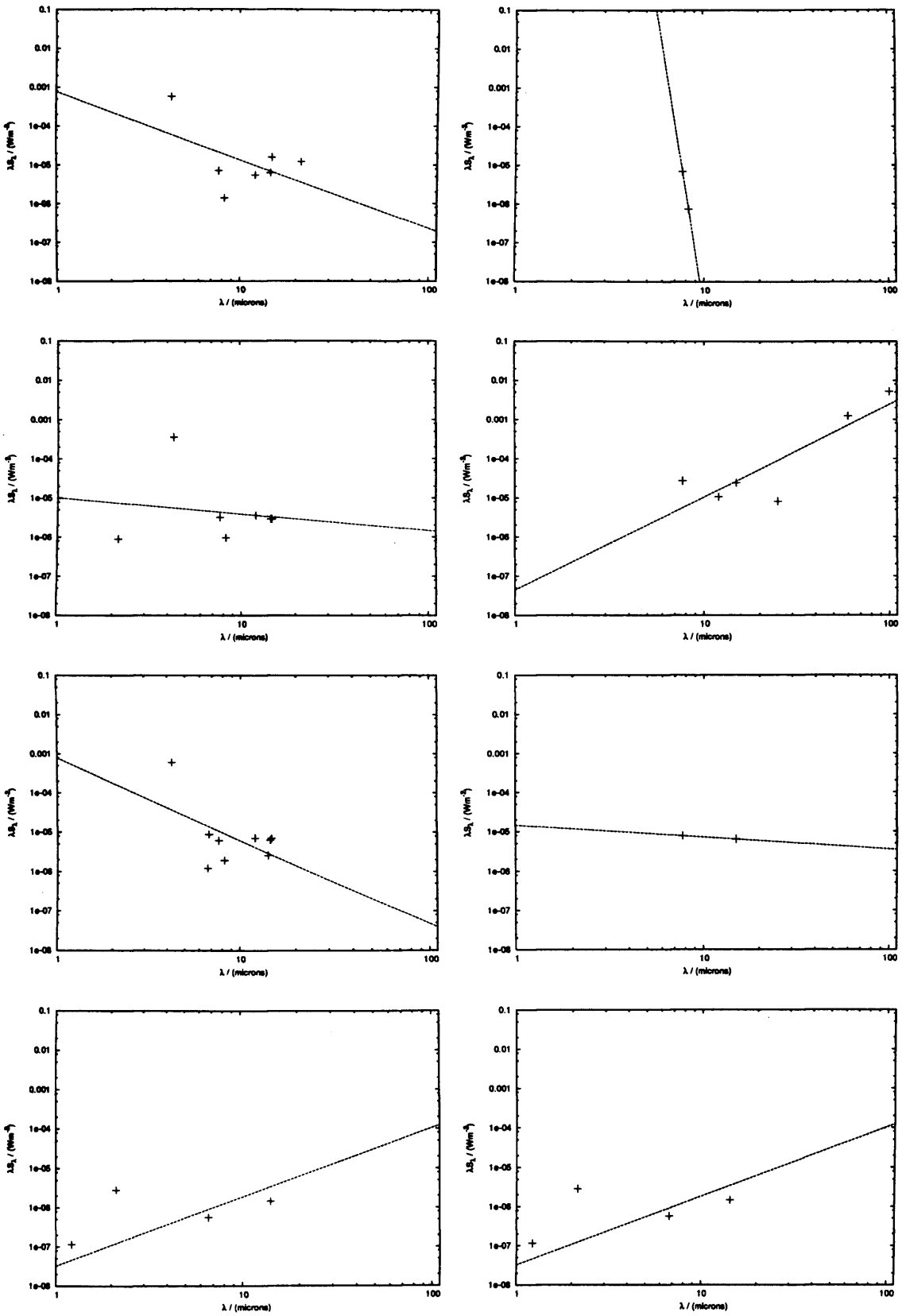

Figure 6.5: SEDs for IR sources associated with methanol masers 33 (bottom left) to 40 (top right)

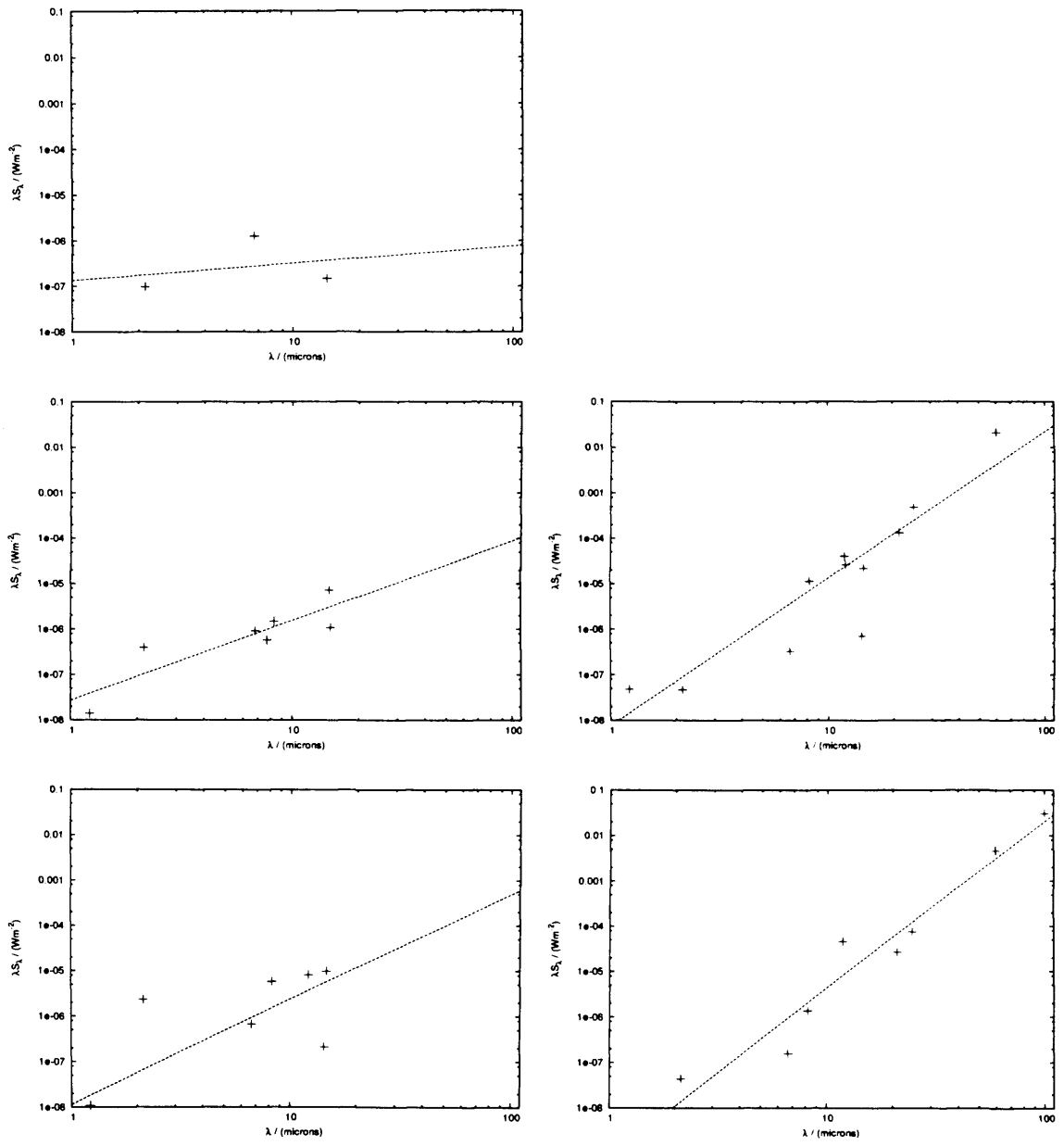

Figure 6.6: SEDs for IR sources associated with methanol masers 41 (bottom left) to 45 (top right)

$$\frac{\omega}{\omega_0} = a_1 \frac{R}{R_0}^{a_2-1} + a_3 \tag{6.2}$$

where a_1=1.00767, a_2=0.0394 and a_3=0.00712. Equation 6.2 can be used to find R, the Galactocentric distance of the object, the distance to the centre of the Galaxy. This distance can be used to find the Heliocentric distance of the maser by the following relation:

$$R = (D^2 cos^2(b) + R_0^2 - 2R_0 d cos(b) cos(l))^{1/2}. \tag{6.3}$$

Two distances are found after solving this quadratic equation which are commonly known as "near" and "far" Heliocentric distances. Table 5.1 contains the Galactocentric and Heliocentric distances of all 57 methanol masers which were in an ISOGAL field.

At the moment, because there is no obvious way to determine whether the near or far Heliocentric distances should be used, both distances are being used for the following corrections. Following a purely statistical approach, it is to be assumed that the flux of the methanol maser is linked to its distance to us, the further away it is, the less bright it is. Plotting the flux of the maser against its near and far distances, it could be concluded that the far distances give a tighter relation. To correct for distance the 10 kpc equivalent flux was calculated for each maser using both near and far distances. Table 6.1 contains these as well as spectral index information (see below).

Methanol Maser Number	Methanol Maser Flux Jy	Methanol Maser Far Corrected Flux Jy	Methanol Maser Near Corrected Flux Jy	Spectral Index α	Number of points	Confidence R^2
MM 01	2.6	2.2	0.8	4.12	9	0.97
MM 02	0.9	0.9	0.2	3.96	8	0.82
MM 03	2.4	3.9	0.1	1.96	8	0.81
MM 04	0.8	1.3	0.1	-2.14	2	1.00
MM 05	18.8	26.5	2.8	-1.49	2	1.00
MM 06	3.5	5.6	0.3	-2.26	2	1.00
MM 07	3.2	8.0	0.0	1.47	4	0.44
MM 08	7.2	5.9	4.5	3.19	6	0.79
MM 09	4.5	4.7	2.1	2.15	8	0.66
MM 10	15.6	23.5	3.5	3.88	13	0.89
MM 11	4.2	3.2	2.8	2.33	7	0.31
MM 12	26.8	20.8	18.0	2.08	7	0.25
MM 13	9.0	8.9	4.5	3.46	9	0.94
MM 14	1.6	1.6	0.8	3.46	9	0.94
MM 15	10.0	20.8	0.7	1.94	6	0.35
MM 16	0.7	0.5	0.5	1.90	6	0.48
MM 17	2.7	2.2	1.7	1.33	4	0.32
MM 18	8.1	12.6	1.6	1.03	6	0.04
MM 19	33.7	25.8	22.9	1.70	5	0.46
MM 20	4.4	3.4	3.0	0.03	3	0.00
MM 21	0.4	0.3	0.3	2.25	2	1.00
MM 22	0.4	0.3	0.3	-0.56	2	1.00
MM 23	4.5	3.5	3.0	0.03	3	0.00
MM 24	2.1	1.6	1.4	1.70	2	1.00
MM 25	14.0	38.4	0.0	4.50	8	0.79
MM 26	5.5	10.6	0.2	-1.88	2	1.00
MM 27	386.0	356.8	125.5	1.34	5	0.19
MM 28	1.8	1.2	0.8	4.22	11	0.98
MM 29	0.7	1.2	0.0	18.25	2	1.00
MM 30	5.0	3.0	2.4	3.58	11	0.91
MM 31	27.0	34.2	3.0	-1.19	3	0.24
MM 32	29.0	24.7	8.4	1.01	5	0.05
MM 33	1.5	0.8	0.8	1.05	5	0.21
MM 34	1.1	0.7	0.5	1.05	5	0.21
MM 35	1.0	0.7	0.4	-0.14	6	0.00
MM 36	79.0	48.5	36.0	-0.01	2	1.00
MM 37	0.6	0.9	0.0	0.04	7	0.00
MM 38	13.0	8.1	5.9	4.85	6	0.88
MM 39	24.0	42.2	0.4	-0.08	7	0.00
MM 40	1.1	1.4	0.1	-1.31	3	0.48
MM 41	1.5	2.3	0.1	2.31	8	0.62
MM 42	36.4	61.0	2.1	3.69	10	0.97
MM 43	1.7	1.7	0.8	1.75	7	0.77
MM 44	10.0	11.3	2.6	3.23	13	0.88
MM 45	65.0	62.3	19.8	0.38	3	0.07

Table 6.1: Flux density, spectral index and data confidence information for the 45 methanol masers associated with ISOGAL sources. Distance corrected fluxes for the methanol masers are the 10 kpc equivalent flux calculated using either the near or far Heliocentric distances.

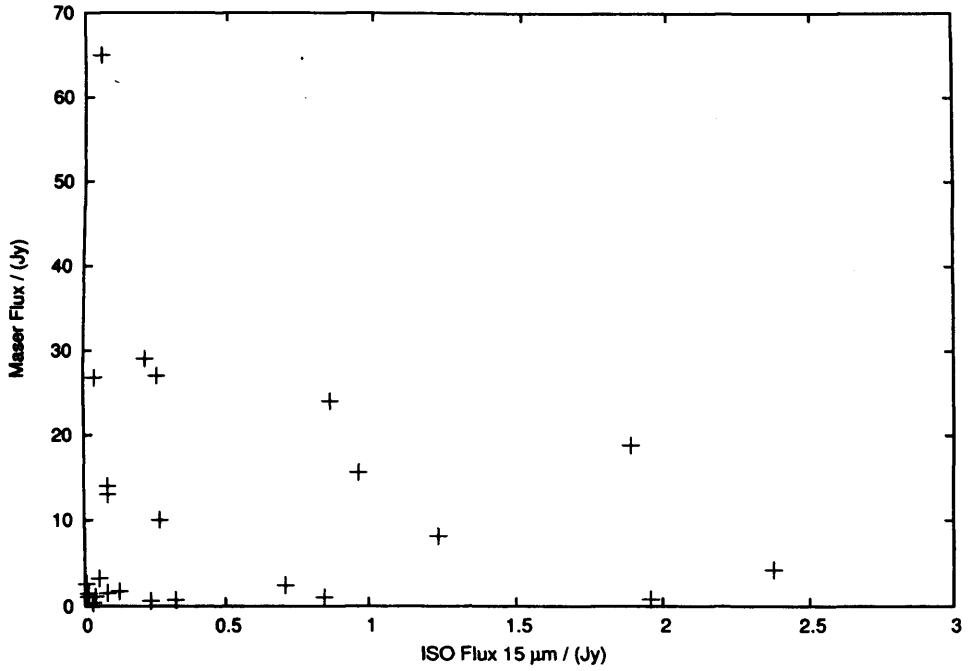

Figure 6.7: Methanol maser flux plotted against 15 μm ISO flux.

6.3 Correlations Between Radio and Infrared Parameters

The relation between the methanol maser fluxes and various infrared parameters were tested. Figure 6.7 shows a plot of methanol maser flux against 15 μm ISO flux. No correlation can be seen. In fact, the only parameters which showed a correlation were methanol maser flux and the spectral index of the source associated with it (see below).

Table 6.1 contains the maser fluxes and spectral indices for each of the 45 masers which are associated with an ISOGAL source. The table also contains information on the number of data points that are used to make up the SED and the confidence in the fit, R^2.

6.4 Correlation Between Methanol Maser Flux and Spectral Index

The spectral index α of an IR source was defined by Lada (1987):

$$\alpha = \frac{dlog(\lambda F_\lambda)}{dlog(\lambda)}$$

The spectral index was calculated by making a best fit to the data points which make up the SEDs (figures 6.1 to 6.6) and calculating the gradient of this.

Table 6.1 contains the spectral index and associated confidence data for the 45 methanol masers associated with an ISOGAL source. It also shows the number of data points that were used to calculate the spectral index. Obviously, the confidence in calculating a fit between two points is 1. It was decided to drop any spectral indices that had been calculated with less than 3 data points as these were deemed unreliable.

Figure 6.8 holds plots of methanol maser flux versus the spectral index of the source associated with it for different distance corrections. The top panel has the raw methanol maser flux, the middle panel has the 10 kpc equivalent flux calculated from the near distance, and the bottom panel the same correction using the far distance. The error bars are calculated using the confidence in the best fit to the SED. A loose correlation can be seen between the flux of the maser and the spectral index of the source associated with it. This correlation appears tighter when the maser flux has been corrected using the far distances.

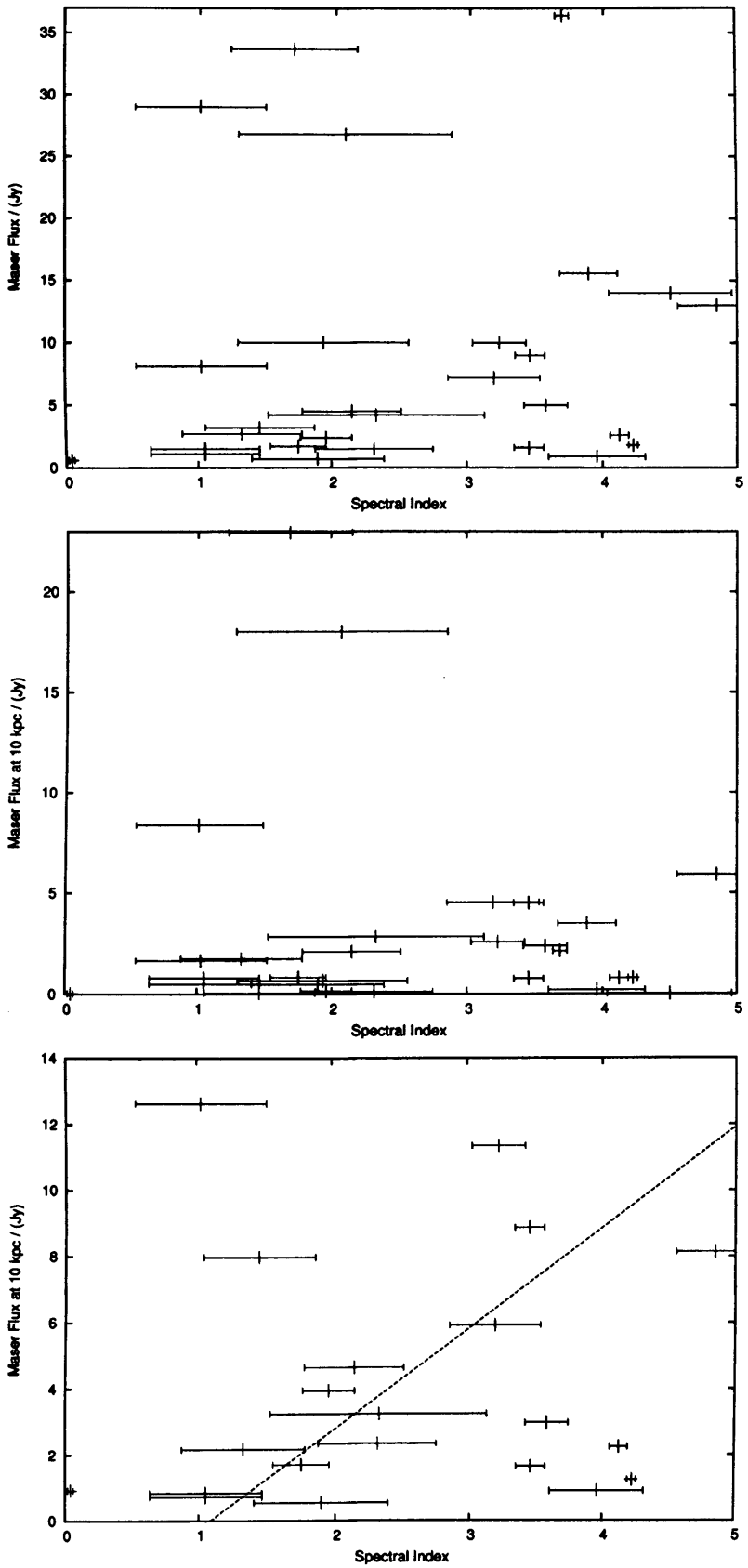

Figure 6.8: Methanol maser flux versus the spectral index of the source associated with it for different distance corrections. The top panel has the raw methanol maser flux, the middle panel has the 10 kpc equivalent flux calculated from the near distance, and the bottom panel the same correction using the far distance.

The correlation between the methanol maser flux and the spectral index can be explained by considering the effect of dust on the SED of a black body source. Figure 6.9 contains three plots of three theoretical SEDs that have been adapted from Lada (1987), the y-axis is $\log(\lambda F_\lambda)$ and the x-axis is λ in μm. In the following, we will be going backwards from a "final" main sequence star, to a protostar.

The lower panel holds the theoretical SED of a final star that is very near to or on the main sequence. The SEDs plotted in Figures 6.1 to 6.6 hold data between typically 2 μm and 100 μm, a strong negative gradient in these would indicate a source of this type. The middle panel shows the theoretical SED of the stage before that of a "final" star. It shows the effect of dust by the reddening of the SED, and represents a central radiating object which is enshrouded by dust. The top panel displays the theoretical SED of a source that is deeply embedded in a dusty core. The dust dominates above 10 μm and the mass of dust present influences the spectral index of the source. The more dust that is being heated and then radiating in the far infrared, the greater the spectral index will be.

There are some SEDs with negative gradients, for example the sources associated with methanol masers 4, 5 and 6 (Figure 6.1). But all of these (not just methanol masers 4-6) can be explained by their not having enough data points to produce meaningful SEDs. There are some SEDs that have a flattish gradient, for example the source associated with methanol maser 39 (Figure 6.5). Looking at these, the poor linear fit to the data becomes apparent. This could be because of source confusion and will be discussed in the following section.

The vast majority of sources show a positive gradient and a good fit to the data. As explained above, the greater the spectral index, the more dust mass there is likely to be shrouding the protostellar source. This is indicative of a younger

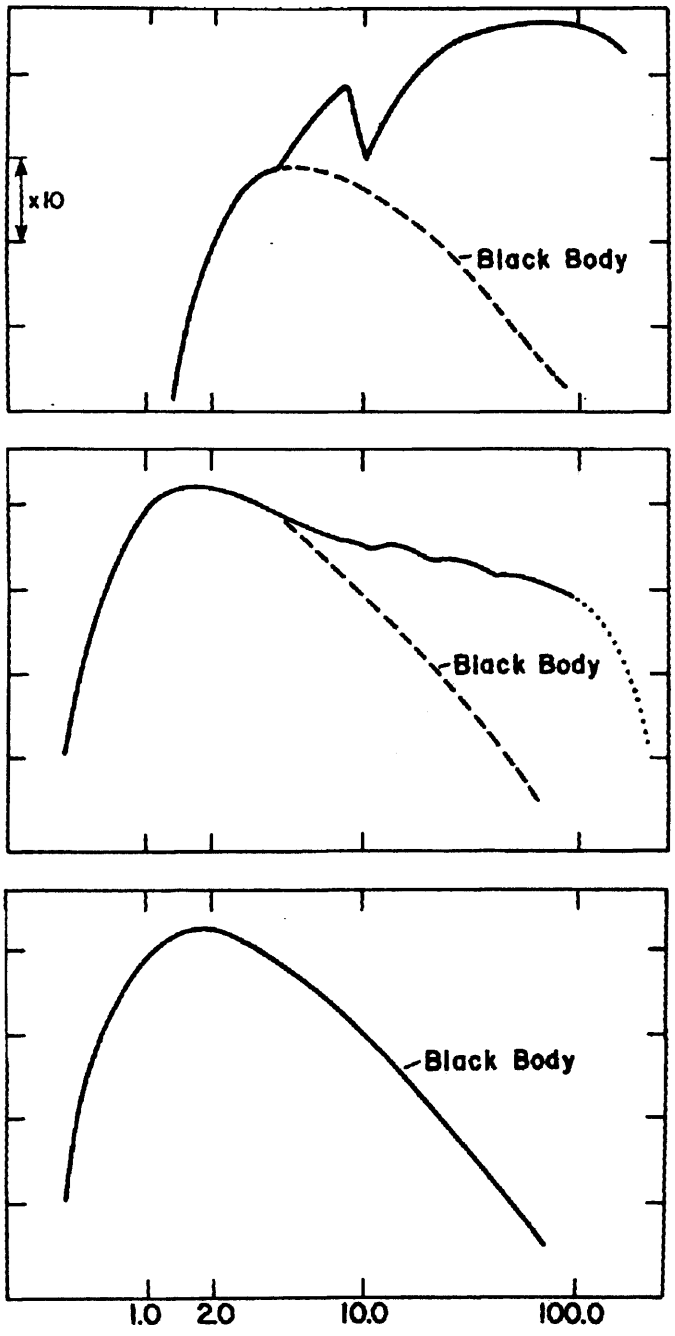

Figure 6.9: The effect of dust on SEDs. Top panel: deeply enshrouded source with strong 10 μm silicate absorption. Middle panel: source with less dust. Bottom panel: Final main sequence star.

source, the younger it is the more dust there is. The correlation between maser flux and spectral index is then really a correlation between maser flux and the mass of dust present, as well as a correlation between maser flux and the age of the source. The correlation therefore implies that the more flux associated with a maser the more dust there is present and the younger the protostellar source.

6.4.1 Correlation Between Methanol Maser Flux and Dust Mass

Previous 6.67 GHz methanol maser studies have targeted UCHII regions by colour selecting IRAS sources according to the Wood and Churchwell criteria (1989a) (Schutte et al. 1993, Van der Walt 1995, Walsh et al. 1997, Walsh et al. 1998). These were largely unsuccessful with detection rates between 9% and 38%. In their later study, Walsh et al. found that the size of the UCHII regions associated with 6.7 GHz methanol masers were generally smaller than those without, suggesting that these UCHII regions are possibly younger. This led them to suggest an evolutionary scenario where 6.7 GHz methanol masers begin masing at a stage of the protostellar evolution before a UCHII region has developed. That is, 6.7 GHz methanol masers are generally associated with younger high mass protostellar objects (HMPOs).

The implication from the data in this chapter that methanol maser strength is correlated with the age of the source is consistent with this scenario. As outlined in Chapter 1, specific conditions of the molecular material are required before maser action begins. The most relevant is the density of the gas which is usually between 10^6 and 10^9 cm^{-3}. It is likely that the maser flux is proportional to the gas density. As the gas is dispersed by the wind from the HMPO, the maser flux

will likely decrease. Hence the older the HMPO, the fainter the maser.

Alternatively it is possible that the enormous luminosity that is associated with a new born massive star and is responsible for the ionisation of the HI which surrounds it, creating the HII that leads to a UCHII region, will alter the chemistry of all the gas that surrounds it. In this instance the abundance of methanol, which is crucial for masing action, may be depleted, thereby reducing the amount of microwave radiation amplified, and hence, lowering the measured flux of the maser.

6.5 Hot Core Candidates

In the preceding section several interesting SEDs were presented as the correlation between methanol maser flux and dust mass (or HMPO age) was presented. These were mostly the SEDs which had poor linear fits and flat gradients, for example methanol masers 35, 37, 39 and to some extent methanol masers 33 and 34 (Figure 6.5). It was suggested that the poor linear best fit arose because of source confusion. This was because of the presence of near infrared fluxes that were equal to, or elevated above their far infrared counterparts. It is possible that this is due to the source being a hot core and at an evolutionary stage before the development of a UCHII region.

G29.96-0.02 is a known hot core and has been observed in the near and mid IR (De Buizer, Osorio, & Calvet 2005) and the far IR (Maxia et al. 2001). Figure 6.10 shows the SED presented in De Buizer, Osorio, & Calvet 2005. The data points are from various observations which are quoted in the figure, the solid line is a fit to the data. This fit is optimised by altering the radius and mass of the molecular envelope, as well as the luminosity of the internal heating source. The

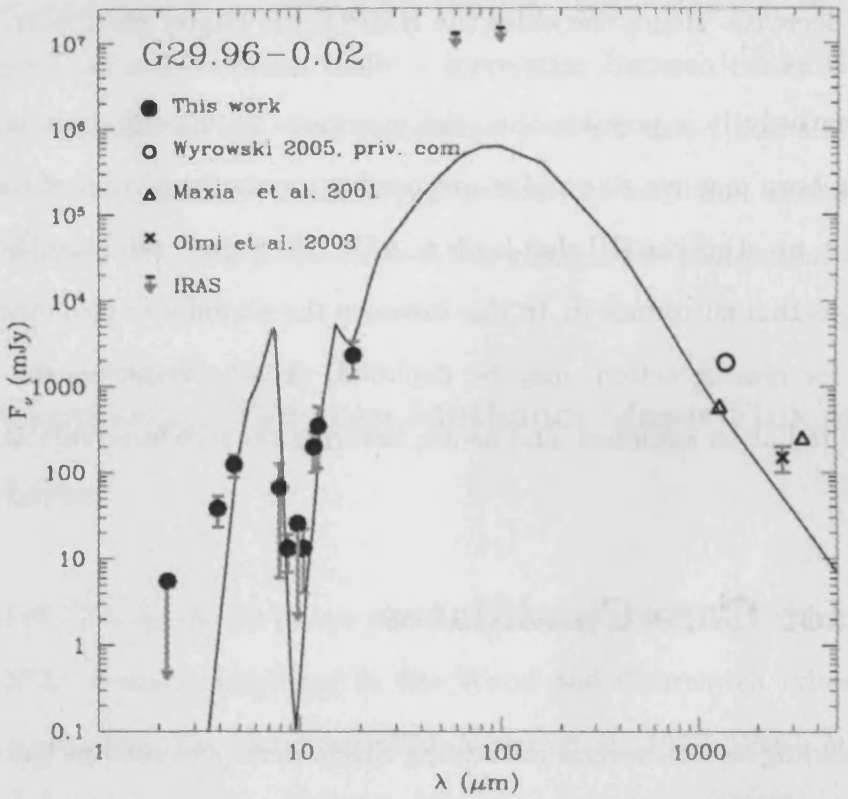

Figure 6.10: Known hot core G29.96-0.02. Presented in De Buizer, Osorio & Calvet 2005. For explanation of the line fit see text.

model that is used to produce this fit is not relevant to this thesis, the plot is merely presented to demonstrate some of the features that are hinted at in some of the SEDs in figures 6.1 to 6.6.

This plot is interesting for several reasons. Firstly, it shows the effect of what is considered an internal heating source in the near IR, with a peak between 2 and 8 μm. It also clearly shows the 10μm silicate absorption feature which is followed by a steep rise up to about 100 μm. This can be partially seen in the SEDs presented in this section, which unfortunately suffer from not having the same wavelength coverage. It's only possible to see, when looking at methanol maser 39 (Figure 6.5) for example, that the spectrum is heading down towards 10 μm and rises again towards the far IR. Looking at the SEDs in this way it becomes clear that there

are several points on the plot which do not fit this explanation and that these points are associated with the 7 μm and 14 μm measurements taken from the ISO images. These all appear to be underestimations and suggest that the method for measuring the fluxes from the ISO images needs to be reconsidered.

In most cases however, this does not appear to have too much of a bearing on the line that is fitted and hence spectral index that is calculated. This is because the SEDs have been treated in a simple manner, reducing them to linear fits. This is because we were interested in the relationship between the dust and the methanol maser and hence in the slope between $\sim$10μm and $\sim$100μm.

6.6 Summary

In this chapter SEDs have been presented which were produced by combining fluxes from the DENIS, MSX and IRAS point source catalogues with measurements taken from ISO archive data. Best fits were made to these data and distance corrections were applied to the fluxes of the methanol masers. The distances were calculated using the methanol maser velocity information and the galactic rotation curve calculated by Brand and Blitz (1993). The spectral indices (α) of the infrared sources were calculated and a correlation between α and the flux of the associated maser was found. This was explained in terms of the mass of dust present and age of the source. Comparisons were made between the SEDs presented and known hot molecular core (HMC) G29.96-0.02. Interesting features were noted which implied that the method of calculating the fluxes from the ISO data had possibly underestimated some. It was concluded that these underestimations did not affect the correlation between methanol maser flux and mass of dust in the associated

IR source.

Chapter 7

Summary and Conclusions

I began this thesis by showing the limits of the current understanding of the formation of massive stars. This is mostly because of the radiation pressure that such objects exert on the infalling material, rendering stars larger than 8 $M_{\odot}$ theoretically problematic, and stars larger than 50 $M_{\odot}$ theoretically impossible. It was shown that there are several alternative approaches to solving this problem and that they all require observations of the earliest stages of the process of massive star formation. A tracer of this stage, the 6.67 GHz methanol maser, was then discussed. This methanol maser is uniquely associated with the phenomena of the earliest stages of high mass star formation, high mass protostellar objects (HMPOs), hot molecular starless cores (HMSCs), and compact HII regions. An unbiased survey for these masers in the plane of the Galaxy, the Methanol Maser Multibeam (MMB) Survey, was then outlined.. It was noted that for the subsequent exploration of these regions highly spatially resolved mid and far infrared observations are required, since this is where the emission from HMSCs and HMPOs peak. During chapters 2 to 4 I discussed a new far infrared camera, THUMPER,

which was designed and built in Cardiff. THUMPER was capable of making such observations of HMSCs and HMPOs.

THUMPER was described in chapter 2 and explanations were given for its wavelength of operation and various components. Atmospheric transmission restricted the wavelength of operation and various design constraints, which arose because of THUMPER's intended role as a common user instrument on the JCMT, limited the choice of cryogenic system and hence detector system. The figures of merit which are used to describe the performance of such systems were described.

Because THUMPER had been designed and built before my arrival in Cardiff, chapter 3 set out the status of the project as I arrived. It explained the confusion that had arisen over THUMPER's performance and my work which demonstrated that previous measurements of the system had been inaccurate. It was concluded that THUMPER was not performing to full specification, but that there was nothing that could be done without rebuilding the detector block.

Chapter 4 outlined the observations that were carried out with THUMPER on the JCMT. Weather constraints limited the amount of available observing time. Nevertheless we successfully characterised the atmospheric transmission at 200 μm on Mauna Kea. In addition we made the first 200 μm ground based astronomical images when we mapped Jupiter and Mars. Upgrades to the JCMT prevented further observing runs.

The results of the MMB survey were presented in chapter 5. I compared the maser detections with the ISOGAL survey (Schuller et al. 2003), and identified IR sources with 45 of the masers. It was originally anticipated that THUMPER would be used to perform follow up observations of some of these regions. This

was not possible which is why the follow up work used the ISOGAL data archive. Other data from the DENIS (Epchtein et al. 1994), MSX (Egan et al. 1999) and IRAS (Beichman et al. 1998) point source catalogues were used to complete the infrared coverage and construct the SEDs, which were presented in chapter 6.

In the final chapter best fits were made to the SEDs while the methanol maser fluxes had distance corrections applied. The distances were calculated using the methanol maser velocity information and the galactic rotation curve calculated by Brand and Blitz (1993). The spectral indices (α) of the infrared sources were calculated and a correlation between α and the flux of the associated maser was found. This was explained in terms of the mass of dust present and age of the source. Comparisons were made between the SEDs presented and known hot molecular core (HMC) G29.96-0.02. Interesting features were noted which implied that the method of calculating the fluxes from the ISO data had possibly underestimated some. It was concluded that these underestimations did not affect the observed correlation between methanol maser flux and mass of dust in the associated IR source, nor did it affect our conclusions.

This thesis has presented a unique way of targeting the earliest stages of massive star formation and a unique instrument capable of the highly spatially resolved far infrared observations which are required to separate the different theories of how high mass stars form.

Bibliography

Ade P. A. R., 2003, Private Communication

Anderson G. P., Clough S. A., Kneizys F. X., Chetwynd J. H., Shettle E. P., AFGL atmospheric constituent profiles (0.120km), 1986, AFGL-TR-0208 Environemental Research papers

Araujo H. M., Walker R. J., Rinehart S. A., Griffin M. J., Ade P. A. R., Assessment of the 200μm Atmospheric Window for Ground-based Astronomy, 2001, International Journal of Infrared Millimetre Waves, 22

Archibald E. N., Jenness T., Holland W. S., Coulson I. M., Jessop N. E., Stevens J. A., Robson E. I., Tilanus R. P. J., Duncan W. D., Lightfoot J. F., On the atmospheric limitations of ground-based submillimetre astronomy using array receivers, 2002, MNRAS, 336, 1

Barnes D. G. et al., The Hi Parkes All Sky Survey: southern observations, calibration and robust imaging, 2001, MNRAS, 322, 486

Barrett A. H., Ho P., Martin R. N., Time variations and spectral structure of the methanol maser in Orion A, 1975, ApJ, 198, L119

Barrett A. H., Schwartz P. R., Waters J. W., Detection of Methyl Alcohol in Orion at a Wavelength of ~1 Centimeter, 1971, ApJ, 168, L101

Batrla W., Matthews H. E., Menten K. M., Walmsley C. M., Detection of strong methanol masers towards galactic H II regions, 1987, Nature, 326, 49

Batrla W., Menten K. M., Detection of a strong new maser line of methanol toward DR 21(OH), 1988, ApJ, 329, L117

Beichmann C. A., Helou G., Walker D. W., 1988, Infrared astronomical satellite (IRAS). Catalogs and atlases. NASA RP (Reference Publication), Washington: NASA, —c1988, edited by Beichmann, C.A.—e et al. (Vol.1); Helou, George—e (Vol.7); Walker, D.W.—e (Vol.7)

Benjamin R. A., Churchwell E., Babler B. L., Bania T. M., Clemens D. P., Cohen M., Dickey J. M., Indebetouw R., Jackson J. M., Kobulnicky H. A., Lazarian

A., Marston A. P., Mathis J. S., Meade M. R., Seager S., Stolovy S. R., Watson C., Whitney B. A., Wolff M. J., Wolfire M. G., GLIMPSE. I. An SIRTF Legacy Project to Map the Inner Galaxy, 2003, PASP, 115, 953

Binney J., Tremaine S., 1987, Galactic dynamics. Princeton, NJ, Princeton University Press, 1987, 747 p.

Bonnell I. A., Vine S. G., Bate M. R., Massive star formation: nurture, not nature, 2004, MNRAS, 349, 735

Brand J., Blitz L., The Velocity Field of the Outer Galaxy, 1993, A&A, 275, 67

Bratt P. R., 1977, in Semiconductors and Semimetals Vol. 12. Edited by Willardson, R.K. Beer, A.C. (1977).

Cesarsky C. J. et al., ISOCAM in flight., 1996, A&A, 315, L32

Chamberlin R. A., Bally J., The Observed Relationship between the South-Pole 225-GHz Atmospheric Opacity and the Water-Vapor Column Density, 1995, Internat. J.Infrared Millimeter Waves, 16, 907

Clegg P. E. et al., The ISO Long-Wavelength Spectrometer., 1996, A&A, 315, L38

Clough S. A., Kneizys F. X., Davies R. W., Line Shape and the Water Vapor Continuum, 1989, Atmos. Res., 23, 229

Cohen R. J. et al., 2007, in IAU Symposium, Vol. 237, Elmegreen B. G., Palous J., ed, IAU Symposium, p. 403

Condon J. J., Broderick J. J., Seielstad G. A., A 4.85 GHz sky survey. I - Maps covering delta between 0 and + 75 deg, 1989, AJ, 97, 1064

Cragg D. M., Johns K. P., Godfrey P. D., Brown R. D., Pumping the interstellar methanol masers, 1992, MNRAS, 259, 203

Crutcher R. M., Magnetic Fields in Molecular Clouds: Observations Confront Theory, 1999, ApJ, 520, 706

Dame T. M., Hartmann D., Thaddeus P., The Milky Way in Molecular Clouds: A New Complete CO Survey, 2001, ApJ, 547, 792

De Buizer J. M., Osorio M., Calvet N., Observations and Modeling of the 2-25 μm Emission from High-Mass Protostellar Object Candidates, 2005, ApJ, 635, 452

de Graauw T. et al., Observing with the ISO Short-Wavelength Spectrometer., 1996, A&A, 315, L49

Egan M. P., Price S. D., Moshir M. M., Cohen M., Tedesco E., The Midcourse Space Experiment Point Source Catalog Version 1.2 Explanatory Guide, 1999, NASA STI/Recon Technical Report N, 14854

Ellingsen S. P., Methanol Masers: Reliable Tracers of the Early Stages of High-Mass Star Formation, 2006, ApJ, 638, 241

Ellingsen S. P., A GLIMPSE-based search for 6.7-GHz methanol masers and the lifetime of their spectral features, 2007, MNRAS, 377, 571

Ellingsen S. P., von Bibra M. L., McCulloch P. M., Norris R. P., Deshpande A. A., Phillips C. J., A survey of the Galactic plane for 6.7-GHz methanol masers - I. l=325 deg-335 deg b=-0.53-0.53, 1996, MNRAS, 280, 378

Elmegreen B. G., Scalo J., Interstellar Turbulence I: Observations and Processes, 2004, ARA&A, 42, 211

Epchtein N. et al., DENIS: A Deep Near-Infrared Survey of the southern sky, 1994, Ap&SS, 217, 3

Gaume R. A., Goss W. M., Dickel H. R., Wilson T. L., Johnston K. J., The NGC 7538 IRS 1 region of star formation: Observations of the H66 alpha recombination line with a spatial resolution of 300 AU, 1995, ApJ, 438, 776

Goddi C., Moscadelli L., Sanna A., Cesaroni R., Minier V., Associations of H_2O and CH_3OH masers at milli-arcsec angular resolution in two high-mass YSOs, 2007, A&A, 461, 1027

Griffin M. J., Ade P. A. R., Orton G. S., Robson E. I., Gear W. K., Nolt I. G., Radostitz J. V., Submillimeter and millimeter observations of Jupiter, 1986, Icarus, 65, 244

Griffin M. J., Orton G. S., The near-millimeter brightness temperature spectra of Uranus and Neptune, 1993, Icarus, 105, 537

Haller E. E., 1993, in Conference on Infrared Physics, Ascona, Switzerland, 21-26 Jun. 1993, p. 21

Haschick A. D., Baan W. A., Menten K. M., Detection of three new methanol maser transitions toward star-forming regions, 1989, ApJ, 346, 330

Hayton D., 2005, Private Communication

Jenness T., Economou F., ORAC-DR – SCUBA Pipeline Data Reduction Starlink User Note 231, 2004, Starlink User Notes

Jenness T., Lightfoot J. F., SURF – SCUBA User Reduction Facility Starlink User Note 216, 2003, Starlink User Notes

Jijina J., Adams F. C., Infall Collapse Solutions in the Inner Limit: Radiation Pressure and Its Effects on Star Formation, 1996, ApJ, 462, 874

Johnson C. O., Depree C. G., Goss W. M., A High-Resolution VLA Study of M17-UC1, 1998, ApJ, 500, 302

Kahn F. D., Cocoons around early-type stars, 1974, A&A, 37, 149

Kessler M. F., Steinz J. A., Anderegg M. E., Clavel J., Drechsel G., Estaria P., Faelker J., Riedinger J. R., Robson A., Taylor B. G., Ximenez de Ferran S., The Infrared Space Observatory (ISO) mission., 1996, A&A, 315, L27

Keto E., The Formation of Massive Stars by Accretion through Trapped Hypercompact H II Regions, 2003, ApJ, 599, 1196

Keto E. R., Welch W. J., Reid M. J., Ho P. T. P., Line broadening in the W3(OH) champagne flow, 1995, ApJ, 444, 765

Krumholz M. R., Klein R. I., McKee C. F., 2005, in IAU Symposium, Vol. 227, Cesaroni R., Felli M., Churchwell E., Walmsley M., ed, Massive Star Birth: A Crossroads of Astrophysics, p. 231

Krumholz M. R., McKee C. F., Klein R. I., Bondi Accretion in the Presence of Vorticity, 2005, ApJ, 618, 757

Lada C. J., 1987, in IAU Symposium, Vol. 115, Peimbert M., Jugaku J., ed, Star Forming Regions, p. 1

Lemke D. et al., ISOPHOT - capabilities and performance., 1996, A&A, 315, L64

Mac Low M.-M., Klessen R. S., Control of star formation by supersonic turbulence, 2004, Reviews of Modern Physics, 76, 125

Matsakis D. N., Wright M. C. H., Townes C. H., Welch W. J., Cheung A. C., Askne J. I. H., An interferometric and multitransitional study of the Orion methanol masers, 1980, ApJ, 236, 481

Matsushita S., Matsuo H., Pardo J. R., Radford S. J. E., FTS Measurements of Submillimeter-Wave Atmospheric Opacity at Pampa la Bola II : Supra-Terahertz Windows and Model Fitting, 1999, PASJ, 51, 603

Maxia C., Testi L., Cesaroni R., Walmsley C. M., The kinematics of molecular clumps surrounding hot cores in G29.96 -0.02 and G31.41+0.31, 2001, A&A, 371, 287

McKee C. F., 1999, in Lada C. J., Kylafis N. D., ed, NATO ASIC Proc. 540: The Origin of Stars and Planetary Systems, p. 29

Menten K., 1991a, in Astronomical Society of the Pacific Conference Series, Vol. 16, Haschick A. D., Ho P. T. P., ed, Atoms, Ions and Molecules: New Results in Spectral Line Astrophysics, p. 119

Menten K. M., The discovery of a new, very strong, and widespread interstellar methanol maser line, 1991b, ApJ, 380, L75

Menten K. M., Walmsley C. M., Henkel C., Wilson T. L., The centimeter transitions of E-type methanol, 1986, A&A, 157, 318

Morimoto M., Kanzawa T., Ohishi M., New maser lines of methanol, 1985, ApJ, 288, L11

Nakano M., Yoshida S., Molecular line observations of the S235B region, 1986, PASJ, 38, 531

Orton G. S., Griffin M. J., Ade P. A. R., Nolt I. G., Radostitz J. V., Submillimeter and millimeter observations of Uranus and Neptune, 1986, Icarus, 67, 289

Pardo J. R., Cernicharo J., Serabyn E., An Improved Model for Millimeter/Submillimeter Applications, 2001, IEEE Trans. Antennas Propagation, 49

Pardo J. R., Serabyn E., Cernicharo J., Submillimeter Atmospheric Transmission Measurements on Mauna Kea during Extremely Dry El Nino Conditions: Implications for Broadband Opacity Contribution, 2001, J. Quant. Spectrosc. Radiat. Transfer, 68

Plambeck R. L., Menten K. M., 95 GHz methanol masers near DR 21 and DR 21(OH), 1990, ApJ, 364, 555

Potter N., 2003, Private Communication

Rice D. P., Ade P. A. R., Absolute Measurements of the Atmospheric Transparency at Short Millimetre Wavelength, 1979, Infrared Physics, 19, 575

Rieke G. H., Visnovsky K., 1996, Detection of Light, From the Ultraviolet to the Submillimeter. Detection of Light, From the Ultraviolet to the Submillimeter, ISBN 0521576741, Illustrated by Karen Swarthourt, Cambridge University Press, 1996.

Salby M. L., 1996, Fundamentals of Atmospheric Physics. Academic Press, San Diego

Sanders D. B., Scoville N. Z., Tilanus R. P. J., Wang Z., Zhou S., 1993, in American Institute of Physics Conference Series, Vol. 278, Holt S. S., Verter F., ed, Back to the Galaxy, p. 311

Schuller F., Ganesh S., Messineo M., Moneti A., Blommaert J. A. D. L., Alard C., Aracil B., Miville-Deschênes M.-A., Omont A., Schultheis M., Simon G., Soive A., Testi L., Explanatory supplement of the ISOGAL-DENIS Point Source Catalogue, 2003, A&A, 403, 955

Schutte A. J., van der Walt D. J., Gaylard M. J., MacLeod G. C., Detection of Thirty-Five New 5/1-6/0A+- Methanol Masers Towards IRAS Sources, 1993, MNRAS, 261, 783

Sewilo M., Churchwell E., Kurtz S., Goss W. M., Hofner P., Broad Radio Recombination Lines from Hypercompact H II Regions, 2004, ApJ, 605, 285

Slysh V. I., Dzura A. M., Val'tts I. E., Gerard E., Further search for OH emission from IRAS sources, 1997, A&AS, 124, 85

Slysh V. I., Kalenski S. V., Val'tts I. E., Detection of a series of methanol maser lines at 1.9 millimeter wavelength, 1995, ApJ, 442, 668

Slysh V. I., Kalenskij S. V., Val'tts I. E., The detection of a new methanol maser transition at 9.9 GHz, 1993, ApJ, 413, L133

Slysh V. I., Kalenskiĭ S. V., Val'Tts I. E., Methanol Radio Emission at Millimeter Wavelengths: New Masers at 1.3 and 2.8 Millimeters, 2002, Astronomy Reports, 46, 49

Sutton E. C., Sobolev A. M., Ellingsen S. P., Cragg D. M., Mehringer D. M., Ostrovskii A. B., Godfrey P. D., New Class II Methanol Masers in W3(OH), 2001, ApJ, 554, 173

Szymczak M., Hrynek G., Kus A. J., A survey of the 6.7 GHz methanol maser emission from IRAS sources. I. Data, 2000, A&AS, 143, 269

Szymczak M., Kus A. J., A survey of the 6.7 GHz methanol maser emission from IRAS sources — II. Statistical analysis, 2000, A&A, 360, 311

Szymczak M., Kus A. J., Hrynek G., Kěpa A., Pazderski E., 6.7 GHz methanol masers at sites of star formation. A blind survey of the Galactic plane between 20 degr = 40 degr and —b— = 0\fdg52, 2002, A&A, 392, 277

Val'tts I. E., Dzura A. M., Kalenskii S. V., Slysh V. I., Booth R. S., Winnberg A., The discovery of methanol masers at 107 GHz, 1995, A&A, 294, 825

Val'tts I. E., Ellingsen S. P., Slysh V. I., Kalenskii S. V., Otrupcek R., Voronkov M. A., Detection of new sources of methanol emission at 107 and 108GHz with the Mopra telescope, 1999, MNRAS, 310, 1077

van der Walt D. J., Gaylard M. J., MacLeod G. C., New detections of 5_1_-6_0_A^+^-methanol masers towards IRAS sources., 1995, A&AS, 110, 81

Voronkov M., Sobolev A., Ellingsen S., Ostrovskii A., Alakoz A., Maser Action in Methanol Transitions, 2005, Ap&SS, 295, 217

Walker R. J., 2003, Ph.D. thesis, Cardiff School of Physics and Astronomy

Walsh A. J., Hyland A. R., Robinson G., Burton M. G., Studies of ultracompact HII regions - I. Methanol maser survey of IRAS-selected sources, 1997, MNRAS, 291, 261

Wang J.-Q., Richards P. L., Beeman J. W., Haegel N. M., Haller E. E., Optical efficiency of far-infrared photoconductors, 1986, Appl. Opt., 25, 4127

Wang J.-Q., Richards P. L., Beeman J. W., Haller E. E., Stressed photoconductive detector for far-infrared space applications, 1987, Appl. Opt., 26, 4767

Ward-Thompson D. et al., First ground-based 200-μm observing with THUMPER on JCMT - sky characterization and planet maps, 2005, MNRAS, 364, 843

Whiteoak J. B., Gardner F. F., Caswell J. L., Norris R. P., Wellington K. J., Peng R.-S., Methanol absorption at 12.2 GHz towards SGR B2, 1988, MNRAS, 235, 655

Whiteoak J. B., Peng R.-S., Observations of 12.2-GHz methanol absorption towards the molecular cloud G1.6-0.025, 1989, MNRAS, 239, 677

Williams J. P., Blitz L., McKee C. F., The Structure and Evolution of Molecular Clouds: from Clumps to Cores to the IMF, 2000, Protostars and Planets IV, 97

Wilson T. L., Huettemeister S., Dahmen G., Henkel C., Three transitions of methanol at 1 CM wavelength, 1993, A&A, 268, 249

Wilson T. L., Walmsley C. M., Jewell P. R., Snyder L. E., Detection of a new type of methanol maser, 1984, A&A, 134, L7

Wilson T. L., Walmsley C. M., Menten K. M., Hermsen W., The discovery of a new masering transition of interstellar methanol, 1985, A&A, 147, L19

Wilson T. L., Zeng Q., Huettemeister S., Dahmen G., The J_2_-J_1_ E methanol transitions for J=12 in Orion KL., 1996, A&A, 307, 209

Wolfire M. G., Cassinelli J. P., Conditions for the formation of massive stars, 1987, ApJ, 319, 850

Wood D. O. S., Churchwell E., Massive stars embedded in molecular clouds - Their population and distribution in the galaxy, 1989, ApJ, 340, 265

Yorke H. W., Sonnhalter C., On the Formation of Massive Stars, 2002, ApJ, 569, 846

Zammit C. C., Ade P. A. R., Zenith atmospheric attenuation measurements at millimetre and sub-millimetre wavelengths, 1981, Nature, 293, 550